**TECHNISCHE
UNIVERSITÄT
WIEN**
Vienna University of Technology

DISSERTATION

Atmospheric tides
in Earth rotation observed with VLBI

ausgeführt zum Zwecke der Erlangung des akademischen Grades einer Doktorin der technischen Wissenschaften unter der Leitung von

Univ. Prof. Dipl.-Ing. Dr.techn. Johannes Böhm
E120-4
Department für Geodäsie und Geoinformation
Höhere Geodäsie

eingereicht an der Technischen Universität Wien
Fakultät für Mathematik und Geoinformation

von

Anastasiia Girdiuk
Matr.-Nr.: 1476053

Wien, November 2017

Acknowledgements

I would like to thank my friends for having a great time together and all who supported and cared about me. It helped me indeed to follow this road. But surely beyond all doubts, I wholeheartedly thank my parents, my mother and grandmother, for caring and educating me in this way, which I deeply appreciate.

Abstract

The Earth's body is enveloped with fluids represented mostly by the atmosphere and oceans, which force the Earth's rotation vector to alter. On daily and sub-daily time scales, differential gravitational forces of the Moon and Sun govern the regular Earth rotation variations by raising ocean tides. A distinct addition and modulation of these ocean tide effects is provided by atmospheric tides, which result from cyclic absorption of insolation at upper air and boundary layer heating at the Earth's surface. Short period tidal mass variations that are of particular relevance to Earth rotation are those with Sun-locked diurnal S_1 (24 hour) and semidiurnal S_2 (12 hour) periodicities.

Atmospheric tides were discovered first in the variations of the surface pressure field, whose measurements are ingested into weather models along with a presentation of the S_1 and S_2 cycles from remote sensing. The impact of these variations on Earth rotation can be determined from a geophysical modeling perspective by means of an angular momentum approach. In this thesis, the Earth's rotation effects related to atmospheric tides are evaluated in a separate approach based on the Very Long Baseline Interferometry (VLBI) observations. Elucidating the potential reasons for the well-known discrepancies in Earth rotation between these two approaches formulates the core argumentation in this thesis.

Overall, atmospheric tide effects in Earth rotation are detected on the expected level in the analysis of the VLBI observations. The reliability of these signals is confirmed directly through a comparison with geophysical estimates and indirectly validating the obtained high-frequency ocean tide terms against the range of reference solutions. For polar motion, previous studies have documented a significant discrepancy between the geodetic and geophysically derived S_1 terms at the order of 10 µas or large. This difference is mitigated to 5 µas in the present study, yet this value is above the best threefold formal error level in polar motion (2.5 µas) provided by the undertaken VLBI analysis.

In a supplementary study Earth rotation tide models were considered in dependence on the applied corrections to the station VLBI positions due to the loading effects of the fluids as provided by different geophysical models and vice versa. However in both approaches, the parameter estimates based on different geophysical models demonstrate statistically insignificant variations under threefold formal error level.

Contents

Chapter 1

Introduction

A research in the area of the Earth system is interested in a wide range of processes from the deep interior of the Earth to the outermost layer of the atmosphere. A unified set of observations of the entire Earth's behavior is now available and promotes further investigations to explore this comprehensive interactive system. In geodesy, the most researches are focused on supporting an accurately determined global reference frame (Plag *et al.*, 2009) on which to base parameters for the Earth rotation, gravity field and geokinematics considerations. This work ultimately involves collaboration with climate monitoring, and efforts to analyze and forecast processes in the atmosphere and oceans. Vice versa, studies of the Earth's structure of atmosphere layers and oceans, benefit from a stable reference frame realization. Specifically, each layer of the Earth system is presumed to experience loading, with both periodical and irregular variations. An examination of these signals and other interactions among Earth's layers is integral to the geodetic and geodesy-related analysis. Nowadays the fundamentals of the Earth System are well known even down to extraordinarily small scales. Nevertheless, the exploration of the influence of the second, third and higher order terms refines the system of knowledge to underpin the reliability of previous investigations (Gross, 2015) with updated arguments. In addition, a cross-validation of results obtained independently by different approaches provides a step toward understanding changes in the system.

1.1   Summary

The entire Earth system and dynamics are affected by external forcing of the Sun and Moon. The result which appears chiefly in the oceans is the well-known effect of tidal variations. The study of ocean tides is a classic example of a dynamic theory, in which the fundamentals have been investigated since the XVIII century by Newton (laying the foundations for classical mechanics) and Euler (calculating the eigenperiods of rigid body rotation). Later, Chandler discovered a considerable departure from Euler's eigenperiod with a period of 433 days mainly sustained by both atmosphere and oceanic excitations (Gross, 2015).

In this thesis the focus is on the study of the periodic variations of the atmosphere which

can be seen in the high-frequency Earth's rotation. These effects are forced by regular solar heating (Chapman & Lindzen, 1970) and commonly known as the diurnal S_1 and semidiurnal S_2 atmospheric tides. Direct insolation is absorbed in upper layers (Hagan *et al.*, 2003), leading to vertically propagating waves that are also recognized in the atmospheric surface pressure field. These atmospheric or "radiational" tides in the pressure field are effective in inducing motions in the oceans, namely the hydrodynamic response to the atmospheric forcing (Ray & Egbert, 2004) at the same frequencies (S_1, S_2). The combination of these effects are referred to as atmospheric tides; the less powerful excitation sources as, e.g., gravitational forcing of the atmospheric mass can be omitted (Ray & Egbert, 2004).

Analysis of one part of the Earth system cannot be performed in a completely independent approach. In the study of the atmospheric tides, the other components are required to be accounted for, in particular, the ocean tides occurring at the same frequencies as the atmospheric tides. One of the main ocean tides is the S_2 tide, known as the principal solar semidiurnal tide, and the one of the smallest ocean tides is the combined S_1 tide (Simon *et al.*, 2013). The study of the atmospheric S_2 tide is, thus, corrupted by the significant ocean forcing, while the atmospheric S_1 tide amplitude dominates the small ocean S_1 tide; therefore, this thesis mainly deals with the assessment of the atmospheric S_1 tide.

1.2 Motivation for research

This thesis's objective is to determine the atmospheric tides in the variations of the Earth's rotation by means of the geodetic Very Long Baseline Interferometry (VLBI) observations. While this evaluation remains challenging for geodetic methods, the same effects can be determined using geophysical modeling (Schindelegger, 2014) on the confident level. For instance, the atmospheric tides were computed recently (Schindelegger, 2014; Schindelegger *et al.*, 2016, 2017) based on the angular momentum approach for both, atmosphere and oceans. These geophysical model results are under the formal error level provided by the analysis in geodesy (Girdiuk *et al.*, 2016b), giving a rise to a discrepancy of approximately 10 μ*as* at the S_1 frequency in the high-frequency band of polar motion. Moreover, in this band of the Earth's rotation the S_1 tide represents one of the smallest signal amplitudes. In the present thesis, the origins of this discrepancy are explored based on geodetic VLBI analysis.

The topic of this thesis was designed under project ASPIRE (anagram-abbreviation for Atmosphere-Induced Short Period variations of Earth Rotation), whose aim was to reconcile geophysical excitations with geodetic estimates for the atmospheric tides. Geophysical values were obtained by Michael Schindelegger based on a combination of meteorological data analysis and ocean modeling (Schindelegger *et al.*, 2017). To validate these estimates in the second part of the project, the geodetic account for the atmospheric tides is set up in this thesis. To that end, an accurate solution for ocean tide effects is required to be deduced consistently using the same input data as for the atmospheric tides detection. This ocean model should corroborate the pre-

vious VLBI solutions (Artz *et al.*, 2011; Böhm *et al.*, 2012, b) or the combined solution with the Global Positioning System (GPS) observations (Artz *et al.*, 2012). The amplitudes at the frequencies of the atmospheric tides are not adequate in these previous solutions, and thus, the current assessment is aimed on the contribution to an agreement with geophysical approach.

Besides variations in the Earth's rotation, the atmospheric tides are recognized in the atmospheric loading signals, that is, harmonic station positions variations. The interdependence between loading and high-frequency Earth's rotation is a supplementary study in this thesis. The usage of the tidal loading models was shown to produce the positive effect (Wijaya *et al.*, 2013) for the geodetic parameter (baseline length repeatability) related to the station positions. The application of a particular model, however, seems to lead to an insignificant changes in terms of the baseline length repeatability as well as the S_1 estimates in the Earth's rotation (Girdiuk *et al.*, 2016a). In addition to considering pre-calculated values from the atmospheric loading models, the same effects are directly estimated in the VLBI observations. The obtained results as well as the high-frequency tide terms are used to assess the current capabilities of the VLBI analysis.

1.3 Thesis outline

The classical approach to describe the Earth's rotation is represented briefly in the Chapter 2. Since the high-frequency Earth's rotation model related to the external lunar-solar attraction is not a part of this approach, the corresponding variations are discussed separately.

In Chapter 3 the basic principles of the VLBI method are explained and its advantages are underlined. The set of reductions is divided into three main groups and follows recommendations by the International Earth Rotation and Reference Systems Service (IERS) Conventions with a few extensions to this guidance related to the geophysical model implementation.

The foundation of the VLBI analysis is the data set. The assembled data set is described in Chapter 4 along with the analysis commonly applied in the processing of the VLBI observations. Further, the single session solution, which is employed mostly in this thesis, and the global solution are described. The time series evaluations of the high-frequency Earth Rotation Parameters (ERP) and station positions in the single session solution are reviewed to reduce most of deficiencies in the time series for the detection of the atmospheric tides.

Chapter 5 collects the main results in this thesis. The empirical high-frequency tide terms model is obtained by means of three methods of the time series approach. These results are validated using the major ocean tides against geodetic solutions and geophysical models. As regards the S_1 tide, the discrepancy with geophysical model estimates is confirmed, but overall the difference is reduced to agree more favorably with the most recent geophysical assessment by (Schindelegger *et al.*, 2017).

The supplementary study of the station position variations estimated internally in the VLBI analysis reveals realistic amplitudes in comparison with values derived from geophysical models. Here, for the first time, no any constraints or additional assumptions are used to retrieve these

daily and sub-daily signals. However, these achievements encounter the certain restrictions by the formal error level.

Chapter 6 concludes this thesis with a brief summary on results and the present formal error level in the VLBI analysis.

Chapter 2

Geophysical interactions

This chapter reviews accepted formalisms to describe Earth's rotation motion and its perturbation factors (Moritz & Müller, 1987; Gross, 2015) as well as a framework of geodetic application recommended by the IERS Conventions (Petit & Luzum, 2010).

Geophysical interactions occurring among the layers of the atmosphere, oceans and the Earth enveloped by these fluids are an important factor influencing the Earth's rotation variations. The set of parameters – polar motion, Length of Day (LOD), precession and nutation – is known as Earth Orientation Parameters (EOP). These quantities represent an interest in Earth's rotation research. On the one hand, their determination has been the subject for a variety of investigations devoted to modeling of geophysical influences (Egbert & Erofeeva, 2002; Ponte *et al.*, 2002; Schindelegger *et al.*, 2017). On the other hand, the EOP variations can be observed at high accuracy using modern space-geodetic techniques. In this thesis in particular, an empirical determination of the EOP is performed based on the analysis of VLBI observations.

At the very highest frequencies, in the sub-daily band, the Earth's rotation is significantly perturbated by the dynamic ocean tides. A secondary influence at these time scales is due to the daily solar irradiance referred to as the atmospheric tide. The ocean tides have larger amplitudes at the diurnal and semidiurnal bands, but owing to non-linear heating processes the atmosphere contribution prevails over the oceanic one at the particular frequency of the S_1 tide.

This thesis focuses on the small diurnal and semidiurnal atmosphere-induced variations, yet the oceanic contribution is considered to treat the Earth's rotation simultaneously. In this chapter, the general dynamic concept of the rotating Earth and its excitations are presented, first. Secondly, the gravitational tidal potential, which provides external torques on the system Earth and induces ocean tides, is derived. Finally, this gravitational potential theory is utilized to introduce the atmospheric tides by means of a radiational potential (Munk & Cartwright, 1966) and the thermodynamic background of the atmospheric tides is summarized briefly.

2.1 Earth Rotation

The movement of the Earth in a field of an external gravitational attraction $\mathscr{L}$ can be described without loss of generality by the fundamental dynamic equation of a rotating solid body:

$$\mathscr{L} = \frac{d}{dt}\vec{H} + \vec{\omega} \times \vec{H}, \tag{2.1}$$

where the applied reference frame (and thus, the time derivative $\frac{d}{dt}$) is fixed to the Earth-body. This equation is called Liouville's equation in geophysics (Moritz & Müller, 1987; Gross, 2015). In the classical approach (Moritz & Müller, 1987) the geophysical excitation modeling of Earth's rotation disregards the lunisolar gravitational field ($\mathscr{L} = 0$) which produces torques $\mathscr{L}$. In this case, the total angular momentum of the Earth $\vec{H}$ remains constant. The angular momentum consists of a solid part and that of fluids (the most essential for this study: ocean and atmosphere). According to the IERS Conventions (Petit & Luzum, 2010) an additional assumption is introduced to specify the solid Earth as consisting of the crust, mantle and core. As follows, any changes in angular momentum of the fluids compel to make an alteration to the angular momentum of the solid Earth. The exchange processes in the angular momentum of the fluids and solid Earth lead to variations of the Earth rotation. The total vector of the entire system $\vec{H}$ therefore is tackled into two parts: relative angular momentum $\vec{h}$ is an indicator of the motion relative to the rotating reference frame and variable inertia tensor $\vec{I}$ is a marker of the mass re-distribution. This principle can be expressed

$$\vec{H} = \underbrace{\vec{I}\vec{\omega}}_{\text{mass or matter term}} + \underbrace{\vec{h}}_{\text{motion term}} = \text{constant}, \tag{2.2}$$

where an angular velocity vector $\vec{\omega}$ quantifies a rotation of body-fixed reference frame attached to the Earth body with respect to the inertial (space-fixed) reference frame. This velocity, thus is instantaneous angular velocity of the Earth, a measure of its rotation, which includes a constant part Ω mainly along $\boldsymbol{z}$ axis with small departures from uniform rotation $m_x, m_y, m_z \ll 1$:

$$\vec{\omega} = \Omega(m_x, m_y, 1 + m_z). \tag{2.3}$$

Similar to the Earth's rotation velocity $\vec{\omega}$ the inertia tensor $\vec{I}$ is time-variable. The inertia of the Earth defines the internal mass distribution which is divided into the constant part assigned

by the diagonal elements and the variable additions to each element:

$$\vec{I} = \begin{pmatrix} A & 0 & 0 \\ 0 & B & 0 \\ 0 & 0 & C \end{pmatrix} + \begin{pmatrix} \Delta I_{xx} & \Delta I_{xy} & \Delta I_{xz} \\ \Delta I_{xy} & \Delta I_{yy} & \Delta I_{yz} \\ \Delta I_{xz} & \Delta I_{yz} & \Delta I_{zz} \end{pmatrix}, \tag{2.4}$$

where A, B and C are the principal moments of inertia of the Earth and meet the conditions $C > B > A$. Most of rotation power is carried out by the constant part, so that the Earth motion can be described by the formalism of the rigid solid body to the first order. The variable part, thus, causes very small but measurable variations which can be utilized to investigate the internal structure and processes occurring in the Earth's body (Yoder *et al.*, 1981).

The product of inertia and angular velocity of the Earth represents mass or matter term and the other component in equation (2.2) presents relative angular momentum and called the motion term (Schindelegger *et al.*, 2013; Gross, 2015). In accordance with generally accepted principles (Gross, 2015; Petit & Luzum, 2010), the relative angular momentum is permitted only for core, ocean, atmosphere and other fluid's motions in the Tisserand mean-mantle frame and canceled for the crust and mantle motions.

The ultimate solution of equation (2.1) upon linearization within the angular momentum approach is

$$\begin{aligned} \frac{1}{\hat{\sigma}_0}\dot{\hat{m}} + \hat{m} &= \hat{\chi} - \frac{i}{\Omega}\dot{\hat{\chi}}, \\ m_z &= -\chi_z, \end{aligned} \tag{2.5}$$

where $\hat{\sigma}_0$ is the observed complex frequency of the Chandler wobble. The vector of motion $\hat{m}$ in equation (2.5) is the combination of two orthogonal components $\hat{m} = m_x + im_y$ which depict the position of the rotation axis of the body-fixed reference frame. The effective angular momentum functions $\hat{\chi}$ and χ_z convey geophysical excitations and are defined by the mass distribution and motions terms:

$$\begin{aligned} \hat{\chi} = \chi_x + i\chi_y = \chi_p + \chi_w &= \frac{1.100\Omega\Delta\hat{I} + 1.608\hat{h}}{(C - A')\Omega}, \quad \Delta\hat{I} = \Delta I_{xz} + i\Delta I_{yz}, \\ &\qquad\qquad\qquad\qquad\quad \hat{h} = h_x + ih_y, \\ \chi_z = \quad = \chi_p^z + \chi_w^z &= \frac{0.748 I_{zz}\Omega + 0.997 h_z}{\Omega C_m}, \end{aligned} \tag{2.6}$$

where the constant A' characterizes the average equatorial moment of the Earth's inertia tensor and satisfies condition $C >> A' = (A + B)/2$. Derivations as well as numerical quantities of the utilized parameters, for instance, the Chandler wobble frequency, the principal moments of

inertia and scaling coefficients in equation (2.6) can be found in work by Gross (2015). Equation (2.6) is valid for a realistic Earth model which represents an elastic body composed of fluid core, equilibrium oceans, anelastic mantle and atmosphere (Gross, 2015). For the atmosphere, the mass and motion terms are related to excitations from pressure ($\boldsymbol{\chi_p}$) and wind ($\boldsymbol{\chi_w}$) which can be calculated based on the pressure field variations and wind pattern provided by various numerical weather models and forecasts. The background equations to calculate effective angular momentum functions are generalized in Appendix A. To adopt this approach for the ocean, pressure and winds can be substituted by heights and currents to evaluate ocean tidal angular momentum functions on the stipulation that a homogeneous flow is defined per column for the still water, where a mass unit is replaced by the mean density of the sea water.

An explicit dependence of the Earth's axial angular velocity upon the axial excitation function is illustrated in equations (2.5) and (2.6). The observed variations of LOD or changes in Universal Time (dUT1), thus, can be obtained by the utilization of the effective excitation functions proposed by Barnes *et al.* (1983)

$$\chi_z = \frac{\text{LOD}(s)}{86400s} + \text{constant} = -\frac{d}{dt}\text{dUT1} + \text{constant}, \qquad (2.7)$$

so that LOD characterizes departures from the standardized length 86400 s of the instantaneous Earth's rotation m_z.

2.1.1   Conventional parametrization

While the interpretation of the m_z component of Earth rotation is rather straightforward, treatment of the complex motion $\hat{m}$ is a more complicated task that demands introducing additional definitions. The location of the instantaneous rotational axis $\hat{m}$ on the Earth surface is called a rotation pole. In perpendicular plane to the Earth's axis the North pole is the origin of rectangular coordinate system, where axes are directed to the Greenwich meridian (x) and 90° West (y). However, observing systems are incapable to determine directly the motion of the instantaneous rotating pole. As a consequence, the definition of the Celestial Intermediate Pole (CIP) is introduced (McCarthy & Capitaine, 2002) by means of measured values of x and y components of the CIP motion in a Terrestrial Reference Frame (TRF). Consisting with astrometry's traditions, this approach separates the Earth's axis motion in the perpendicular plane (xy plane) into precession-nutation and polar motion, so that the long-term variations observed in a celestial reference frame correspond to precession and nutation and almost all variations in the terrestrial reference frame belong to polar motion (except diurnal band with frequencies between -1.5 and -0.5 Cycle per sidereal day (cpsd) specified in TRF).

From a mathematical point of view, three rotations with corresponding angles are necessary and sufficient to define a transformation matrix from one reference system to another. This is, an observer's position given in the terrestrial reference frame $\vec{r}_t$ can be converted to the celestial

reference frame $\vec{r}_c$ by means of three angles defined by direction cosines in equation (2.3). For practical applications, the last resolutions of the International Astronomical Union (IAU) (Mc-Carthy & Capitaine, 2002) introduce the transformation formalism between the International Terrestrial Reference System (ITRS) and the Geocentric Celestial Reference Frame (GCRS):

$$\vec{r}_c = QRW\vec{r}_t, \tag{2.8}$$

$$Q = R_3(-E)\cdot R_2(-d)\cdot R_3(E)\cdot R_3(s), \tag{2.9}$$

$$R = R_3(-ERA). \tag{2.10}$$

$$W = R_3(-s')\cdot R_2(x)\cdot R_1(y), \tag{2.11}$$

where the classical transformations W stands for the transformation of the observer's location from the TRF to an intermediate system using the reported pole coordinates of the CIP x and y. With respect to the kinematical definition of "non-rotating" origins, in the terrestrial reference system the "Terrestrial Intermediate Origin (TIO) locator s'" specifies the TIO position on the equator of the CIP and the "Celestial Intermediate Origin (CIO) locator s" provides the CIO position on the equator of the CIP correspondingly. The next transformation matrix R rotates the obtained CIP position to account for the spin motion around the CIP axis on the angle ERA (Earth Rotation Angle) between intermediate celestial and terrestrial reference systems (CIO and TIO). The last matrix Q sets the previous resultant to the celestial reference frame by rotating for precession-nutation motion. The motion of the CIP in the GCRS is described by angles E and d in equation (2.9) used to define the rectangular coordinates of the CIP in the GCRS:

$$\begin{cases} X &= \sin d\cos E, \\ Y &= \sin d\sin E, \\ Z &= \cos d. \end{cases} \tag{2.12}$$

and by a rotation from the intermediate reference frame on angle s expressed as a function of X, Y (Capitaine *et al.*, 2003). The model for precession and nutation utilized in the last IERS Conventions (Petit & Luzum, 2010) takes into account these effects as provided by Capitaine *et al.* (2003), including frame biases. In this theory, however, the Free core nutation (FCN) is not included and by this reason so-called celestial pole offsets (dX, dY) are required to be estimated from observations. Hence, the matrix Q implemented in all reductions uses a model matrix Q_{IAU}:

$$Q = Q_{\text{IAU}} \begin{pmatrix} 1 & 0 & dX \\ 0 & 1 & dY \\ -dX & -dY & 1 \end{pmatrix}. \tag{2.13}$$

The transformation matrix given in equation (2.8) implies rotation on five angles, because both locators s' and s are defined by the polar motion or precession-nutation quantities correspondingly. Thus, five EOP are used to associate any transformation from celestial to terrestrial reference frame and vice versa. These EOP are two components of polar motion, the parameter describing spin, LOD or dUT1, and two parameters to depict precession and nutation. Since a minimal number of transformations between two systems in three-dimensional space is defined by three rotations, the set of the EOP involves a linear combination between polar motion $\boldsymbol{p}$ and precession-nutation motion $\boldsymbol{n}$

$$\hat{\boldsymbol{p}} = -\boldsymbol{n}e^{-i\Omega t},$$
$$\boldsymbol{n} = X + iY. \tag{2.14}$$

The parametrization for combined complex polar motion of the CIP can be expressed by $\hat{\boldsymbol{p}} = x - iy$, so that the analytical solution in form of the rotation Ω between the body-fixed terrestrial and the intermediate reference frames (CIP) (Gross, 1992) reads:

$$\hat{\boldsymbol{m}} = \hat{\boldsymbol{p}} - \frac{i}{\Omega}\frac{d}{dt}\hat{\boldsymbol{p}}. \tag{2.15}$$

This provides the link between reported vector $\hat{\boldsymbol{p}}$ in the terrestrial reference and theoretical quantities $\hat{\boldsymbol{m}}$. For frequencies, the following relation (Gross, 1992) holds

$$\sigma_{\text{celestial}} = \sigma_{\text{terrestrial}} + \Omega. \tag{2.16}$$

Long-term precession-nutation motions in the celestial reference frame can be found in equation (2.16) to correspond to the high-frequency variations in the terrestrial reference frame with frequencies $\sigma_{\text{terrestrial}} \approx -\Omega$. As common, any motion along with the direction of Earth rotation is referred to as the prograde motion and labeled by positive frequencies. At the negative frequencies semidiurnal retrograde polar motion propagates backwards with respect to the direction of Earth rotation. Nearly diurnal polar motion exhibits the effect of ocean tides in the diurnal and semidiurnal bands. These effects were neglected in the previous realization of the intermediate reference frame known as Celestial Ephemeris Pole. Currently, geodetic observing systems are approaching to a millimeter level, on which the account for ocean tides is required. By this reason, the modern conventional CIP also takes into account effects of ocean tides. In the CIP framework precession-nutation comprises any motions of the CIP observed in the celestial reference frame in range of frequencies between -0.5 and 0.5 cpsd. All remaining frequencies in celestial reference are ascribed to polar motion. In the terrestrial reference frame, nutation encompasses frequencies between -1.5 and -0.5 cpsd and all other frequencies in the domain are in polar mo-
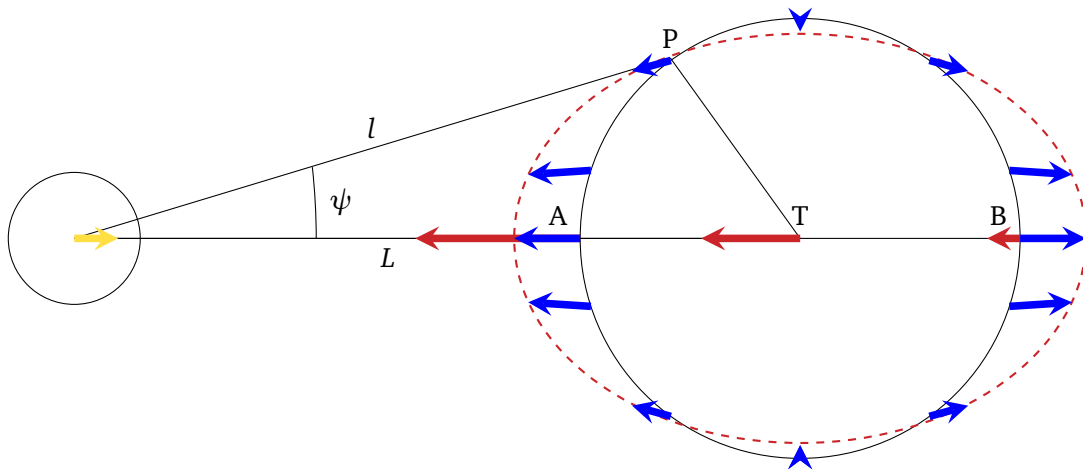
Figure 2.1: A schematic plot of mutual position of the Moon (on the left side) and the Earth (on the right) is shown where the bodies centers are located on the same line and separated by the distance L. T is the Earth's center, A and B are the diametrically opposite points on the Earth's surface and the line connected to the Moon's center. At these points red vectors denote accelerations towards to the Moon, in inverse direction there is the compensated acceleration to the Earth marked by yellow color. Differential accelerations appear at every point at the Earth body (blue vectors) and supply the theoretical circle (at the first approach) Earth figure with tidal bulges illustrated by the red dashed line. An arbitrary point P on the Earth's surface is remote on the distance l from the Moon's center.

tion. Thus, tides in the terrestrial reference frame appear at prograde diurnal frequencies and the entire semidiurnal band of polar motion. The retrograde diurnal band is cleansed from any polar motion signals, which are nutations and studied in the celestial reference frame.

2.2   Tidal potential and ocean tides

The periodic effect of rising and descent of water level and its source, the gravitational attraction by the Moon, were known for many centuries. But the fact of existing tides twice per day was discovered by Newton (Feynman *et al.*, 1963) who gave the correct interpretation. To illustrate the tide generation mechanism, the two bodies case suffices as a first approach. According to Newton's law of universal gravitation the Earth experiences the attraction decreasing with distance from the Moon as the inverse squared law. The Earth is supposed to be different from the point mass body, namely an extended body is considered. In the result of the Earth's extent the differential accelerations appear in diametrically opposite points A and B on the Earth surface. At these points the following relationship between accelerations $\vec{a}_A$ and $\vec{a}_B$ holds:

$$\vec{a}_B < \vec{a}_T < \vec{a}_A, \tag{2.17}$$

where $\vec{a}_T$ is applied to the Earth's center. In Figure 2.1 the red vectors denote accelerations induced in the points A, B and T towards to the Moon placed on the line which ties the body's centers. The Earth's surface attracted maximally on the point A depicts a "tide is under the Moon"
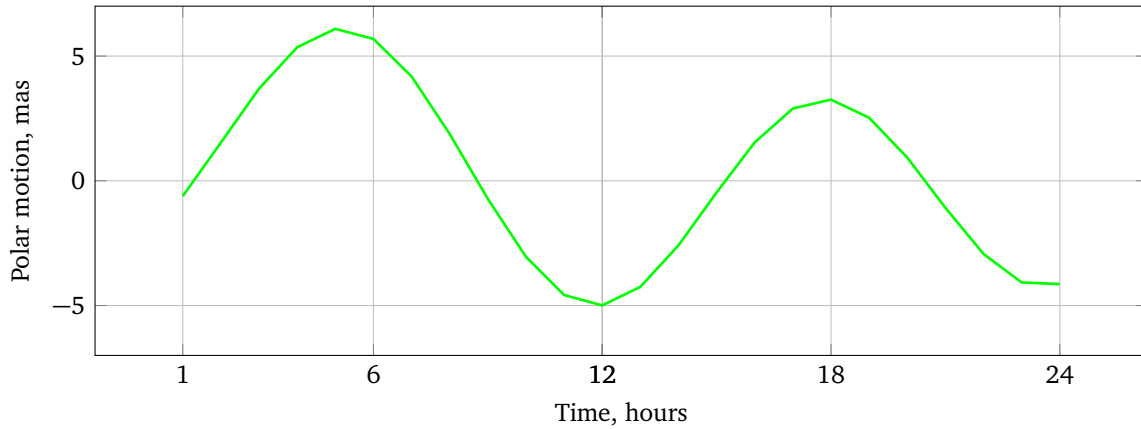
Figure 2.2: A signature of a tidal wave in polar motion over 24 hours.

(see Figure 2.1) while the gravitational field on the point B has minimal effect on the Earth's surface. When these accelerations are considered with respect to the center of the Earth, point B experiences the differential acceleration similar to point A:

$$
\begin{aligned}
\vec{w}_A - \vec{w}_T &= GM\Big(\frac{1}{(L - R_\oplus)^2} - \frac{1}{L^2}\Big) \approx GM\frac{2R_\oplus}{L^3}\frac{\vec{L}}{L}, \\
\vec{w}_B - \vec{w}_T &= GM\Big(\frac{1}{(L + R_\oplus)^2} - \frac{1}{L^2}\Big) \approx GM\frac{2R_\oplus}{L^3}\frac{\vec{L}}{L},
\end{aligned}
\tag{2.18}
$$

where the vector $\vec{L}$ is the distance between centers of the Earth and Moon, $R_\oplus$ is a radius of the Earth.

The first order terms in equation (2.18) reveal the same accelerations of A and B where collinear vectors pointed in opposite directions shown in Figure 2.1 in blue. An arbitrary point on the Earth's surface between marginal locations in point A and B experiences acceleration pointed towards to A or B. The directions of resulting vectors depend on the hemisphere with respect to the rotational axis in which this arbitrary point is located. At the poles, the Earth's surface is affected by acceleration half as small as differential acceleration on the straight line between body's centers: $GM\frac{R_\oplus}{L^3}\frac{\vec{L}}{L}$. The surface, which is subject to these differential or, also called, tidal accelerations, is shown by red dashed line in Figure 2.1 and defines the equilibrium. The equilibrium surface demonstrates the balance of the tidal forces with hydrostatic pressure. Moreover, tidal amplitudes and phases are calculated relative to this surface.

As the result of Earth's rotation, the gravitational attraction of the Moon is compensated by inertia forces. The corresponding tidal accelerations can be demonstrated by the action of the fluid Earth's bulge. The bulge appears twice per day in every location on the surface due to Earth's rotation and moves across the planet with period of the Moon's revolutions. The amplitude of the one bulge part can be seen large than the other. This fact can be confirmed by extracting higher order terms in the equation (2.18), so that in any area during a day one of the tidal heights

rises above the other. This effect is illustrated in Figure 2.2 in terms of polar motion wobble. Two increases of the amplitude wave during a day display the presence of the supplemental two bulges on the opposite sides of the Earth. And an increment of one of them characterizes diurnal variations as a smaller addition to the semidiurnal effects.

2.2.1   Analytical expansion of tidal potential

The motion in the Earth-Moon system occurs around the common center of the mass, which is located within the Earth's body. This position of the center of mass indicates the considerably smaller Moon's mass and potential V than the Earth gravitational field. The major influence of the Moon's potential V is the differential accelerations produced by the tidal force at the arbitrary point on Earth's surface P, removed from the Moon's center at distance l shown in Figure 2.1. In accordance with Newton's law, the gravitational field of the force $\vec{F}$ is described by a scalar function (Moritz & Müller, 1987) of the spherically symmetric potential field V generated by mass M

$$\vec{F} = -\nabla V \Longleftrightarrow V = \frac{GM}{l}, \tag{2.19}$$

where G is the gravitational constant. The distance $1/l$ can be expressed by Legendre polynomials P_n of degree n (see Appendix A for details) in the theoretically infinite sum:

$$\frac{1}{l} = \frac{1}{\sqrt{R_\oplus^2 + L^2 - 2\,R_\oplus\,L\,\cos\psi}} = \frac{1}{L}\sum_{n=0}^{\infty}\left(\frac{R_\oplus}{L}\right)^n P_n(\cos\psi), \tag{2.20}$$

where ψ is the central angle between the arbitrary point P at the Earth surface on the radius $R_\oplus$ and the Moon.

The nabla operator ∇ defined as $\left(\frac{\partial}{\partial x}, \frac{\partial}{\partial y}, \frac{\partial}{\partial z}\right)$ in the Cartesian coordinate system (x, y, z) of the distance vector $\vec{L} = (L_x, L_y, L_y)$ is applied to determine accelerations:

$$-\nabla V \;\; = \;\; + \begin{cases} \nabla\dfrac{GM}{L^2}\dfrac{\vec{L}}{L} == \vec{w}_T \\[2mm] \nabla\dfrac{2GM}{L^3}\dfrac{\vec{R}_\oplus\vec{L}}{L} == \vec{w}_P{}^{\text{rel}} \\[2mm] \nabla\dfrac{GM}{L}\displaystyle\sum_{n=2}^{\infty}\left(\dfrac{R_\oplus}{L}\right)^n P_n(\cos\psi) \end{cases} \tag{2.21}$$

The first term represents the acceleration force exerted by the Moon, for the particular simple case in which the potential field is induced by a point mass on the distance L. This gravitational attraction forced by the Moon at the center of the Earth balances the centrifugal force applied to

the Moon to keep revolving around the Earth. The second term comprises the nearly equal terms obtained in equations (2.18) coerced by tide generating forces. These forces shape the Earth with approximatively the same two tidal bulges. Thus, the first two terms are compensated.

The next terms, harmonics $n = 2$ and higher in equation (2.21), caused by differential acceleration are referred to as 'tidal potential' or Tide Generating Potential (TGP) (Dehant & Mathews, 2015)

$$V_{\text{TGP}} = \frac{GM}{L} \sum_{n=2}^{\infty} \left(\frac{R_\oplus}{L}\right)^n P_n(\cos \psi), \tag{2.22}$$

The only term of the TGP which is worth to be considered further is V_2, because it comprises 98% of the V_{TGP} (Torge & Müller, 2012). The central angle ψ can be defined (Moritz & Müller, 1987) also as the zenith distance of the Moon in the equatorial coordinate system. The spherical triangle encompasses positions of the North Pole, direction on Zenith in the location of the observer (ϕ, λ') and the Moon (δ, λ), so that the angle ψ can be expressed by the cosine rule into the longitude difference $(\lambda - \lambda')$

$$\cos \psi = \sin \phi \sin \delta + \cos \phi \cos \delta \cos(\lambda - \lambda'). \tag{2.23}$$

These mutual position angles are used in the substitution of the second degree TGP V_2 in equation (2.22), so that the final result contains the sum of following terms (Sidorenkov, 2009; Torge & Müller, 2012)

$$\begin{aligned} V_2 \;=\; & D\left(\tfrac{L_0}{L}\right)^3 && \Big(3(\sin^2 \phi - \tfrac{1}{3}) && (\sin^2 \delta - \tfrac{1}{3}) && + \\ && & + \sin 2\phi && \sin 2\delta && \cos(\lambda - \lambda') + \\ && & + \cos^2 \phi && \cos^2 \delta && \cos(2(\lambda - \lambda'))\Big), \end{aligned} \tag{2.24}$$

where the Doodson constant $D = \frac{3GM}{4} \frac{R_\oplus^2}{L_0^3}$ comprises time-independent coefficients $G, M, R_\oplus$ and L_0 (lunar major semi-axis of revolution). Terms in equation (2.24) reveal periodic solution of tidal potential and distribution of these solutions on the sphere. The distribution serves to describe the Earth's surface differential perturbations by lunar attraction. Corresponding terms in equation (2.24) include the latitude-dependent $(\sin^2 \phi - \tfrac{1}{3})$ factor which divides the sphere into loci where the potential surface takes positive values in the range $-35° \leqslant \phi \leqslant 35°$ and negative everywhere else. The solutions, which meet this condition, belong to zonal spherical functions (zonal harmonics). Adjacent terms contain latitude as function $\sin 2\phi$ and $\sin^2 \phi$ called tesseral and sectoral in accordance with loci of solutions on the sphere (see Appendix A for details). The other parameters $\frac{L_0}{L}$, δ and $(\lambda - \lambda')$ in equation (2.24) specify the periodic solutions defined

Argument	Period defined as	1$^{\text{st}}$ term	Caused by
s	Mean lunar tropical month	constant	Declinational change
$(s-p)$	Lunar anomalistic month	$\left(\frac{L_0}{L}\right)$	Orbit ellipticity
$(s-p)-2(h-p)$	Lunar evection period	combination	Perigee revolution – evection
$(s-h)$	Lunar synodic month	combination	Eccentricity revolution – variation

Table 2.1: Arguments of main harmonics functions, their periods and sources (Simon *et al.*, 2013).

by the continuous change of the Moon position with respect to the observer. The expansion of these parameters in time series of harmonic functions exposes diurnal $(\lambda - \lambda')$ and semidiurnal $(2(\lambda - \lambda'))$ periodicities as well as long-term variations depending on δ. In celestial mechanics these periodical solutions of the orbital motion are the main problem consisting of the evection equation solving (Simon *et al.*, 2013). The evection equation serves to define one of the milestones of the celestial mechanics theory – the lunar perigee motion induced by solar attraction (Beutler *et al.*, 2006). Although the gravitational field of the Sun is the strongest in the solar system, tidal solar acceleration is approximately twice as small on the Earth as lunar attraction. By this reason the evection is an even smaller long-term deviation with frequency p (revolution mean perigee of the Moon, see the Table 2.2) which affects $\frac{L_0}{L}$ and lunar longitude λ_l, so that solar TGP is considered simultaneously with lunar tidal forcing (Simon *et al.*, 2013).

2.2.2 Harmonics solutions

A periodic formulation of tidal potential can be obtained by considering the components mentioned above ($\frac{L_0}{L}$, δ and $\lambda - \lambda'$). During the lunar revolution the equatorial coordinates ($\delta, \lambda - \lambda'$) vary with time as the functions of hour angle $\tau = \lambda - \lambda'$, and, additionally, the distance $L = L(t)$ changes due to eccentricity of the orbit. The first term in equation (2.24) represents time-variable multiplier which contains the fortnightly (M_f) long-term variations due to the declination δ changing twice per mean lunar tropical month:

$$\sin^2 \delta - \frac{1}{3} = \frac{1}{3} - \cos 2\delta, \tag{2.25}$$

where lunar declination is circumscribed in the range of $|\delta| < 28°30'$. Another source of long-term variations is the distance perturbations $\frac{L_0}{L}$ (Sidorenkov, 2009; Simon *et al.*, 2013), whose first harmonic corresponds to lunar anomalistic month assigned by argument $(s-p)$. The anomalistic period is the time between double transitions of the pericenter. The other main periodicities are collected in the Table 2.1 (Simon *et al.*, 2013), where fundamental arguments are described in Table 2.2.

A uniform circle orbital motion with period of one mean lunar tropical month is the first order of the lunar orbital motion. The second effect is provided by adding the first term of the

Argument	Description	Period	
s	Mean lunar longitude	Tropic month	27.32 d
p	Mean lunar longitude of perigee	Lunar precession	8.85 y
$l = (s - p)$	Mean lunar anomaly	Anomalistic month	27.55 d
N	Mean lunar longitude of the ascending node		18.61 y
$F = s - N$	Mean lunar elongation counted off from the ascending node	Draconitic month	27.21 d
h	Mean solar longitude	Tropic year	365.24 d
$D = s - h$	Mean lunar elongation counted off from the Sun	Synodic month	29.53 d
p_s	Mean longitude of the perihelion of the Earth		20 940 y
$l' = h - p_s$	Mean solar anomaly	Anomalistic year	365.26 d

Table 2.2: Fundamental arguments (Simon *et al.*, 2013).

distance change $\frac{L_0}{L}$ to describe the elliptic motion with a period of an anomalistic month. The next effect provides periodic solution based on mutual positions the Sun and Moon. The gravitational attraction prevails in conjunctions with the Sun than in quadratures, which induces the period of lunar synodic month (Table 2.1). These periodic solutions (Simon *et al.*, 2013), lunar evection and synodic month, are somewhat more complicated since these non-linear motions are combined. To summarize these terms, the expansion for the distance ratio and longitude can be composed as (Simon *et al.*, 2013):

$$
\begin{aligned}
\left(\tfrac{L_0}{L}\right)^3 &= 1 \quad + C_{ell}\cos(s-p) + C_{evec}\cos(s-2h+p) + C_{var}\cos(2s-2h), \\
\lambda_l &= \dot{s}t \quad + C'_{ell}\sin(s-p) + C'_{evec}\sin(s-2h+p) + C'_{var}\cos(2s-2h),
\end{aligned}
\tag{2.26}
$$

where appropriate coefficients account for effects of ellipticity C_{ell}, C'_{ell}, evection C_{evec}, C'_{evec} and variation of lunar orbit C_{var}, C'_{var}. The connection of these effects with the same variations defined in equation (2.24) for TGP can be expressed by the next link between longitude and declination of the Moon (Simon *et al.*, 2013):

$$
\sin\lambda_l \sin\varepsilon_\odot = \sin\delta \quad \Longrightarrow \quad
\begin{cases}
\sin 2\delta \approx 0 + 2\sin\varepsilon\sin s \\
\cos^2\delta \approx 1 + n\cos 2s,
\end{cases}
\tag{2.27}
$$

so that their corresponding harmonics functions are listed in the Table 2.3. The system of referring to harmonics functions was initiated by Sir William Thomson (Lord Kelvin) in 1882, for instance M_2 and S_2 or already mentioned above M_f, and extended by Darwin (1898) in an *ad hoc* manner later. Currently, numerous side lobes are assigned with arbitrary letter and hold the subscript of species-number in accordance with periodicity, i.e., diurnal ($_1$), semidiurnal ($_2$), terdiurnal ($_3$), quaterdiurnal ($_4$).

The analytical expression for the decomposition of lunisolar tidal potential in equation (2.24)

Argument	Tide	Definition
Lunar diurnal tides		
τ		No principal lunar wave in TGP
$(\tau + s)$	$^{\mathrm{M}}\mathrm{K}_1$	Lunar declinational
$(\tau - s)$	O_1	Principal lunar declinational
$(\tau - s) - (s - p)$	Q_1	Large lunar elliptic, side of O_1
$(\tau - s) + (s - p)$	$\mathrm{M}_1 == \epsilon(\mathrm{O}_1)$	Small lunar elliptic, side of O_1
$(\tau + s) - (s - p)$	$\mathrm{M}_1 == \epsilon(^{\mathrm{M}}\mathrm{K}_1)$	Small lunar elliptic, side of $^{\mathrm{M}}\mathrm{K}_1$
$(\tau + s) + (s - p)$	J_1	Lunar elliptic, side of $^{\mathrm{M}}\mathrm{K}_1$
Lunar semidiurnal tides		
2τ	M_2	Principal lunar
$2\tau - (s - p)$	N_2	Principal (large) lunar elliptic
$2\tau + (s - p)$	L_2	Small lunar elliptic
$2(\tau + s)$	$^{\mathrm{M}}\mathrm{K}_2$	Lunar declinational
$2\tau - (s - 2h + p)$	ν_2	Lunar large evectional
$2\tau + (s - 2h + p)$	λ_2	Lunar small evectional
$2\tau - 2(s - h)$	μ_2	Lunar variational

Table 2.3: Arguments and periods of main harmonics functions caused by Moon tidal generating potential.

into theoretically infinite harmonic functions depended on fundamental arguments listed in Table 2.2 are formulated by Moritz & Müller (1987)

$$V_{\mathrm{TGP}} = \sum_{n=2}^{\infty} \sum_{k=0}^{n} P_n^k(\cos\phi) \sum_j C_{nmj} \cos[\omega_{nmj} t + \beta_{nmj} + m(\lambda - \lambda') + (n-m)\frac{\pi}{2}], \qquad (2.28)$$

where C_{nmj} are appropriate coefficients and harmonic functions are generalized by a simple formula: $C\cos(\omega t - \beta) = A\cos\omega t + B\sin\omega t$, where phase lag $\beta = \tan^{-1}(\frac{B}{A})$. The term $(n-m)\frac{\pi}{2}$ is added for phase shift to provide sinus or cosine parametrization. Frequency of variation ω_{nmj} is a linear combination of time-variable fundamental arguments, namely $s(t)$, $h(t)$, $p(t)$, $N(t)$, and $p_s(t)$ provided in Table 2.2. Accurate calculation formulas for evaluation of these arguments are recommended by the IERS Conventions (Petit & Luzum, 2010) and given in Appendix A.

2.2.3 Specific harmonics of tidal potential expansion

The harmonic functions decomposition utilizes amplitude modulation (Roder, 1931) of a carrier frequency ω_c and a lower modulation frequency ω_m:

$$a_c(1 + a_m/a_c \cos\omega_m t)\cos\omega_c t = \qquad (2.29)$$
$$a_c \cos\omega_c t + \frac{a_m}{2}\cos(\omega_c + \omega_m)t + \frac{a_m}{2}\cos(\omega_c - \omega_m)t,$$

where a_c and a_m are amplitudes of the carrier and modulation waves. Equation (2.29) illus-

trates that any decomposition provides three harmonic functions: the principle wave is dependent on carrier frequency and two functions represent side bands separated by modulation frequency ω_m relative to ω_c. In absence of the modulation frequency ω_m, the carrier frequency ω_c exemplifies a single harmonic function. In this case, the lunar revolution motion will be a uniform circular motion of the zero-inclination orbit. The presence of modulation frequency $\omega_m \neq 0$ is evidence of non-uniform motion as far as variations are conditioned by distance and declination change. In the tidal potential this wave is called the principal tide (Simon *et al.*, 2013), namely the lunar M_2 (or solar S_2), the argument for which can be seen in the Table 2.3.

The decomposition of the tidal potential contains the principal lunar M_2 tide supplied with elliptic side lobes N_2 and L_2 due to distance variations. N_2 is larger than L_2 and called the principal or large lunar elliptical and small lunar elliptic correspondingly (Simon *et al.*, 2013). In the diurnal band halving M_2 the carrier is absent and, by this reason, O_1 is defined as the principal lunar declinational tide and $^{M}K_1$ is another side lobe (Simon *et al.*, 2013). Also, large lunar elliptic wave Q_1 is the side lobe of O_1. The other lunar elliptic wave J_1 is smaller because it is the side of $^{M}K_1$. Even smaller variations belong to evectional and variational tides (Sidorenkov, 2009): ν_2, λ_2 and μ_2 .

The decomposition (2.29) is fruitful in generating harmonic functions. One of resultants of this approach is the existence of several harmonics of nearly equal arguments. These harmonics can be combined, since the period and trigonometric arguments are common. For instance, $^{M}K_1$ carrier and solar harmonic $^{S}K_1$ are combined wave of the lunisolar K_1 tide. These waves are indistinguishable due to propagation with the same angular velocity $\tau + s = t + h$. In addition, a similar combination is spotted in the semidiurnal band, where $^{S}K_2$ and $^{M}K_2$ are an inseparable lunisolar wave K_2 (Sidorenkov, 2009).

The combined tides are able to indicate processes of physical origin which derive from tidal potential indirectly. In the diurnal band there is no principal solar or lunar harmonic wave with period equal exactly to 1 cycle per solar day (Simon *et al.*, 2013), and so the observed signal is related to the atmospheric origin. The closest appropriate gravitational S_1 line is a product of two side bands of the solar tidal potential expansion (Sidorenkov, 2009):

$$S_1 \quad \begin{cases} \epsilon(P_1): & (t-h)+(h-p_s) \\ \epsilon(^{s}K_1): & (t+h)-(h-p_s) \end{cases} \tag{2.30}$$

These waves are separated by the long-term argument p_s with period of variation 20 940 y. This long-term motion characterizes the revolution of the Earth's perihelion, which can be omitted in a first-order approach, but modern tidal tables include both lobes (Petit & Luzum, 2010). As a result, the definition of S_1 exemplifies a combined tide of two lobes of non-principal carriers, and thus the contribution of these harmonic is small. Amplitude oscillations driven by TGP are widely referred to as gravitational tides. This duality (Ray & Egbert, 2004) leads to a common confusion resolved partially by nomenclature: radiational S_1 tide is a combined tide of frequency

15°/h and gravitational tide S_1 is the largest wave in equation (2.30) – $\epsilon({}^s K_1)$.

2.2.4 Major ocean tides

The fundamentals of tidal potential imply oceans to be in equilibrium. The equilibrium theory considers tidal forcing compensated with the sea level surface elevation for a hypothetical case in which the Earth is covered entirely by oceans which response instantaneously. Tidal heights over the Earth's surface can be obtained on the basis of this equilibrium assumption (Pugh, 1987)

$$\zeta_E = \frac{V_{\text{TGP}}}{g} \tag{2.31}$$

driven explicitly by TGP of the Sun and Moon. The equilibrium tide is the second degree spherical harmonic, thus in the realistic case when the Earth responses as elastic body the corresponding amplitudes are modified by the factor of $(1+k_2-h_2)$. The elastic constants k_2 and h_2 are known as the body tide Love numbers of the second degree and liable for the mass redistribution of the gravitational potential and surface distortions (Pugh, 1987). The body tide Love numbers, however, take different values for the diurnal and semidiurnal bands due to FCN resonance (Sasao & Wahr, 1981), so that equilibrium tidal amplitudes in accordance with equation (2.24) and (2.28) are divided into a long-term (l), diurnal (d) and semidiurnal (s) periodicities:

$$\zeta_{E_l} = C_l 3(\sin^2 \varphi - \frac{1}{3}) \qquad \zeta_{E_d} = C_d(\sin 2\varphi) \qquad \zeta_{E_s} = C_s(\cos^2 \varphi), \tag{2.32}$$

where C_l, C_d and C_s are appropriate coefficients for each set where Love numbers are already included and can be found, e.g. in the work by Arbic *et al.* (2004). However, in general a tide's propagation over the real globe is different from the equilibrium case due to existence of land surface and ocean bottom topography, currents and ocean bottom friction, as follows Coriolis forces and dissipation processes take place as well.

The set of the largest signals specified in equation (2.32) includes usually three long-term tides and four diurnal and four semidiurnal dominant harmonics. The long-term variations are lunar fortnightly M_f, lunar monthly M_m and solar semiannual constituent S_{Sa}. Diurnal lunar O_1 and Q_1, solar P_1 and lunisolar K_1 and semidiurnal lunar M_2 and N_2, solar S_2 and lunisolar K_2 are called eight major tides. The principal solar declinational tide P_1 is derived from solar potential by analogy to O_1. The main power of lunisolar tides in the diurnal band is provided by the K_1 tide. The principal lunar M_2 tide is the greatest wave in the considered high-frequency bands. Next sizable amplitude in the semidiurnal band originate from the principal solar S_2 tide, which is larger than the N_2 tide and the lunisolar K_2 tide.

2.3   Atmospheric contribution

Effects of smaller order than the gravitationally induced ocean tides belong to atmospheric variations. The oscillations of the atmosphere are forced by daily insolation and classified as radiational tide following by Munk & Cartwright (1966). The principal excitation mechanism is non-gravitational, which is a distinctive property of atmospheric tides in comparison with ocean tides. This mechanism can be specified by the dependence on solar radiation $\mathscr{R}_\odot$ expressed by a plain statement:

$$
\begin{aligned}
\mathscr{R}_\odot &\propto \frac{\vec{R_\odot}}{R_\odot}\cos\psi, \quad \text{where} \quad -\frac{\pi}{2}\leqslant\psi\leqslant\frac{\pi}{2} \qquad \text{– day,} \\
\mathscr{R}_\odot &= 0, \qquad\qquad\qquad\qquad\qquad\qquad\quad \text{– night,}
\end{aligned}
\tag{2.33}
$$

so that the vector $\mathscr{R}_\odot$ is directed to the Sun. This step function approximates the main pattern (Munk & Cartwright, 1966) of the atmospheric S_1 tide, occurring once per solar day. Realistic variations in the Earth's rotation variations can be shown by describing the so-called radiational potential. A different thermodynamic approach is developed in the atmospheric science for the weather modeling. Utilizing this approach the tidal signals in atmospheric pressure fields can be calculated to represent the crust deformation forced by the atmosphere. Besides, this atmospheric loading induces a hydrodynamic ocean response, which is the secondary order effect related to the atmospheric contribution. Overall, these models are practical for any geodetic analysis.

2.3.1   Atmospheric tides as derived from tidal potential

By analogy with the gravitational potential expansion, the function $\mathscr{R}_\odot$ in equation (2.33) can be substituted by Legendre polynomials and decomposed by into the harmonics functions (Munk & Cartwright, 1966). Consequently, the major atmospheric tidal admittance relates to arguments of the S_1, seasonal annual S_a, K_1 and P_1 tides. The radiational S_1 tide is the pivotal wave in the diurnal band corresponding to the 1$^{\text{st}}$ degree Legendre polynomial, and the K_1 and P_1 tides produce significantly smaller variations (Ray & Egbert, 2004). A determination of the radiational S_1 tide is supported by the absence of strong signal in the tide generating potential. In view of the fact that the K_1 and P_1 tides are the main ocean tides, an analysis of their small radiational components is corrupt by the gravitational parts (Ray & Egbert, 2004). The second degree harmonics are represented by the same frequencies as tide generating potential, i.e., semidiurnal waves, where the radiational S_2 tide is smaller than the major ocean S_2 tide (Arbic, 2005).

2.3.2   The thermodynamic approach

Effects of atmospheric tides were determined (Hagan *et al.*, 2003), first of all, in pressure field variations. Following thermodynamic laws, temperature and density variations contain these sig-

nals as well as the wind patterns and geopotential heights. Currently, the radiational atmospheric tides are explained primarily by the water-vapor and ozone radiational absorption (Ray & Ponte, 2003), which induces atmospheric pressure oscillations through the upper-atmosphere heating.

Atmospheric tides are divided into migrating and non-migrating tides. Both oscillations possess the same periods but propagate in opposite directions. This fact can be illustrated by a general expression:

$$A\cos(N_\omega \omega t - N_A \lambda - \varphi) \tag{2.34}$$

where A is the variation amplitude, $\omega = (2\pi/24)\mathrm{h}^{-1}$ is the wave frequency, positive N_ω number denotes nth harmonic frequency, and λ is longitude, N_A is the wave number, which specifies the number of peaks over the same latitude. Positive values of N_A indicate eastward tidal propagation and negative values reveal westward movement. Migrating solar tides are defined as waves for which $N_A = -N_\omega$, thus for diurnal waves $N_A = -1$ and $N_\omega = 1$ and for semidiurnal $N_A = -2$ and $N_\omega = 2$. These waves propagate westward and vary equally along the same meridian. Thus, the migrating solar tide is Sun-synchronized and the rest of the waves with the same period are nonmigrating tides.

Both migrating and nonmigrating waves relate to the vertical component of the tide. The absorption processes of radiation, which run equally for all latitudes along the same meridian, produce migrating tides. The solar radiation penetrates all layers, so that these variations can be observed at any height. In particular, some layers are important to mention: at 150 km level the layer of atomic oxygen absorbs extreme ultraviolet; closer to the ground, at the altitudes of 100-150 km, molecular oxygen absorbs far-ultraviolet; the next barrier (30-70 km) of ozone layer absorbs the ultra-violet radiation and the rest (infrared radiation) is absorbed by water vapor in the lowest atmosphere. The diurnal oscillations of migrating tides initialized in the troposphere grow with altitude with respect to the conservation law because of the matter density decrease. The migrating semidiurnal tides have their primary source higher than diurnal, but often occur with large amplitude owing to favorable vertical propagation characteristics (Dai & Wang, 1999; Hagan & Forbes, 2002). The nonmigrating tides show a different behavior over the same meridian because of their origin in longitude-dependent factors such as topography, land-sea contrast and zonal variations. The practical distinction between these types of waves is complicated and requires a reasonable number of measurements along the same longitude as well as spatial distribution of ground-based techniques, for which upper layers are not attainable. Altitude data are, however, available and obtained usually from low orbit satellites, for instance, the Upper Atmosphere Research Satellite at the 585 km orbit (The National Aeronautics and Space Administration (NASA) project `science.nasa.gov/missions/uars/`).

A model of atmospheric tides observed in the surface pressure field variations is required for the geodetic ground-based systems. These variations can be obtained from the European Centre for Medium-Range Weather Forecasts (ECMWF) data set (Ray & Ponte, 2003), for example.
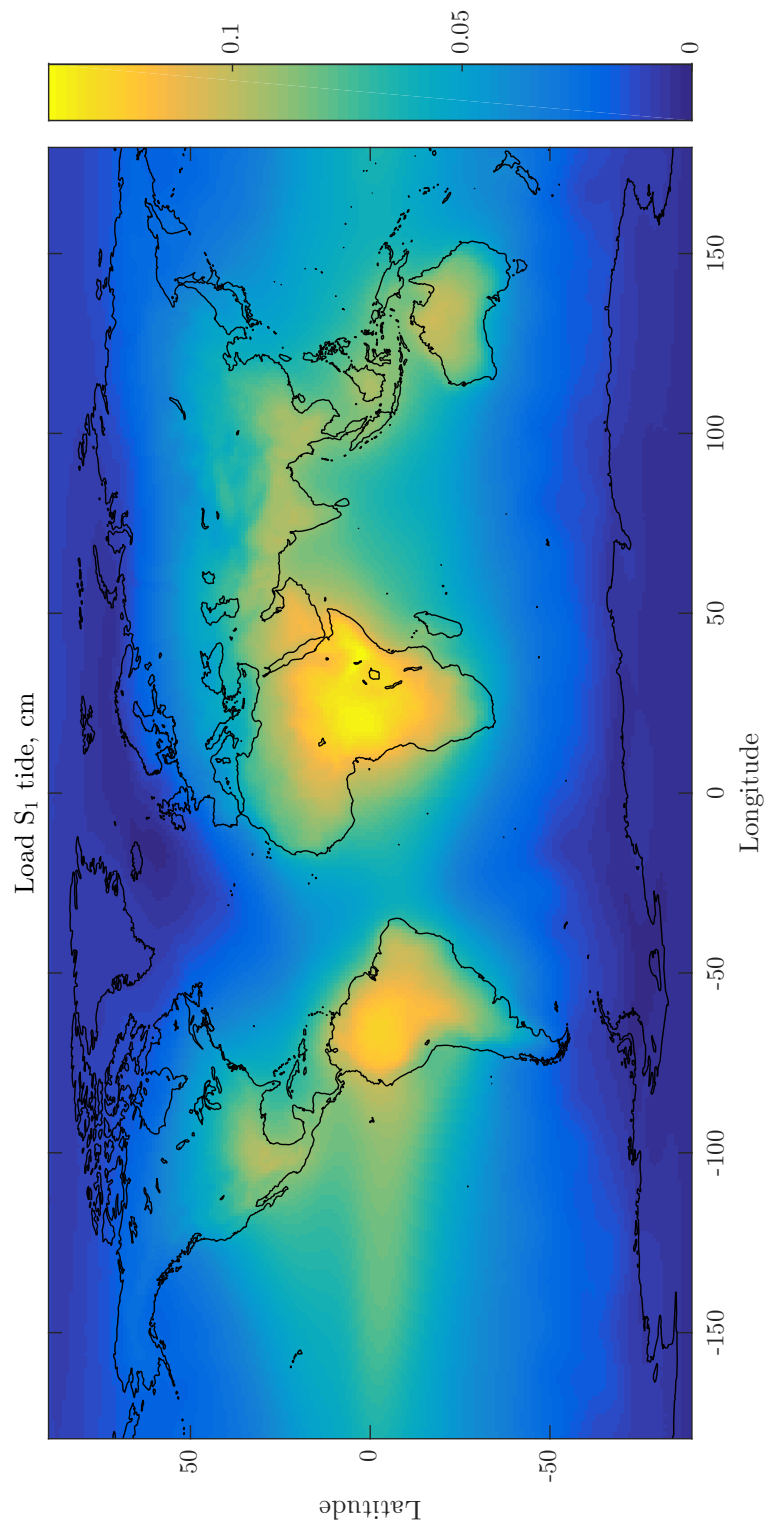
Figure 2.3: Amplitudes of the atmospheric loading S_1 tide are provided by Vienna University of Technology (TU Wien). The corrections are shown in cm.
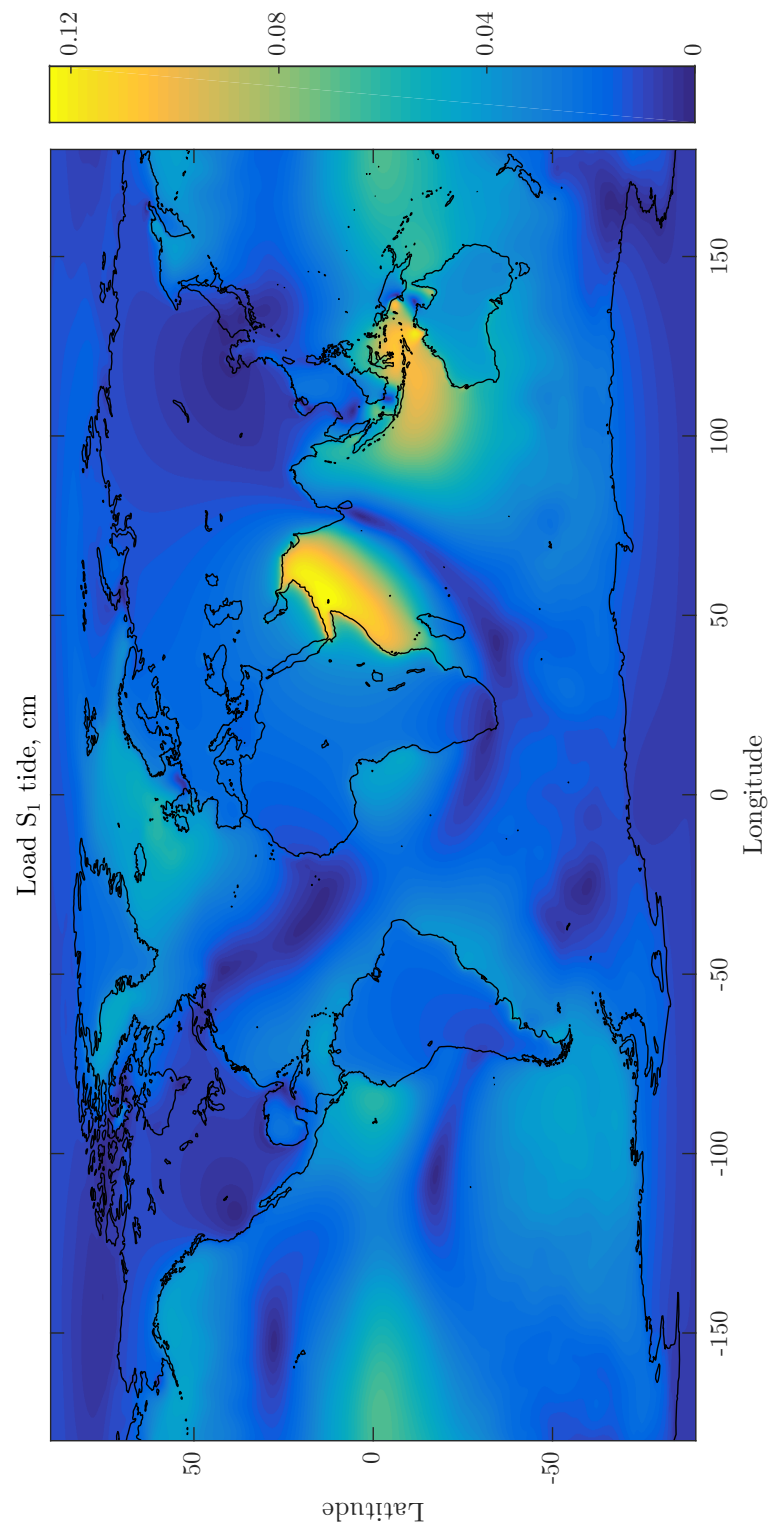
Figure 2.4: Amplitudes of the load S_1 tide are provided by Finite Element Solution (FES)2014b. The corrections are shown in cm.

The commonly applied approach to process this data (Ponte & Ray, 2002) was used to produce the TU Wien atmospheric loading model (Wijaya *et al.*, 2013). The corresponding atmospheric loading amplitudes for S_1 demonstrate (Figure 2.3) typical corrections. This model can be implemented in the geodetic analysis directly, because the load tide represents the crust deformation (see Appendix A). Also, the angular momentum approach utilizes the surface pressure variations to evaluate Earth Rotation change (Gross, 2015). Because of considerable amount of the globally distributed pressure field measurements, angular momentum approach provides currently more accurate the Earth rotation tide model than geodetic observations. Thus, these geophysical estimates serve as a reference to the atmospheric tide terms determined in this thesis by means of VLBI observations.

2.3.3 Secondary processes related to atmospheric tides

Based on the work by Ray & Ponte (2003), where the diurnal pressure pattern is clearly illustrated, Ray & Egbert (2004) discuss the excitation mechanism for the S_1 variations in the ocean. It is concluded that the S_1 atmospheric tide excites the hydrodynamic response. The achievements of this work are partially confirmed by the research of Dobslaw & Thomas (2005) utilizing a more complicated 3D ocean model used for processing of Gravity Recovery and Climate Experiment (GRACE) data.

This hydrodynamic ocean response to the atmospheric forcing at the major diurnal frequency is assumed to induce sea level anomalies of about 1 cm. In the modern ocean model FES2014b (Lyard *et al.*, 2006) the so-called oceanic S_1 tide (Figure 2.4) is given in form of the crust deformations (see Appendix A). These signals hardly attain a couple of millimetres (Figure 2.4).

Besides radiational effects, the gravitational pull of the atmospheric masses due to the Sun and Moon also excites atmospheric tides (Hagan *et al.*, 2003). Specifically, the lunar atmospheric tides present about 5-10 % of the atmospheric tidal impact. These significantly smaller effects can be detected in the pressure field variations (Hagan *et al.*, 2003), and their amplitude estimates were evaluated recently in the preliminary results of the GRACE product (Dobslaw *et al.*, 2017). However, on the millimetre accuracy level of VLBI cannot be measured and, thus it is not supposed to affect the obtained results.

Chapter 3

The VLBI method

Nowadays, Very Long Baseline Interferometry (VLBI) is one of the widely used measurement methods in space geodesy. With the VLBI method, distant radio sources are observed, giving a valuable advantage among other techniques. That is a possibility to relate the Celestial Reference System (CRS), thus the entire transformation between celestial and terrestrial reference systems is employed in VLBI observations. The Earth Orientation Parameters are quantities to define this transformation. Since the Celestial Reference Frame (CRF) is fixed to the sources, which are considered as standard lighters, all deviations of the real Earth are divided into the Earth rotation variations, station position deformations and light propagation path through the atmosphere.

This chapter presents a general description on the VLBI method and data processing recommended by the IERS Conventions. In particular, the minimal set of models required for the VLBI analysis is reviewed and an extension with regard to the geophysical models is discussed.

3.1 Very Long Baseline Interferometry

The Very Long Baseline Interferometry (VLBI) network embraces scores of radio antennas spread around the world. The primary idea of the VLBI method is to make an interferometer from at least two radio antennas separated by a distance of thousands kilometres, which observe the same radio source simultaneously. This distance is a receiver's base, which, in the application to VLBI, is called a baseline $\vec{b}$ shown in Figure 3.1, and, in general, is an analogue of a single dish aperture's size. By changing the aperture's size by a thousand times from a single dish to a baseline, VLBI achieves unprecedented resolving power by accumulating synchronized data from remote antennas while capabilities of each of the single dish remain unchanged. The angular resolution characterizes this ability to separate details of the objects on the celestial sphere. The longer the length of the baseline can be reached between two antennas, the better angular resolution α can be obtained. Because the angular resolution α is defined by the function of the baseline length $|\vec{b}|$ for the interferometer which receives a radiation of a wavelength λ:

$$\alpha \propto \lambda/|\vec{b}|, \tag{3.1}$$
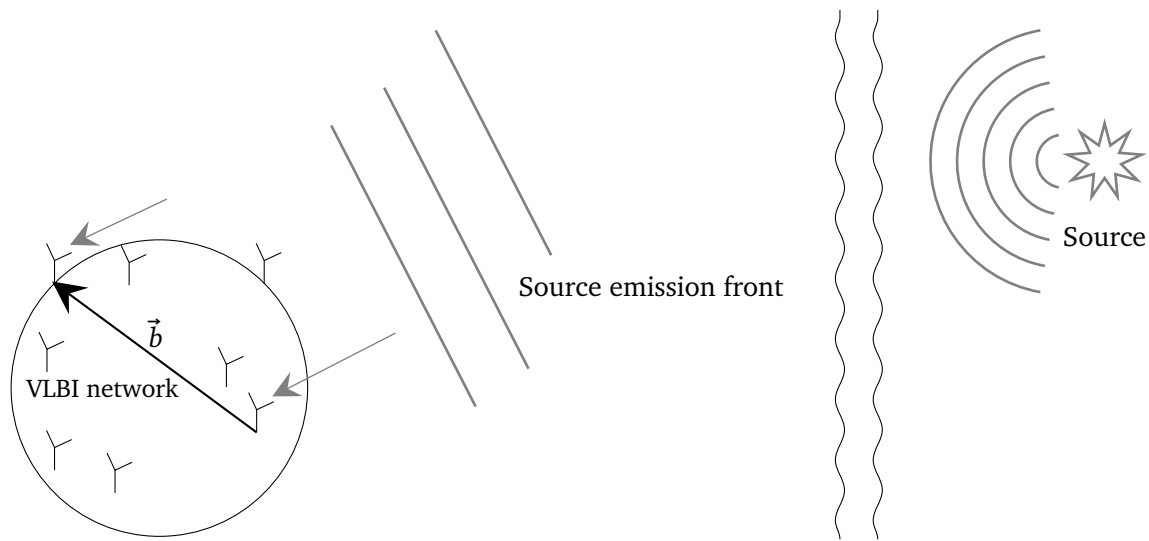
Figure 3.1: An illustration of the VLBI principle.

the observations on the longest baselines are benefited for the VLBI accuracy. For a single observation this resolution can achieve approximately 1 mas with the wavelength approximately 3.5 cm for the longest singular baseline length of about 12 000 kilometers. Because a regular VLBI network, on average, consists of 6-9 antennas which compose 15-36 baselines growing with a binomial law dependence, a post-processing analysis of this single routine session might allow the achievement of the angular resolution α about 0.1 mas. Further post-processing analysis methods can enhance this angular resolution even more by considerable amount of the long baselines. Additionally, a certain decrease of the signal accumulation time (that time during which one source is observed simultaneously on network) permits to collect a large number of observations what improves a statistical assessment (formal error level given by VLBI analysis). This strategy is made available, first, by observing reasonably strong sources and, second, by upgrading the equipment on the stations and building new antennas. However, a multi-baseline VLBI is depended highly on the equipment of each antenna, so that the least sensitive receiver will define most of the accumulation time of the whole network.

Concurrent observations on the multiple baselines can determine three ERP independently (Moritz & Müller, 1987), while observations on one baseline can provide only two of these parameters. The ERP set is situated in the plane perpendicular to the baseline, so that baselines spread between North and South are sensitive more to the polar motion and East-West baselines couple to dUT1. At practice the parameter of network geometry is found convenient to associate baselines with Earth Orientation Parameters (EOP). In this regard EOP estimates from regional networks, which are composed on comparatively short baselines, were shown to be less accurate (Malkin, 2009) due to insufficient network geometry (Dermanis & Mueller, 1978). This problem can not be resolved with increasing of observation number, the latter, however, can improve a statistical assessment of coordinates per station and source.

The other factor defining the angular resolution α included in equation (3.1) is the wave-

length λ. The VLBI method is designed to observe in two well-separated bands, X of 3.5 cm and S of 13.5 cm. The data obtained in the shorter X band are processed in the further analysis which gives about 4 times better resolution than the S band (Sovers *et al.*, 1998). The observations in S band are conducted only for reductions of the ionosphere, which is the upper layer of the atmosphere consisting of free electrons and ions dispersing the electromagnetic wave propagation, what affects all geodetic techniques (Alizadeh *et al.*, 2013).

The VLBI method operates in several channels of each of X and S bands, which, first of all, get correlated to measure rough signals, and, then, the band-width synthesis is applied using fringe fitting to determine accurate group delays, phases and phase rates for each channel. The term 'group' marks this fact that each band is divided into several channels, where the standard mode implies this separation for the X band in 8 channels and the S band in 6 channels. All these channels include ionosphere delays for two distinct bands, X and S, used to calculate group delay differences between these bands in order to "calibrate" ("correct") the group delays. The mathematical approach to correct for the ionospheric delay is used as described in the IERS Conventions (Petit & Luzum, 2010) in more details.

The VLBI method was designed to achieve the unprecedented angular resolution amongst other observing systems. The celestial reference objects observed by VLBI method are supposed to be point-like bodies even using high angular resolution. These astronomical objects are radio sources at considerable distances of several billion light years which emit strong electromagnetic signals (as a rule) and are called quasi-stellar objects of continuous radiation, or QSO, or quasars (Schmidt, 1963). Quasars are known as active galactic nuclei because of intense radio emission. Given the combination of physical properties, powerful luminosity and the distance, quasars are near-perfect markers on the sphere; thus they can provide a quasi-inertial reference frame, which is in high demand in geodesy. As a deterrent, the source structure was detected for a majority of quasars and for some of them the images were created (Charlot, 1990). The number of quasars is uncountable and observations for a single image building require substantial effort. The spatial and time variability of quasars contribute to error propagation (Charlot, 1990). Overall, quasars are in high demand for establishing a celestial reference frame (Fey *et al.*, 2015) regardless to the recognized deficiencies, because only these objects can provide access to the CRS with the necessary accuracy as long as there are no better standard lighters yet discovered.

One of the main advantage of using quasars is remoteness used to assume that the wave front from the source is parallel (Figure 3.1), where the radio source emission center is in direction of the vector $\vec{s}$ (Sovers *et al.*, 1998). In general, the observations of the sources are the time readings, which are the main input parameter for the post-processing analysis and used to calculate group delay. Literally, the term 'delay' signifies that parallel signals from the quasars are not detected at the exactly same time (Figure 3.2), but in the time t_1 at one site and t_2 at second site, delayed
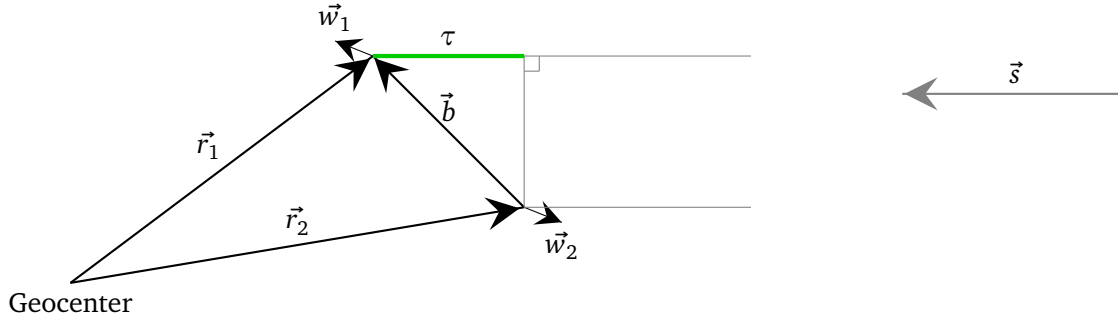
Figure 3.2: The geometrical VLBI principle is illustrated for two antennas with geocentric coordinates $\vec{r}_{i=1,2}$, which generate baseline vector $\vec{b}$. The parallel front from the source $\vec{s}$ receives with time delay τ.

by time τ with respect to the first observation (Petit & Luzum, 2010):

$$\tau = t_2 - t_1 = -\frac{\vec{b} \cdot \vec{s}}{c} + \tau_{\text{grav}} + \Delta L_1 \frac{\vec{s} \cdot (\vec{w}_2 - \vec{w}_1)}{c} + (\Delta L_2 - \Delta L_1), \qquad (3.2)$$

where the baseline vector $\vec{b} = \vec{r}_2 - \vec{r}_1$ between two antennas with geocentric coordinates $\vec{r}_{i=1,2}$ and respective geocentric velocities $\vec{w}_{i=1,2}$, c is the speed of light, τ_{grav} is the gravitational delay with respect to the general relativity principle, $(\Delta L_2 - \Delta L_1)$ is the propagation delay in the atmosphere, so that term $\Delta L_1 \frac{\vec{s} \cdot (\vec{w}_2 - \vec{w}_1)}{c}$ denotes this difference in time delay due to the medium attendance, which is not the vacuum. By disregarding the propagation delay in atmosphere $(\Delta L_2 - \Delta L_1)$ the reduced form of equation (3.2) is called the geometric delay and demonstrates the so-called geometric principle of the observed delay in VLBI.

The analysis centers process obtained group delays to estimate station and sources positions and EOP together with troposphere and clock parameters. To achieve this goal various modifications of the Least Squares Adjustment (LSA) are introduced. Regardless of the particular method the main procedure stays the same: reductions as recommended by Petit & Luzum (2010) are implemented to obtain the theoretical delays which are calculated 'C' values to complete a pair 'O'-'C', where 'O' is the observed group delays. The LSA is then applied to find the closest fit to the differences 'O'-'C'. Namely, based on the theoretical approach given by equation (3.2) and called the total delay τ forms 'O'-'C' with the group delay. The rest of recommended reductions are mainly applied to the station coordinates and EOP and discussed in section 3.2.

3.1.1   In comparison with other observing methods

The VLBI method represents a highly accurate and precise measurement technique for a simultaneous realization of celestial and terrestrial object positions as well as the Earth axis orientation in space as independent parameters in the EOP set. The other geodetic techniques Global Navigation Satellite System (GNSS), Satellite Laser Ranging (SLR), Lunar Laser Ranging (LLR) and Doppler orbitography and radio positioning integrated by satellite (DORIS) can report EOP as a

dependent set only (Gross, 2015).

These geodetic systems support a monitoring of Earth rotation, but each of them was designed for the different purposes. First on the list, GNSS is based on a two-segment system a ground network and a satellite segment. Systems with the largest constellations are Global Positioning System (GPS), GLObal NAvigation Satellite System (GLONASS) and Galileo. The fundamental of GNSS is that the ground segment receives satellite-transmitted signals for the high-accurate spatial positioning. The other geodetic techniques, SLR and LLR, are designed to measure the round laser-beam track from the ground station to a special satellite or a lunar reflector accordingly. The last one, DORIS is based on measurements of the Doppler effect and is designed for precise orbit determination as required for altimetry/ocean applications. All these geodetic observing systems have an orbit determination problem in common, i.e., polar motion and LOD can be obtained as independent parameters only. The last one, DORIS represents the least accurate solution for these parameters, mainly due to a significantly smaller constellation of satellites and ground network than GNSS. Weather conditions are problematic for SLR and LLR, however SLR analysis is that one included in the combined solution for EOP and provides pole coordinates at the 3 to 5 order worse estimated uncertainties (Gambis *et al.*, 2015) than VLBI ($\approx$70 mas by International VLBI Service for Geodesy and Astrometry (IVS)) and GNSS ($\approx$40 mas by International GNSS Service (IGS)) methods correspondingly. Also, single-technique solutions for EOP from the VLBI and GPS were found to be in a good agreement (Artz *et al.*, 2012). Yet, routine GPS solutions show a better accuracy than VLBI in polar motion and, at the same time, VLBI solutions of dUT1 exhibit a similar accuracy level as achieved for LOD from GPS (Gambis *et al.*, 2015). In general, VLBI results are affected by some deficiencies mainly due to the available global coverage of the network which is inferior to the GNSS network and, consequently, the number of observations obtained by GNSS is significantly large than VLBI can afford. This advantage highlights GNSS among other satellite-based observing systems, because the number of observations in processing decreases the formal errors of any estimates. Still, the resonance with orbital satellite periods limits GNSS analysis in the high-frequency band of Earth rotation, where the VLBI analysis provides the high-frequency dUT1 and polar motion variations without a lack of signals in the diurnal band and usually more accurate account in semidiurnal band.

All operated observing systems, including VLBI, report the coordinates of CIP, while the ring laser gyroscope technique is designed to sense the instantaneous Earth's rotation axis (Mendes Cerveira *et al.*, 2009). Analyzing ring-laser data might have been a solution for variety of geodetic problems including the subject of this thesis – atmospheric tides (Schreiber *et al.*, 2004). First attempts to evaluate the effects of ocean tides from ring-laser observations were undertaken recently (Tercjak & Brzeziński, 2017), but numerous technical issues must be solved before presenting any ocean tide model in Earth rotation. This gyroscope at station Wettzell in Germany can be maintained in a stable observing mode for several hours and days, and currently about 100 days are available for processing (Tercjak & Brzeziński, 2017). Such new techniques can provide more opportunities, for instance, in combination with VLBI and GNSS. Because this is the only one station operated now in testing mode, an improvement might be seen in future.

3.2   Applied reductions

The IERS Conventions (Petit & Luzum, 2010) define the term "reductions" as models which represent various geophysical effects. Their accuracy is expected to suffice the 1 mm level in terms of station positions. To conduct a reliable processing, reductions are required to be obtained independently on the VLBI analysis or the other geodetic observing systems. Besides, if any constraints are applied to calculate reductions, they should not be provided by the VLBI analysis. The set of reductions is divided into station positions, EOP and light propagation. In the current processing, the main departure from the set of models recommended by the IERS Conventions is the inclusion of geophysical corrections for the station positions to take into account the non-linear effects.

3.2.1   Station positions

In VLBI analysis one of the main outcome or "product" in conventional terminology is the International Terrestrial Reference Frame (ITRF). The realization of the ITRF is provided by linear station positions $\vec{X_0}$ and velocities $\dot{\vec{X}}$ at the reference epoch t_0:

$$\vec{X}(t) = \vec{X_0} + \dot{\vec{X}}(t - t_0), \tag{3.3}$$

where t is a moment of observation, on which coordinates $\vec{X}(t)$ are requested. Most of solutions are obtained on the basis of the ITRF2014 unless it is specified otherwise. The other realization applied in the current processing is the VieTRF13 (Krásná, née Spicakova, 2014). After the release of the last official ITRF2008, this intermediate solution VieTRF13 was chosen to be an internal model for the data analysis implemented in Vienna VLBI and Satellite Software (VieVS) commonly used at the TU Wien.

The stations are placed on the ground of the Earth, and each component of the network, thus, experiences the same deformations as the underlying crust. The ITRF definition expects the applications of time-dependent corrections $\Delta\vec{X_i}(t)$ listed in Table 3.1 as additions to the reported reference points in order to obtain the instantaneous station positions $\vec{X_I}(t)$:

$$\vec{X_I}(t) = \vec{X}(t) + \sum_i \Delta\vec{X_i}(t) \tag{3.4}$$

The range of these reductions varies from those driven by Earth's gravitation itself and movements in the presence of gravitational fields raised from Sun and Moon; to that ones due to irregular effects. Those models are referred to as solid Earth tides (Mathews *et al.*, 1995) and ocean tides. Also, the IERS Conventions recommend the cubic model of secular motion of the pole, so-called mean pole and rotational deformations due to polar motion. And, the model by Desai

Reduction	Model by	Value
Solid Earth tides	(Mathews *et al.*, 1995)	up to 40 cm
Ocean tidal loading	varied	10 cm
Pole tide loading (cubic model)	IERS Convention model	several cm
Ocean non-tidal loading	varied	1 cm
Atmospheric non-tidal loading	varied	2.5 cm
Hydrology loading	varied	< 1 cm
Atmospheric tidal loading	varied	< 2 mm
Ocean pole tidal loading	(Desai, 2002)	up to 2 mm
Post-seismic deformations for ITRF2014	-	up to 80 cm

Table 3.1: Various effects on the displacements of reference positions on the crust.

(2002) is to account for this centrifugal effect of polar motion called ocean pole tide included in conventional set of reductions as well. These effects contribute mainly to the low-frequency band of periods of 14 and 12 months. The periodic effects due to ocean tides are taken into account by ocean tidal loadings provided by, for instance: FES (Lyard *et al.*, 2006), Empirical Ocean Tide Model (EOT, Savcenko & Bosch, 2012), TOPEX/Poseidon global tidal model (TPXO, Egbert & Erofeeva, 2002). For all these series, on-going and updated versions can be found. Based on some of these models, the special services by Bos & Scherneck (2007) or by Petrov (2015) report the corresponding site-dependent coefficients represented by amplitudes A_{cj} and phases φ_{cj}. The resultant vector Δc is computed by substituting these amplitudes and phases in the expression similar to the equation (2.28), where astronomical argument is described by $\psi_j(t)$ for 11 tides in total:

$$\Delta c = A_{cj} \cos(\psi_j(t) - \varphi_{cj}). \tag{3.5}$$

The account of ocean tides was agreed to use only 8 major ocean tides in diurnal (K_1, O_1, P_1 and Q_1) and semidiurnal (M_2, S_2, N_2, K_2) bands and 3 long-term tides (M_f, M_m, S_{Sa}). The obtained vector Δc is one of the corrections $\Delta \vec{X}_i$ to the chosen station.

The other regular variations are due to the signals at the frequencies $\omega(S_{1,2}) = 1, 2$ cycles per day of the S_1 and S_2 tides. The atmospheric tides utilized in this analysis are provided by next services by Petrov (2015); van Dam (2010); Wijaya *et al.* (2013). The corresponding station displacement can be calculated similar to ocean tides:

$$\Delta S_{1,2} = A_c(S_{1,2}) \cos(\omega(S_{1,2})T) + A_s(S_{1,2}) \sin(\omega(S_{1,2})T), \tag{3.6}$$

where $A_c(S_{1,2})$ and $A_s(S_{1,2})$ are the harmonic coefficients per station, T is time moments t in days of the Universal Time (UT1).

Both corrections, Δc and $\Delta S_{1,2}$, are usually given in so-called REN-system. REN-system is

the local rectangular reference system, whose axes are placed along with Radial, East and North directions in topocentric system. These corrections in REN require the transformation to the geocentric reference frame $(\vec{X}_i = (\Delta X, \Delta Y, \Delta Z))$ for reductions as follows

$$
\begin{pmatrix} \Delta X \\ \Delta Y \\ \Delta Z \end{pmatrix} = \Omega \cdot \begin{pmatrix} \Delta R \\ \Delta E \\ \Delta N \end{pmatrix}, \tag{3.7}
$$

where Ω is the rotation matrix on two angles of the site ellipsoidal latitude φ and longitude λ correspondingly:

$$
\Omega = \begin{pmatrix} \cos\varphi\cos\lambda & -\sin\lambda & -\sin\varphi\cos\lambda \\ \cos\varphi\sin\lambda & \cos\lambda & -\sin\varphi\sin\lambda \\ \sin\varphi & & \cos\varphi \end{pmatrix}, \tag{3.8}
$$

Additionally, the non-linear effects derive from the atmospheric thermodynamic processes and hydrodynamic interactions in the ocean system. In reductions these effects can be taken into account by ocean and atmosphere non-tidal loading models. In this thesis, non-tidal atmospheric loading is provided by TU Wien (Wijaya *et al.*, 2013) and Goddard Space Flight Center (GSFC) (Petrov, 2015). Non-tidal ocean model is spread separately by Estimating the Circulation and Climate of the Ocean, Phase II (ECCO2, Menemenlis *et al.*, 2008) or as a part of non-tidal atmospheric loading (Carrére & Lyard, 2003). The consistency of the ECCO2 with TU Wien or GSFC is doubtful because this model might have a lack in modeling (Menemenlis *et al.*, 2008). Notwithstanding a non-linear geophysical model inclusion in reductions is not a part of the IERS Conventions, geophysical corrections due to atmospheric non-tidal loading provided by TU Wien and hydrology by GSFC are applied for each solution undertaken in this study. Since a consistent non-tidal ocean model with TU Wien was not found, in the current reductions these geophysical effects are not introduced.

The other kind of non-linear deformations arises from the fact, that the Earth structure itself is somewhat different from a simple solid model; the Earth body experiences deformations as an elastic body, cf. the IERS Convention model. Recently, post-seismic deformations for ITRF2014 were released to take into account some part of the deformation effects (Altamimi *et al.*, 2016). These effects are approximately up to 30 cm in average and up to 80 cm in maximum can be seen for specific station. These corrections represent the major difference with respect to the previously used VieTRF13 for the high-frequency ERP analysis (Girdiuk *et al.*, 2016b).

3.2.2 Light propagation

The quasar's light detected by the ground network passes through the atmospheric layers where it undergoes atmospheric propagation delay. Whereas ionospheric part of this delay can

be accounted for by dual-frequency band observations in VLBI, the path going through the troposphere needs a special treatment. By the accepted approach (Nilsson *et al.*, 2013), the tropospheric delay can be divided into a hydrostatic (h) and a wet part (w) of zenith delay ΔL

$$\Delta L = \Delta L_h^z \cdot mf_h(e) + \Delta L_w^z \cdot mf_w(e), \qquad (3.9)$$

where e is the elevation angle, ΔL_h^z is a priori zenith hydrostatic delay (accurately determined, e.g. in the paper by Davis *et al.*, 1985) and ΔL_w^z is the wet delay part (usually estimated in the analysis of geodetic observations). The corresponding mapping functions $mf_h(e)$ and $mf_w(e)$ are used as provided by Vienna Mapping Function 1 (VMF1, Böhm *et al.*, 2006) to describe a thickness of the atmosphere by the ratio of the slant delay to the delay in zenith direction. The line-of-sight delay model can be supplied by orthogonal gradients, in this case, the tropospheric path delay ΔL signifies the symmetric delay $\Delta L_0(e)$, where gradients (Chen & Herring, 1997) account for variations in the North (G_n) and East (G_e) directions:

$$\Delta L = \Delta L_0(e) + \frac{1}{\sin(e)\tan(e) + C} \cdot [G_n\cos(a) + G_e\sin(a)], \qquad (3.10)$$

where constant value C is 0.0032 and a is the azimuth angle. The a priori model for mapping function can be provided by Böhm *et al.* (2006), or, in the other approach, ray-traced delays can be utilized to calculate mapping function, North and East gradients as well as the zenith delay. The ray-traced delays applied in the reductions for this thesis were obtained by (Hofmeister, 2016) for the VLBI analysis.

The technical side of VLBI contains very small but measurable deformity, which modifies the path delay in addition to tropospheric delay. The daily temperature change induces complex distortions in the structure of the radio-antennas and, as consequence, reference markers of dish experience deformations called thermal antenna deformations (Haas *et al.*, 1999; Nothnagel, 2009; Skurikhina, 2001) and axis offsets (Krásná *et al.*, 2014). These particular VLBI related corrections are small but might be correlated with atmospheric tides due to the same origin of solar heating.

3.2.3 A priori Earth Orientation Parameter model

The final part of reductions discussed here concerns the position and spin rate of the Earth rotation axis or the CIP, respectively (Petit & Luzum, 2010). The largest signals in polar motion are the Chandler wobble mainly generated by atmosphere-ocean contribution and forced variations related to the irregular processes in the atmosphere and ocean such as ocean bottom pressure variations, ocean currents, atmospheric pressure and winds. The largest regular harmonic variations of the spin rate are demonstrated on inter-seasonal and long-terms periodicities by solid

Earth tides (Yoder *et al.*, 1981) and the somewhat less powerful by ocean tides. The short-period variations comprise mainly ocean tides and significantly smaller variations of atmospheric tides in polar motion and spin rate. The Earth's spin rate is affected by additional irregularities related to climate variability including El Niño and La Niña events in equatorial areas and the Southern Hemisphere (Kolaczek *et al.*, 2003).

Currently any types of irregularities of the Earth's rotation (Eubanks, 2013), in general, are not considered in a priori tidal models. And, periodic effects such as the tidal variations for the solid Earth and the oceans are taken into account in the reductions. Usually, models for zonal tides applied for the spin rate are stated separately from the product of the Combination Center (Petit & Luzum, 2010). According to the IAU 2000 resolution, forced motion due to torques acting on the non-axisymmetric Earth appears in the celestial reference frame with periods of less than two days. These oscillations are referred to as libration and accounted for as variations of ERP in the ITRS (Petit & Luzum, 2010) additionally. All remained variations in Earth Rotation (except ocean signals in diurnal and semidiurnal bands) are supposed to be included in the EOP time series, which are provided by the IERS Earth Orientation Center and divided into four types of combined (C) data (Gambis *et al.*, 2001): C01 is a long-term solution of 0.05 year sampling, C02 and C03 are intermediate solutions given at 5 or 1 day-intervals correspondingly, and, the last, operational smoothed C04 series with daily sampling are used in routine VLBI analysis. These C04 time series are updated twice per week and reported values with a delay of 30 days from the release date. For rapid services the a priori EOP data with less latency is required, thus Bulletin A widely known as 'finals' (Luzum & Gambis, 2014) was established to supply this shortage. Bulletin A contains the EOP values, which are partially predicted and based on geodetic techniques. Bulletin A is different from Bulletin B in that the celestial pole offsets and dUT1 are obtained from a combination and not only from VLBI. Generally, both bulletins are a product of the geodetic techniques combination (Gambis & Luzum, 2011) using LLR, SLR, VLBI, GNSS and optical methods until 1970. The combination of geodetic techniques informs the full set of EOP, for which several series were already released. One of the earliest is C04 05 time series compatible with ITRF2005, the next one is C04 08 time series consistent with ITRF2008 and International Celestial Reference Frame (ICRF)2, and the last released time series are C04 14 (Bizouard *et al.*, 2017, preliminary draft on 9/Jan/2017) adapted for ITRF2014 and ICRF2. In the current analysis the last two were used with the appropriate ITRF and ICRF2 realizations in reductions.

Finally, ocean tides are reported by means of amplitudes for 71 frequencies in the diurnal and semidiurnal bands (Petit & Luzum, 2010). As already implied smaller effects in these bands are the atmospheric tides with frequencies of 1 cpd and 2 cpd. These signals are not included in the IERS Conventions for polar motion as well as for dUT1. As it was mentioned above, the complicated mixture of the ocean and atmospheric tides is required to be assigned properly. Namely, at the S_1 frequency the small gravitational tide is about 1μas in polar motion and 0.1μs in dUT1, which amplitudes are given in the set of 71 tidal constituents. Large variations are observed for the radiational part (Girdiuk *et al.*, 2016b), and their amplitudes can be obtained in a separate approach by utilizing atmospheric excitation functions based on the pressure and wind field dis-

tribution as provided by weather models (for instance, ECMWF). The least studied part is the hydrodynamic ocean response to the atmospheric forcing. Accounts for this signal can be found in the most recent ocean models FES2012 and FES2014. The other frequency of atmospheric tides S_2 represents a different magnitude ratio of these excitation sources. In particular, the S_2 tide is the principal semidiurnal solar tide in the TGP and possesses considerable amplitude of about 130 µas in the retrograde band. The radiational part of S_2 can be evaluated in analysis of atmospheric excitation functions only as separate contribution, but such estimate at the S_2 frequency is largely suppressed by the standard sample rate of weather models every 6 hours (Arbic, 2005). Some recent ocean models, like FES2012 and FES2014, include the cumulative effect of the ocean tide and the response to the atmospheric forcing at the S_2 frequency simultaneously.

Chapter 4

Analysis of VLBI observations

This chapter contains the VLBI data set report and its processing. The VLBI analysis is revised with focus on a calculation of the high-frequency ERP time series and station position variations. In particular, the a priori geophysical models are discussed in the context of this analysis to disclose any dependencies.

Geodetic VLBI observations are available in open access and various processing packages were developed to satisfy requirements and realize reductions discussed in the previous Chapter. These packages can be found at http://ivscc.gsfc.nasa.gov/ with links to the persons who are currently responsible for this software. Since this study has emerged at the Vienna University of Technology (TU Wien), the Vienna VLBI and Satellite Software (VieVS) is applied for the VLBI data processing (Böhm *et al.*, 2012, a). The Least Squares Adjustment (LSA) is a common method in VLBI analysis and implemented in VieVS as well as its modifications in other softwares. The first VLBI sessions were sparse in the beginning and analyzed separately in a single session solution. The second approach, a global solution, became available when the frequency of sessions had increased up to at least two sessions per week and a considerable number of observations had been assembled over several years.

First and foremost, this chapter employs the single session solution because time series of the parameter estimates are accessed along with their statistical assessment. The single session solution, thus, can reveal potential inadequacy in parameters or systematic effects. The global solution is an extension to the single session solution. A precise parameter estimation over the whole time span characterizes the global solution, where imperfections of particular data are averaged. For instance, Böhm (2012) demonstrated the determination of the high-frequency ERP tide terms from a global solution. In this thesis the evaluation of an empirical high-frequency ERP model for the same tide terms is provided in the single session solution without enlargement of accuracy.

4.1   Data set

The first VLBI observations were made in 1979 and described in the first technical reports by Vandenberg (1999a); however, a community was established 20 years later (Vandenberg, 1999b). The leading role in the initial community effort belonged to a joint activity of the U.S. Naval Observatory (USNO) and GSFC, for VLBI provided within National Earth Orientation Service (NEOS) by launching programs NEOS-A. Following this activity the first Acting Analysis Coordinator (Eubanks *et al.*, 1999) was appointed to organize routine data processing flow in Analysis Centers and present this work together in Analysis reports.

The first observations were scattered in the early 80s, and on a routine basis they were established with sessions starting from 21 December 1983 every 5 days and afterwards every week from May 1993. First continuous VLBI observations were started in 1994 by the first campaign CONT94. After this successful campaign in 1996, Continuous Observations of the Rotation of the Earth (CORE, MacMillan *et al.*, 1999) was performed along with Continuous VLBI 1996 (CONT96). Next similar campaigns (CONT) are run currently every 3 years (Behrend, 2013). And under the CORE program sessions were produced weekly (CORE-3) and monthly (CORE-1, on Monday). Contemporary regular observations twice per week – the rapid turnaround R1 and R4 (on Monday and on Thursday, correspondingly) – were launched in 1997. These VLBI campaigns were arranged for EOP determination. Moreover, a great number of specially designed programs, for instance, 24 hour duration Research and Development (RD) and Research and Development with the VLBA (RDV) were begun in 1988-1989 and 1997 correspondingly, where Very Long Baseline Array (VLBA) network consists of up 10 geodetic stations. RDV sessions were shown recently suitable for EOP analysis (Gordon, 2017) and some of RD sessions are found to provide reasonable EOP time series in this thesis.

The modern VLBI sessions are provided in the form of 24 hour continuous observations collected from networks including at least 3 antennas maintained by IVS. The intensive sessions for daily UT1 measurements and some of experimental sessions involve two stations; these sessions are not suitable for global parameter estimations and, as a consequence, excluded from the data set in this thesis. In the other kinds of campaigns, for instance, already mentioned RD are designed on wide networks and observe over 24 hours. Since this configuration matches to accepted assumption on network size, RD were included in data set. Overall, the continuous monitoring of global parameters requires at least 24 hours VLBI observations duration per session and their considerable number as well as the rigorous selection of the data set.

As follows, observational data are assembled from routine 24 hour VLBI sessions in several steps: firstly, all available sessions in period from 1989.10 to 2014.01 were processed, then in a subsequence of numerous iterations a part of these data was excluded and extended on the period from January 1995 until mid-June 2015. The final data set includes mainly the operational R1 and R4 sessions, NEOS-A as well as experimental sessions such as CORE, RD and RDV sessions, continuous VLBI campaigns (CONTs), and some other experiments (Table 4.1), which are similar in characteristics to R1 or R4 sessions. Table 4.1 represents main session types in this

Session type	Description	Number
AP	Asia-Pacific	12
A (AUST)	AuScope (mainly Australian network)	23
	VLBA-only session	5
CORE-1/-3	CORE	47/37
CORE-A/-B/-C	CORE	71/46/5
COH	CORE Ohiggins sessions	9
CONT96/CONTM	CONT/continuous	3/5
CONT02/05/08	CONT	12/27/13
CRD/CRF	CRF deep-south/CRF	29/6
E3/T2	S2 EOP sessions for IVS/IVS TRF sessions	10/56
EUR	Europe	79
GG	Golden Global TRF	5
GT	Global TRF	3
IS	IRIS-S	43
NA	NEOS-A	282
NAEX/NAP/NAX	NAVEX (Navy Experiments)/NAPS/part of CONT94	8/3/5
OH	Ohiggins sessions	56
R1	rapid turnaround	572
R4	rapid turnaround	537
RD	Research and Development, includes CONT94	93
RDV	Research and Development with the VLBA	86
SAT/STRF	South Atlantic TRF, Southern hemisphere TRF	1/17
	Trans-Pacific/Trans-Atlantic	2/1
WAP/WP	Western US plate stability/Western Pacific	10/2

Table 4.1: The main session types used in the analysis are represented. For each session type the description is given as it can be found in the IVS data base and the number of sessions contained in the analyzed data set is shown in the last column.

analysis described in more details at the IVS data base. Some sessions designed for TRF or CRF determination are also suitable for this analysis at the first selection step, which implies that some amount of data from these sessions (Table 4.1) might have been excluded further.

4.2 A common concept of LSA applied in VLBI analysis

As mentioned, this thesis utilizes VieVS (Böhm *et al.*, 2012, a) where the LSA method is applied to a classical Gauss-Markov model. As usual, an overdetermined system $A\hat{x} = \hat{b}$ has undergone the LSA, which minimizes the functional S:

$$S = \min(\hat{r}^{\mathrm{T}} P \hat{r}), \tag{4.1}$$

where the parametrization matrix A consists of n unknown coefficients for m equations with respect to number of observations. The observations $\hat{b}$ with known weights $w_i > 0$ compose a

diagonal matrix P. The solutions can be found for the system where $m > n$ in the form of the best fit residuals $\hat{r} = A\hat{x} - \hat{b}$, and these observations are supposed to be uncorrelated. The normal equation system provides a unique solution:

$$
\begin{aligned}
N &= A^\mathrm{T}PA, & Q &= N^{-1}, \\
N\hat{x} &= A^\mathrm{T}P\hat{b} \Rightarrow & \hat{x} &= QA^\mathrm{T}P\hat{b}.
\end{aligned}
\tag{4.2}
$$

A covariance matrix $M_{\hat{x}}$ should characterize observations, but at practice the co-factor matrix Q and weight matrix P are used instead:

$$
M_{\hat{x}} = \chi^2 Q,
\tag{4.3}
$$

and the diagonal matrix of weights P is formulated for a priori variance σ^2 as $P = \sigma^2 I$ (I is identity matrix), which is approximated by a posteriori variance of unit weight χ^2 in order to minimize the functional S:

$$
\chi^2 = \frac{\hat{r}^\mathrm{T}P\hat{r}}{m-n},
\tag{4.4}
$$

where $m - n$ is the degree of freedom. When the functional S achieves its minimum, the χ^2 value equals 1, but this situation is impractical and the values χ^2 obtained in the processing of regular VLBI sessions are typically within the range $[1.2-1.6]$. In order to attain this level a couple of additional prerequisites (e.g. a datum definition) are applied for special cases, for instance, when observations are unevenly distributed and overloaded by noises or outliers. These solutions are realized by the set of reliable stations and sources, which have been chosen to provide the reference.

The matrix A of unknown coefficients is composed by derivatives of introduced parameters. In the regular parametrization (Table 4.2) instrumental parameters which include clock polynomials, and atmospheric parameters (zenith wet delay and tropospheric gradients in north and east directions) are estimated along with EOP, station and source coordinates in routine VLBI analysis. Among them the short estimation intervals are adjusted for the frequently changed atmospheric parameters and clocks, whereas the other parameters can be resolved once per session (Table 4.2). The earliest VLBI observations are rather sparsely distributed within an hour as well as hour to hour, and thus the number of observations per interval can be insufficient. By these reasons, pseudo-observations, which are an extension in the character of "real" observations, are

	Clock's parameters	Zenith wet delays	Tropospheric gradients	EOP	TRF CRF
interval	1 h	30 min	6 h	1 d	1 d
relative constrains	1.3 cm	1 cm	0.05 cm	10^{-4} mas in PM 10^{-4} ms in dUT1	10 cm for TRF 10^{-4} mas for CRF
absolute constrains	-	-	0.1 cm	- -	- 10^{-4} mas for CRF

Table 4.2: The regular parametrization of the single session solution includes parameters listed at the caption along with their estimation intervals and relative constraints, which are normally used. The absolute constraints can be implemented on demand in VieVS for all parameters with corresponding reasonable values.

implemented to balance this inhomogeneous distribution of observations:

$$A\hat{x} = \hat{b} + \hat{r} \Longleftrightarrow \begin{bmatrix} A_{ro} \\ A_{po} \end{bmatrix} \hat{x} = \begin{bmatrix} \hat{b}_{ro} \\ \hat{b}_{po} \end{bmatrix} + \begin{bmatrix} \hat{r}_{ro} \\ \hat{r}_{po} \end{bmatrix}, \quad P = \begin{bmatrix} P_{ro} & 0 \\ 0 & P_{po} \end{bmatrix} \tag{4.5}$$

where $\hat{b}_{ro}$ is the vector of observed delays. The parametrization of A_{po} applies certain restrictions on the parameters introduced in the matrix A_{ro} of two kinds: relative constraints between adjoining estimates and absolute constraints as a ceiling values listed in the Table 4.2. Numerical values of constraints are chosen arbitrarily to present loose and tight restrictions. For most of the parameters relative constraints are applied and the rigorous approach by absolute constraints is avoided in this thesis. The vector of pseudo-observations $\hat{b}_{po}$ sets as a rule to zero to enable introducing these constraints in the matrix A_{po}.

With a different intention, the constraints are applied to establish the origin of the reference frames or datum. The terrestrial and celestial reference frames are evaluated separately by means of station and source coordinates estimates in the LSA which can produce a number of origins. The datum, however, requires to be defined unequivocally, so that station and source coordinates need to be restricted additionally in the regular parametrization. Namely, the six Helmert transformation parameters (except scale, which is currently optional in routine VLBI analysis) are necessary and sufficient in the three-dimensional space to provide undisturbed transformation from one datum to another. One datum is defined by a priori used TRF and another is a new adjusted reference frame. In practice, Helmert transformations are introduced for reliable station positions only and the rest of stations are excluded from the datum.

4.3 Single session solution

The high-frequency ERP and station position parameter estimates are obtained in the single session solutions, for which the concept of Continuous Piece-Wise Linear Offsets (CPWLO) is introduced (Schuh & Böhm, 2013) at selected intervals for each parameter individually. This di-

vision into intervals produces the time series of the estimated parameters. CPWLO can also adjust these intervals in order to minimize correlations among parameters in matrix *A*. To demonstrate this approach the delay model given in equation (3.2) can be simplified in form of:

$$\tau = -\frac{b \cos \varphi}{c}, \tag{4.6}$$

where φ is an angle between direction of source and baseline, so that in the application of the LSA this model is defined for the residuals $\Delta \tau$:

$$\Delta \tau = \frac{\partial \tau}{\partial b} \Delta b + \frac{\partial \tau}{\partial \varphi} \Delta \varphi, \tag{4.7}$$

where the derivatives which compose matrix *A* can be generalized as follows:

$$\frac{\partial \tau}{\partial b} = -\frac{\cos \varphi}{c}, \tag{4.8}$$

$$\frac{\partial \tau}{\partial \varphi} = \frac{b}{c} \sin \varphi. \tag{4.9}$$

These partial derivatives specify two groups (Sovers *et al.*, 1998): geodetic and astronomical parameters. In the routine analysis, the first one is represented by station coordinates and the second one by source positions estimates. The LSA application assumes observations to be independent, but estimates can correlate among each other. Given that angle φ changes entirely in interval $[0° : 360°]$ within 24 hours and corresponding length b of generated baselines takes values in interval $[b_{\min} : b_{\max}]$. The duration of a single session is required to last at least this time, so that the correlation ρ between station and source parameters equals zero:

$$\rho(\frac{\partial \tau}{\partial b}, \frac{\partial \tau}{\partial \varphi}) = \frac{Cov(\frac{\partial \tau}{\partial b}, \frac{\partial \tau}{\partial \varphi})}{\sqrt{Var(\frac{\partial \tau}{\partial b}) \, Var(\frac{\partial \tau}{\partial \varphi})}}, \tag{4.10}$$

where Var is a variance, so that $Var(x) = Cov(x, x)$ for any random variable x, and Cov is a covariance

$$Cov(\frac{\partial \tau}{\partial b}, \frac{\partial \tau}{\partial \varphi}) = \int_{b_{\min}}^{b_{\max}} \int_{0°}^{360°} \frac{\partial \tau}{\partial b} \cdot \frac{\partial \tau}{\partial \varphi} d\varphi db = -\int_{b_{\min}}^{b_{\max}} \int_{0°}^{360°} \frac{b}{c} \cdot \cos \varphi \sin \varphi d\varphi db = 0. \tag{4.11}$$

Thus, it becomes sufficient to evaluate random variables of station coordinates and source

positions once per session to ensure their independence. In the processing of regular VLBI observations the correlation matrix $Corr$, which shows dependencies between parameters, can be calculated based on the co-factor matrix Q obtained in the applied LSA. The matrix Q is modified by the factor χ^2, thus the matrix Q takes properties of the covariance matrix $M_{\hat{x}}$ and the elements of correlation matrix $Corr$ can be expressed as follows

$$Corr = Q/\sqrt{diag(Q) \cdot diag(Q)^{\mathrm{T}}}, \qquad (4.12)$$

where $diag(Q)$ denotes a vector of diagonal elements of the matrix Q.

The analysis of correlations can approve the appropriate adjustment of already chosen intervals and improve the accuracy of parameters. Even in the case of the best choice of intervals, all correlations can not be minimized entirely. For example, results for a routine VLBI session 09DEC16XA_N004 shown in Figure 4.1 exemplify a typical case of a standard division of estimates into intervals. This symmetric matrix demonstrates that the largest dependencies can be found on the diagonal elements. The strongest correlations are produced by clock polynomials (the part assigned as clocks on the plot) and among sources, where dependence on clocks are expected due to a complicated dependence of clocks and observed frequencies (Sovers *et al.*, 1998). At the same time, correlations of clocks from station to station often can be considered as insignificant, indicating a high level of synchronization. Concerning significant correlations among some sources the reason may arise from an insufficient distribution during observing times. The remarkable part is that sources have a complete independence with the rest of parameters. This fact supports the ICRF realization.

More important, Figure 4.1 illustrates internal dependencies of atmospheric parameters due to the fact that their partial derivatives include a common dependence on an elevation angle e of the observing source above the horizon for zenith wet delay ZWD (Böhm *et al.*, 2006) and north NGR and east EGR gradients (Chen & Herring, 1997) :

$$ZWD \propto \frac{1}{\sin e}, \qquad (4.13)$$

$$NGR(EGR) \propto \frac{\cot e}{\sin e}. \qquad (4.14)$$

For the concept given by equation (4.10), different intervals were also confirmed practically (Sovers *et al.*, 1998). As the result, the hourly and half-hourly intervals for the zenith wet delay are widely used in routine analysis as well as 6-hour intervals for the gradients evaluation. Atmospheric parameters are correlated also with station heights (Sovers *et al.*, 1998) because of the same dependents on the elevation angle e:
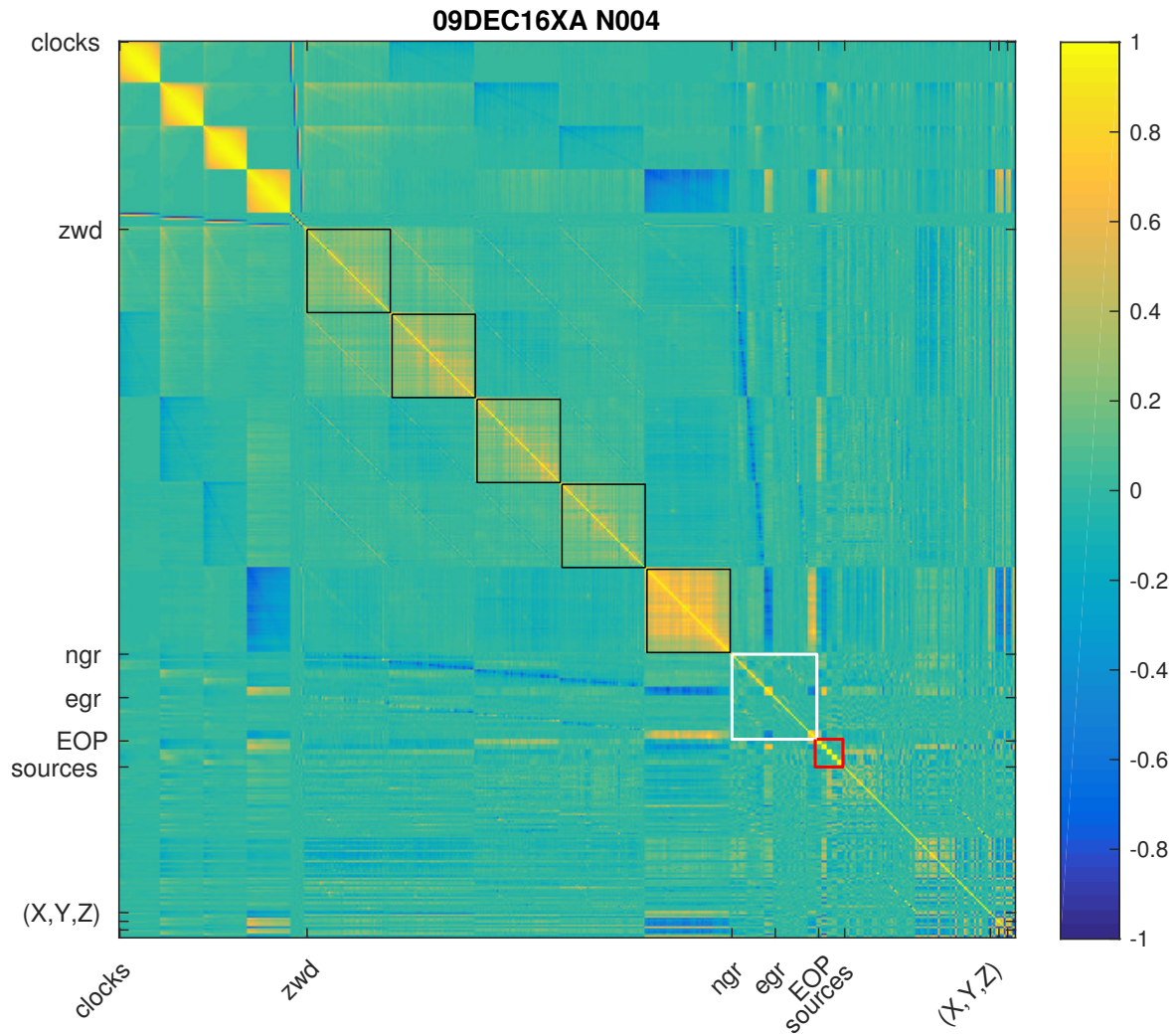
Figure 4.1: The symmetric correlation matrix of single session 09DEC16XA_N004 illustrates the regular single session parametrization. The diagonal elements are dependent ($\rho = 1$). This matrix is composed of parameters listed in the Table 4.2 and abbreviated as clocks (clock's parameters), zwd (zenith wet delay), ngr and egr (tropospheric gradients in North and East directions correspondingly), EOP, sources and (X,Y,Z) for CRF and TRF. The black blocks separate the zenith wet delay estimates for each station (5-station network). The white block highlights the tropospheric gradients in North and East directions. The red block underlines EOP estimates.

$$\frac{\partial \tau}{\partial R} \propto -\sin e, \tag{4.15}$$

where R is a displacement in radial direction related to a rectangular coordinate system with its origin in geocenter as defined by equation (3.7). In Figure 4.1 estimates are obtained in a rectangular coordinate system, so that dependence in radial direction propagates mostly into X component of the station position vector. Besides, some correlations may appear in Y and Z components.
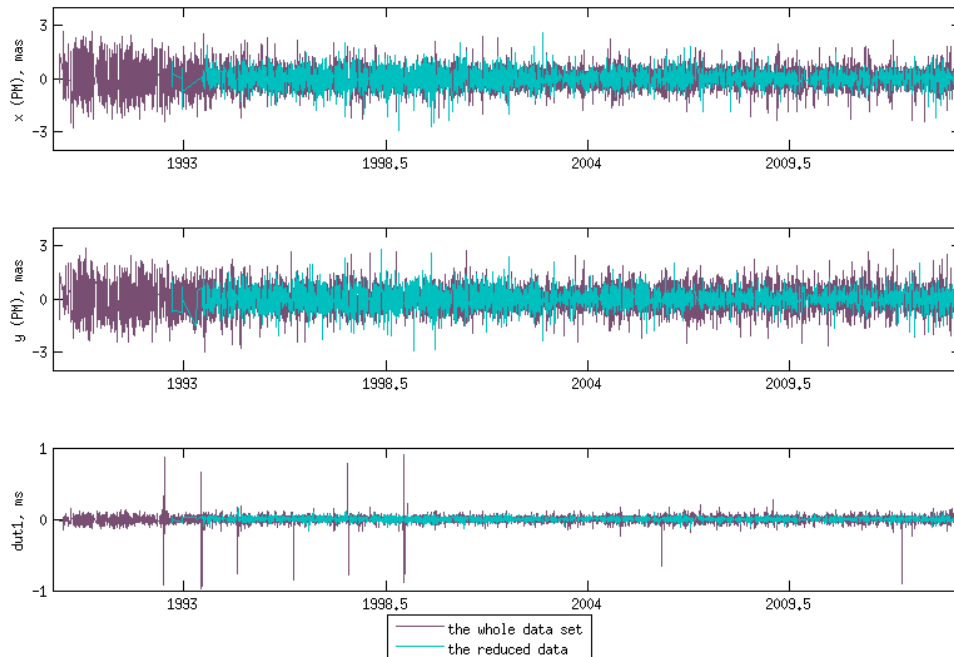
Figure 4.2: The time series are obtained on the basis of network geometry selection (cyan) and without (violet color). The panels demonstrate time series of *x* and *y* component of polar motion (upper and middle) and dUT1 (lower).

In practice, due to insufficient time and spatial resolution among observations, outliers appear for time series of parameters estimated in the LSA. To ensure reliability of the obtained data, the standard deviations (std) can be calculated for each parameter and epoch:

$$std = \chi \cdot \sqrt{diag(Q)}. \tag{4.16}$$

Yet, the analysis of this time series cannot be straightforward because the VLBI sessions are performed on a non-continuous basis. The temporal distribution within a session affected by the CPWLO application since it separates data in intervals.

Arguments concerning data selection

The VLBI method is found to depend on baselines in particular (Moritz & Müller, 1987), i.e., the longer the baselines generated during a session, the better the obtained ERP estimates, which are the aim in the processing revision. In order to specify the limiting range of these baselines, a commonly used factor, which condenses the impact of all baselines and all directions, is the volume of the VLBI network (Dermanis & Mueller, 1978). Besides some technical factors, for instance, station equipment issues, the network volume is the global characteristic for the network description as entire system. Regional networks as well as sub-networks during session defined usually by shorter baselines can be distinguished from the global networks by means of

this parameter. Thus, the network geometry is applied within an interval of an estimation (1 hour for ERP) to explore the reason for large uncertainties in parameter estimates at particular epochs. It approves that a number of outliers in the time series of the parameter estimates can occur due to the existence of small sub-networks per hour, when the designed network for a whole session exhibits a global coverage.

The data set was revised on the basis of the network geometry following to Dermanis & Mueller (1978). Both the network volume computed from tetrahedrons (Malkin, 2009) as well as the east-west and the north-south orientation of baselines were employed as selection criteria. Different subjectively chosen thresholds were applied on this network measures to subset the high-frequency ERP time series into a higher-quality data set. Finally, the network geometry restriction removes up to 50 % of the original time series. The vast majority of these data are sessions performed in different kind of test mode (NAEX, but most of them are not included in Table 4.1 because these sessions do not belong to any of listed types) or using regional networks (EUR, WAP). The rest of outliers were found among all other session types as result of small sub-networks generated within globally designed sessions. The overall feasibility of selection criteria is verified by the fact that the reduced data are unencumbered by gross statistical outliers in comparison with the complete data set (Figure 4.2). After eliminating these outliers based on the network geometry, some smaller features can be still retained in the reduced data set (Figure 4.2). Fortunately, these questionable estimates can be down-weighted individually by means of standard deviations obtained in the LSA of single session solution.

4.3.1 Earth Rotation Parameters time series

The short-period atmospheric effects in Earth rotation occur at similar frequencies as influences from ocean tides, so the first prerequisite is to employ a reliable empirical ocean model. Most of the models include the tidal terms that account for the gravitational forcing only, for instance, the high-frequency Conventional model. For S_1, the TGP includes two spectral lines close to 1 cpd, while the radiational part remains unaccounted for. Since the ocean impact is known well at the predefined frequencies and a number of ocean models are available, ocean tides can be reduced in the processing. The atmospheric tides, thus, will be seen as addition systematic deviations at the frequency of S_1 (S_2 atmospheric part is omitted, see Chapter 2).

Evaluation of the empirical high-frequency tide terms requires two-step single session solution. It is necessary especially for proper nutation reductions and FCN effect, which is not a part of the IAU 2006/2000A model (Petit & Luzum, 2010). In fact, nutation in the terrestrial reference frame is the retrograde diurnal polar motion, but with regard to the IERS Conventions this motion is considered in the celestial reference frame as the long-term CIP motion. The estimation of the high-frequency polar motion along with nutation at hourly intervals, thus, provokes correlations. Since the subject of interest is the high-frequency ERP time series, nutation is fixed to the a priori values. As follows at the first processing step, the full set of EOP is estimated daily as in routine processing. In this case, a priori model is used for polar motion and dUT1 only and for celestial

09DEC16XA N004
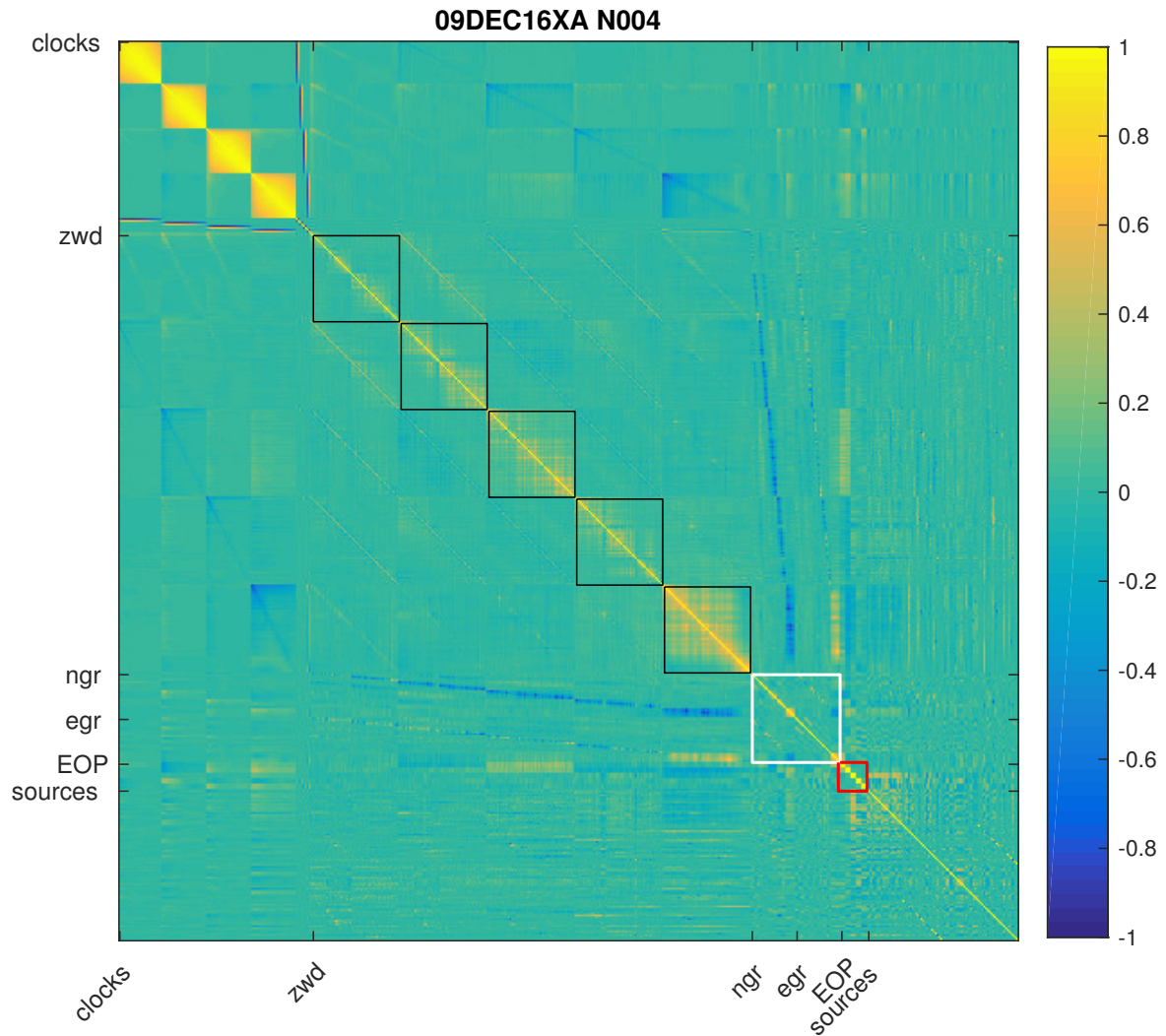
Figure 4.3: Correlation matrix is shown as in Figure 4.1 but station coordinates are fixed to the a priori model.

pole offsets (dX, dY) the model (Mathews *et al.*, 2002) is discarded to produce their total values. At the second step, these obtained daily EOP time series are implemented as the a priori model (instead of C04 08 or C04 14 time series), so all unmodeled effects are assumed to be included.

In the single session solution the daily EOP are estimated together with other parameters, which are the same as for a routine processing (Table 4.2). At the second step the subset of the hourly ERP is introduced in the same parametrization matrix instead of daily EOPs. Because other parameter uncertainties propagate to EOPs or ERPs seen, e.g., in the correlation matrix in Figure 4.1, the standard parametrization is revised in case of the two-step-processing. The matrices in Figures 4.1, 4.3, 4.4 show parameter dependencies of the first step in this processing to exemplify common picture of correlations in both solution steps. Black, white and red blocks separate the zenith wet delay, tropospheric gradients in North and East directions and EOP estimates accordingly. Next approaches are expected to decrease correlations in those blocks.
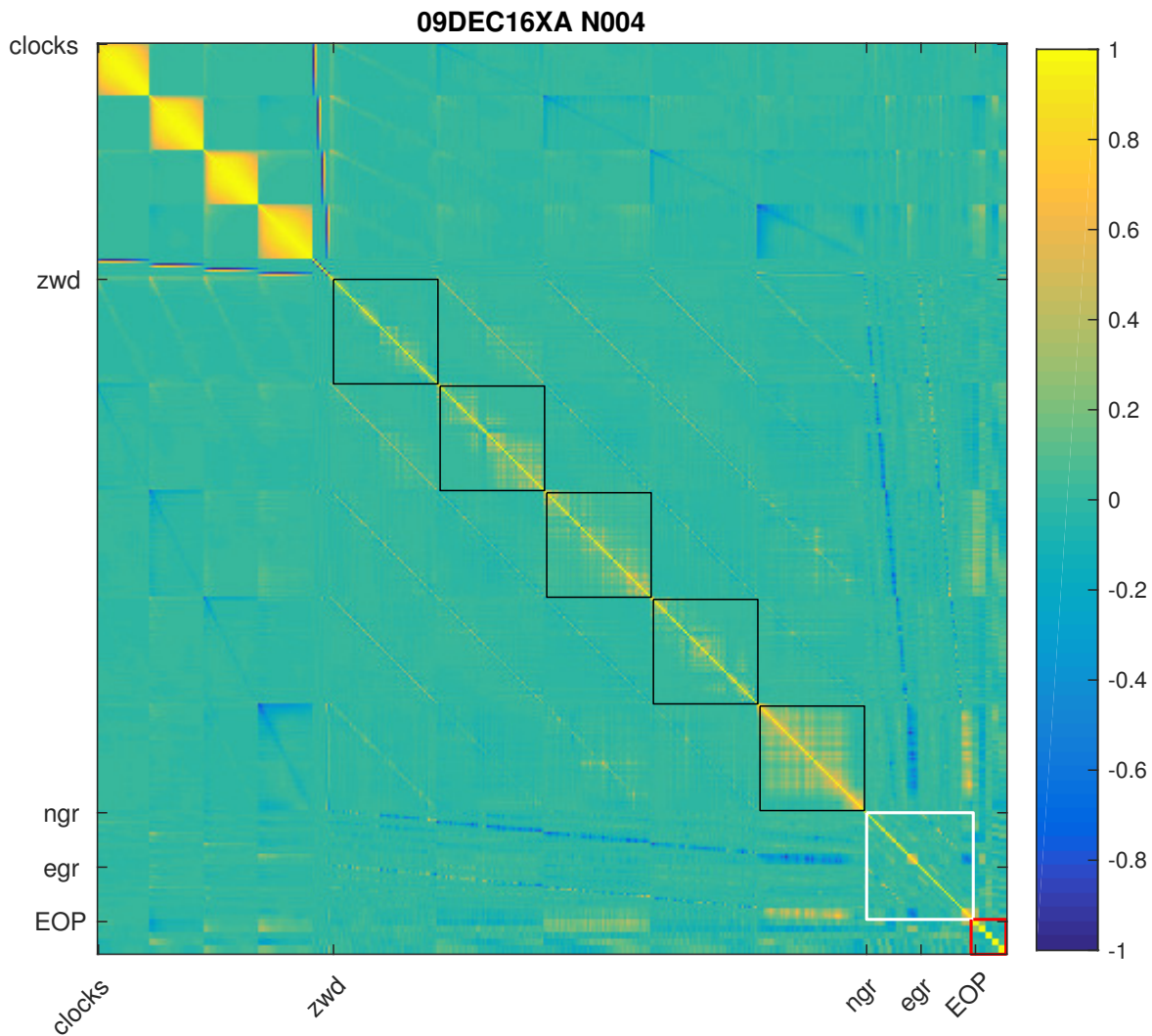
Figure 4.4: Correlation matrix has source fixed relative to Figure 4.3.

A first possible reconsideration is to change estimation intervals governed by equation (4.10). Because a necessary number of observations is provided by the modern sessions (since mid of 90s), which compose the analyzed data set, the ZWD at the 30 minutes estimation interval (Figure 4.1) can be resolved efficiently (without outliers). This analysis follows the regular parametrization (Table 4.2) and already uses 30 min estimation interval, however sometimes the 60 minutes estimation interval for the ZWD can be accepted. Usually, it is required for the earlier sessions, in which the number of observations per half an hour or even per hour can be insufficient.

In a different approach, some parameter estimates can be fixed. Owing to the known relation with the ZWD (equation 4.13) fixing of station coordinates to the a priori model given by ITRF can be found as a reasonable choice. This approach demonstrates smaller correlations of the troposphere with other parameters in Figure 4.3 (cf. black blocks formed between zwd and ngr, and less visible in white block between ngr an egr and red block for EOP).

Similar to the station positions this approach is used to disregard by source estimates. Corre-

sponding parametrization was shown sufficient (Girdiuk *et al.*, 2016b) for deriving an empirical model of the high-frequency ERP tide terms. In other words, the presented solution can produce a better high-frequency time series with realistic statistics given by the standard deviations in the LSA of the single session solution. These standard deviations are expected to down-weight remaining deficiencies in the reduced data set (Figure 4.2). Ultimately, correlations between parameter estimates (Figure 4.4) can be considered already insignificant, thus this parametrization in Figure 4.4 is finalized. This solution infers that reductions for the terrestrial and celestial reference frame are reliable and any ambiguities introduced by mismodeling of the reference frames, which might change the EOP determination, are negligible.

The a priori EOP model is the most important part of the successful determination of accurate EOP and ERP time series. The widely used a priori IERS C04 08 EOP model is discussed in details below. In particular, an affinity of celestial pole offsets given in IERS C04 08 Conventional model and the EOP time series evaluated at the first step of the processing is analyzed. Additionally, the high-frequency ERP time series, which are estimated at the second step, are compared with results from GNSS analysis.

The a priori EOP and ERP time series

A priori IERS C04 08 time series can be introduced in the reductions for the EOP as well as recently released IERS C04 14. Here, a priori IERS C04 08 time series and the EOP time series obtained on their basis (at the first processing step) are considered (Figure 4.5). An analogous treatment using a priori IERS C04 14 time series shows similar results.

The model by Mathews *et al.* (2002) provides an account for nutation and precession, however for determining sub-daily Earth rotation variations the recommendation is to estimate celestial pole offsets within the same solution for the particular geodetic technique. As follows, the total celestial pole offsets dX and dY are evaluated at the first step (Figure 4.5), where the general nutation model (Mathews *et al.*, 2002) is excluded from reductions. The obtained time series contain some additional variations which are not part of Mathews *et al.* (2002) model along with possible noises included in VLBI observations. For an intermediate assessment of the obtained results at the first step, the Pearson correlation coefficients for these EOP sets can be calculated as:

$$\rho_{\text{EOP}_0,\text{EOP}} = \frac{Cov(\text{EOP}_0, \text{EOP})}{\sigma_{\text{EOP}_0}\sigma_{\text{EOP}}}, \tag{4.17}$$

where Cov is covariance, σ_{EOP_0} and σ_{EOP} are respective standard deviations of the C04 08 EOP and the obtained EOP time series. These coefficients are calculated individually for each parameter. The celestial pole offsets dependencies $\rho_{dX_0,dX}$ and $\rho_{dY_0,dY}$ are 0.71 and 0.72 correspondingly. At the same time, Figure 4.5 demonstrates remarkable joint variability of estimated and a priori polar motion and dUT1 (ERP). Numerical values $\rho_{\text{ERP}_0,\text{ERP}}$=1 for each of the three
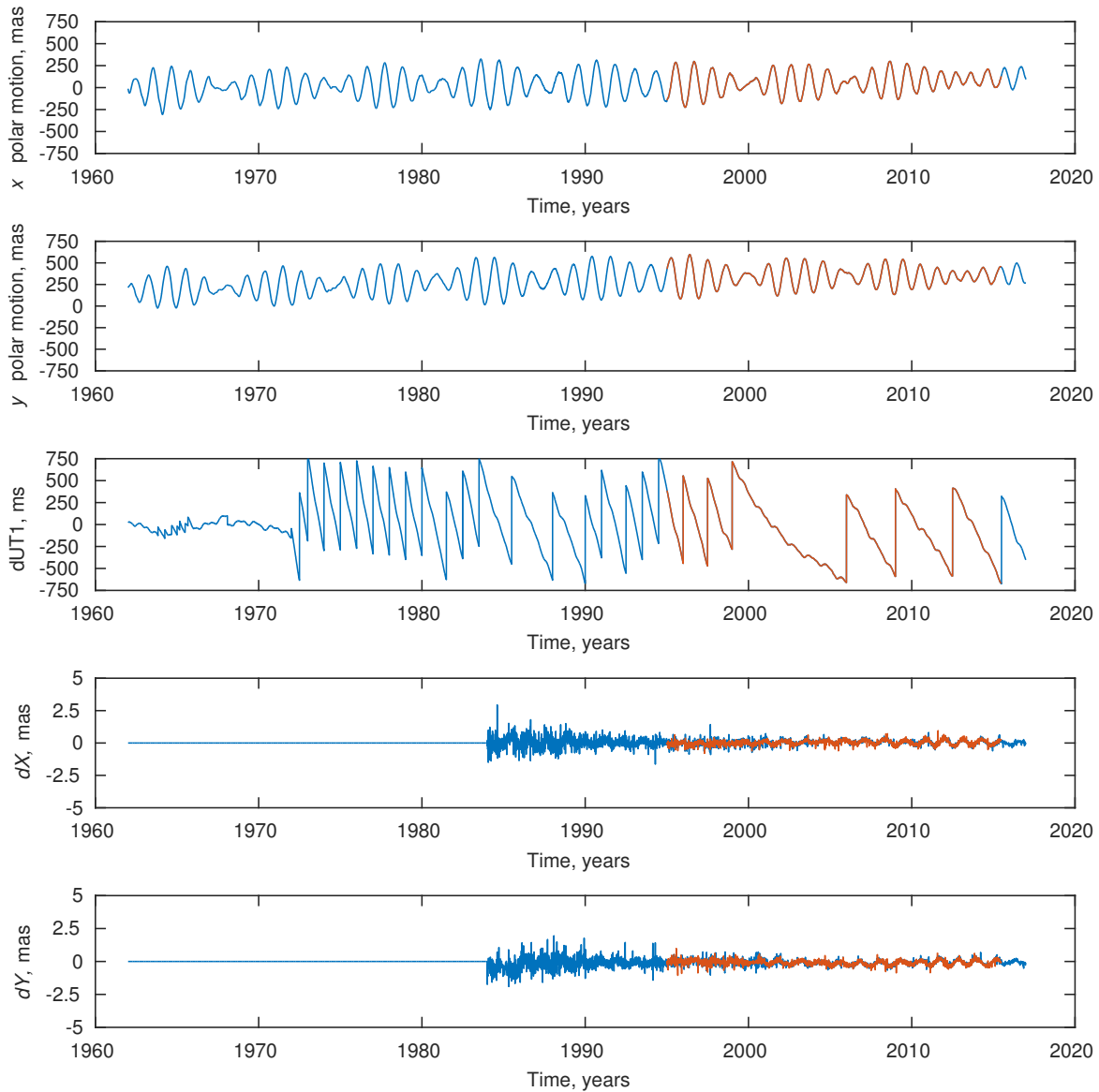
Figure 4.5: A priori IERS C04 08 time series (blue) and obtained time series (red). The full set of EOP (red) was obtained at the first step of the processing with parametrization matrix shown in Figure 4.4. At the panels from top to bottom: x and y polar motion, dUT1, dX and dY celestial pole offsets are plotted.

parameters infer their total dependence, thus these daily ERP time series compose the same geophysical effects.

The EOP time series based on only one technique, for example VLBI, might contain a drift or other systematic effects, which might be seen in a comparison with similar ERP solutions deduced from the analysis of GNSS observations (Figure 4.6). The comparison with Conventional time series (Figure 4.5) might not reveal these problems because this solution is combined by utilization of several geodetic techniques including VLBI.

The analysis of GNSS observations was performed at TU Wien, Department of Geodesy and
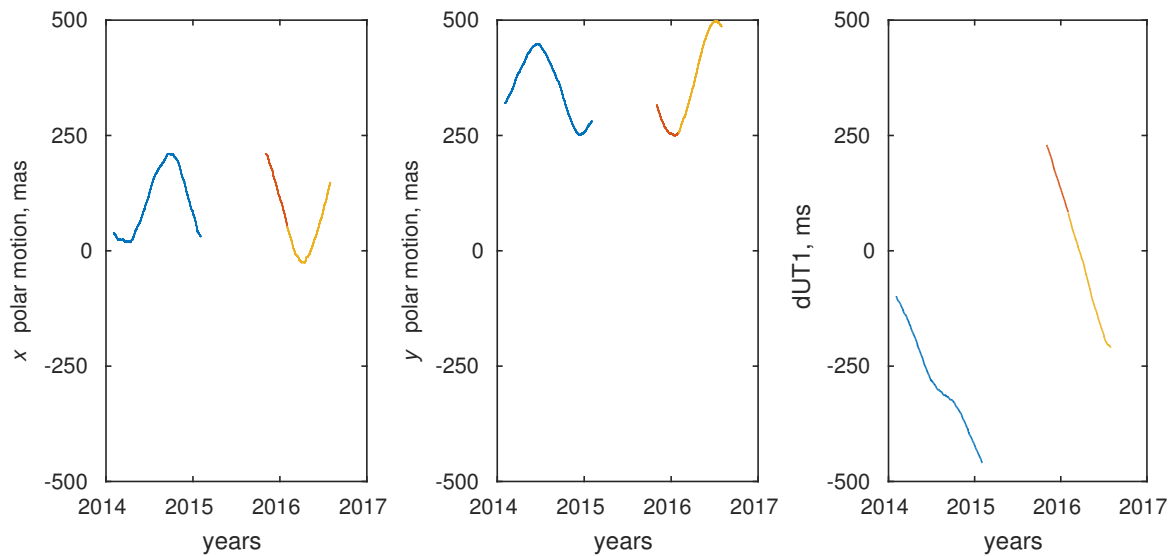
Figure 4.6: Three types of GNSS-based time series. The first, only GPS observations are available in period of January to December marked by blue color; the second set of GPS and GLONASS observations – October to December 2015 marked by red color; the last data from GPS and Galileo – period of January - June 2016 marked by yellow color.

Geoinformation, Advanced Geodesy, by the GNSS group (within the project "GNSS-EOP") in collaboration with Space Research Centre of the Polish Academy of Sciences at Warsaw, Department of Planetary Geodesy, Poland (Weber *et al.*, 2017). In the current comparison, the hourly high-frequency ERP time series obtained for 3 time spans (Figure 4.6) are used. The first time span is based on GPS observations only from January to December 2014. The second set includes observations of two satellite systems, GPS and GLONASS, from October to December 2015. The last set is obtained on the basis of observations of two other observing systems, GPS and Galileo, over the period January – June 2016.

The processing of GNSS data is computationally costly and comprises data from more than a hundred continuously observed stations (174 sites, where no-net-rotation (NNR) condition is applied for 81 stations). In both processing of GNSS or VLBI data to produce the high-frequency ERP time series, the calculation method and the underlying model for EOP (GNSS uses the IGS Final Products provided by IGS) evoke differences. Nutation and precession offsets are obtained similar to the first step of the VLBI processing in this Chapter, however due to the orbit error propagation these parameter estimates are supplied with tightened constraints and not considered further. The a priori EOP model is similar to the Conventional EOP time series, C04 08 or C04 14, and other reductions of GNSS and VLBI are entirely or partially comparable, for example, the ITRF2008, the high-frequency Conventional model and the ocean tidal loading (FES2004) for the station position variations.

The available GNSS observations are continuous within each of the three subsets and contribute with about 15 000 points of hourly parameter estimates. These time series can be compared with the high-frequency ERP time series obtained at the second step in this VLBI analysis.
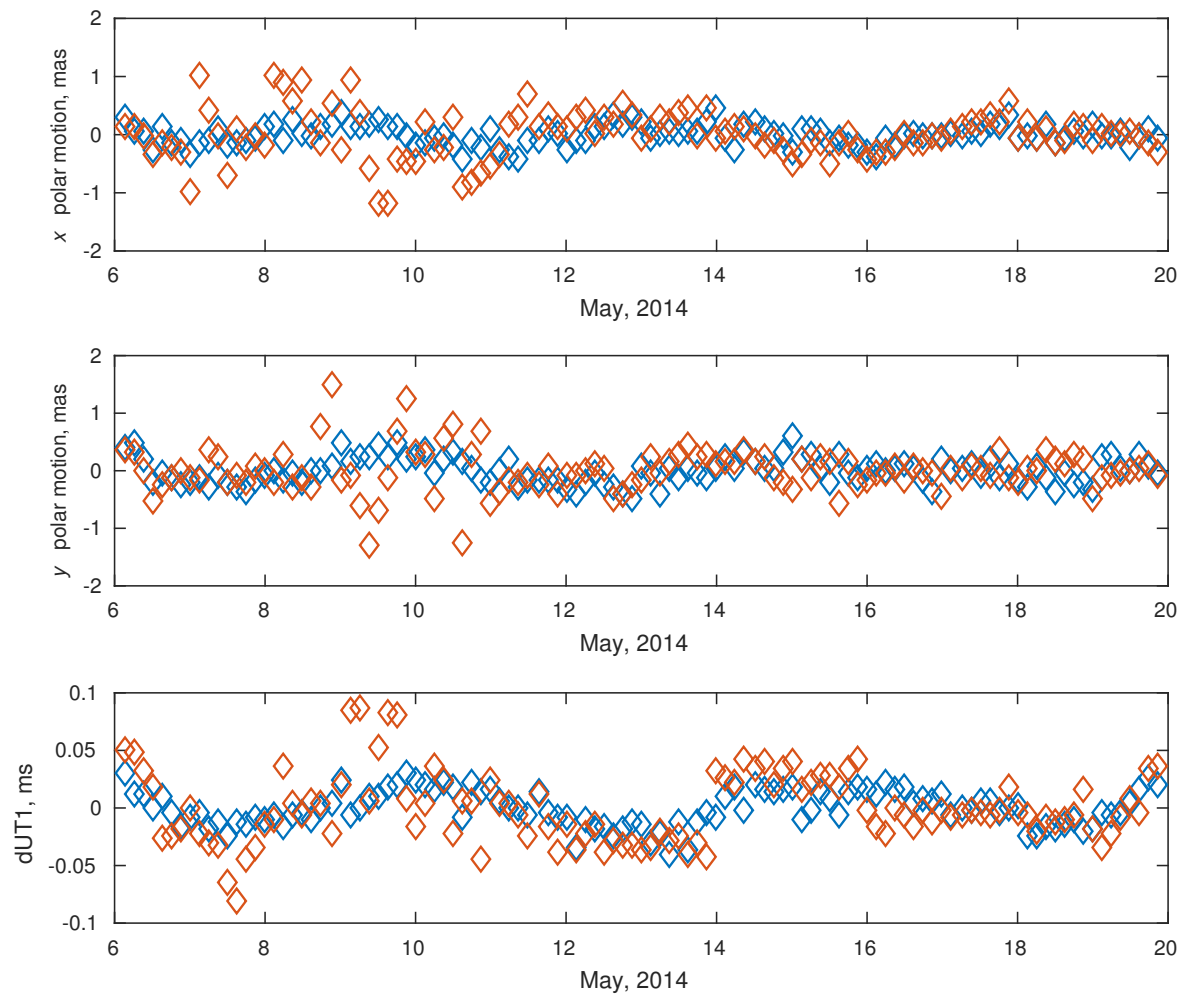
Figure 4.7: GNSS time series (marked red) are plotted along with VLBI time series (marked blue) at the same epochs during the special VLBI campaign CONT14.

Unfortunately, VLBI observations are significantly sparser in time than GNSS, and common epochs are found for only about 800 points of hourly estimates. The same epochs in both time series were identified in 2014 and correlation coefficients were deduced accordingly. Perfect agreement ($\rho = 1$) can be seen for total ERP values (equation (4.17)), but these statistics are mainly influenced by the long-term effects. To illustrate their similarities in more details, the high-frequency variations are considered only. For this purpose, the specially designed campaign CONT14 was chosen from VLBI data set. These observations during CONT14 are a sequence of single sessions provided every day within period of 14 days from 6 May to 20 May, so this is the most dense set of hourly VLBI estimates (Figure 4.7). Over this relatively short time span a curve (polynomial of 5th degree) can be fitted to the estimates to separate the high-frequency variations from long period effects. In this case, a correlation coefficient (ρ) of nearly to zero (0.08) can be found for y component of polar motion, and a somewhat stronger correlation (0.23) for the x component of polar motion. Hence, both components of polar motion can be considered as independent between VLBI and GNSS-based solutions. By contrast, dUT1 shows midmost value (0.53), which

Atmospheric model	Weather model	land-sea mask
TU Wien	Tidal: op. ECMWF DCDA every 3 h Non-tidal: ECMWF 6 h with 1° resolution	determined from ETOPO5 1° resolution
GSFC	NCEP Reanalysis 6 h with 2.5° resolution	from FES99 0.25° resolution

Ocean model	Weather model	Uniform grid
FES2004 FES2012	S_1: from R. Ray, operational (op.) ECMWF 6 h S_1: op. ECMWF DCDA 3 h analysis	$1/8°$ $1/16°$

Table 4.3: Description of the underlying models on which computations of the atmosphere and oceans are based. Atmospheric (TU Wien and GSFC) and ocean (FES2004 and FES2012) models are mainly different due to listed weather models and land-sea mask or uniform grid in case of ocean models.

can be enlarged slightly by lessening CONT14 to subsets, for instance, the second part of campaign data yields 0.6 for dUT1. In general, these high-frequency ERP variations are expected to represent a high level of affinity in disregard to the observing technique. This lack in similarities might be explained by the crucial disadvantage of GPS constellation, which is a deep resonance with the Earth's rotation (Lara *et al.*, 2011). The GPS revolution period is 11 hour 58 minutes and the sidereal period of the Earth's rotation is 23 hour 56 minutes, thus this resonance effects occur twice and once per day. This main weakness introduces an ambiguity in the high-frequency diurnal band, which is problematic for the assessment of S_1, in particular. The main distinctive feature of GNSS results is its ability to provide a continuous high-frequency ERP time series, as follows a sampling (4 hours for the utilized data) is necessary to apply and a harmonic decomposition with the orbit resonant frequencies can induce numerous artefacts in sub-diurnal spectrum as $1/n$ cycle per day for integer value n (Weber *et al.*, 2017).

4.3.2 Study of various geophysical models

The VLBI method utilizes different geophysical models in reductions to take into account the influence of the atmosphere and ocean, which affects EOP estimates and station displacements. In the first part EOP time series were discussed, and the rest of this section deals with station positions corrections calculated based on geophysical models. These changes in station coordinates are called loadings and divided into two parts according to their physical origin: tidal and non-tidal loadings. Amplitudes of these effects are provided by the various services and the computational concept can be seen in Appendix A.

This study is opened with atmospheric loading comparison. Tidal atmospheric loading is known to induce small variations in station coordinates, by this reason a replacement of the background models in reductions applied for the VLBI analysis was not expected to propagate significantly into the estimated parameters. To demonstrate this fact two atmospheric models provided by TU Wien (Wijaya *et al.*, 2013) and GSFC (Petrov & Boy, 2004) were chosen. These models differ mainly in terms of the calculation methods, the weather models and the land-sea
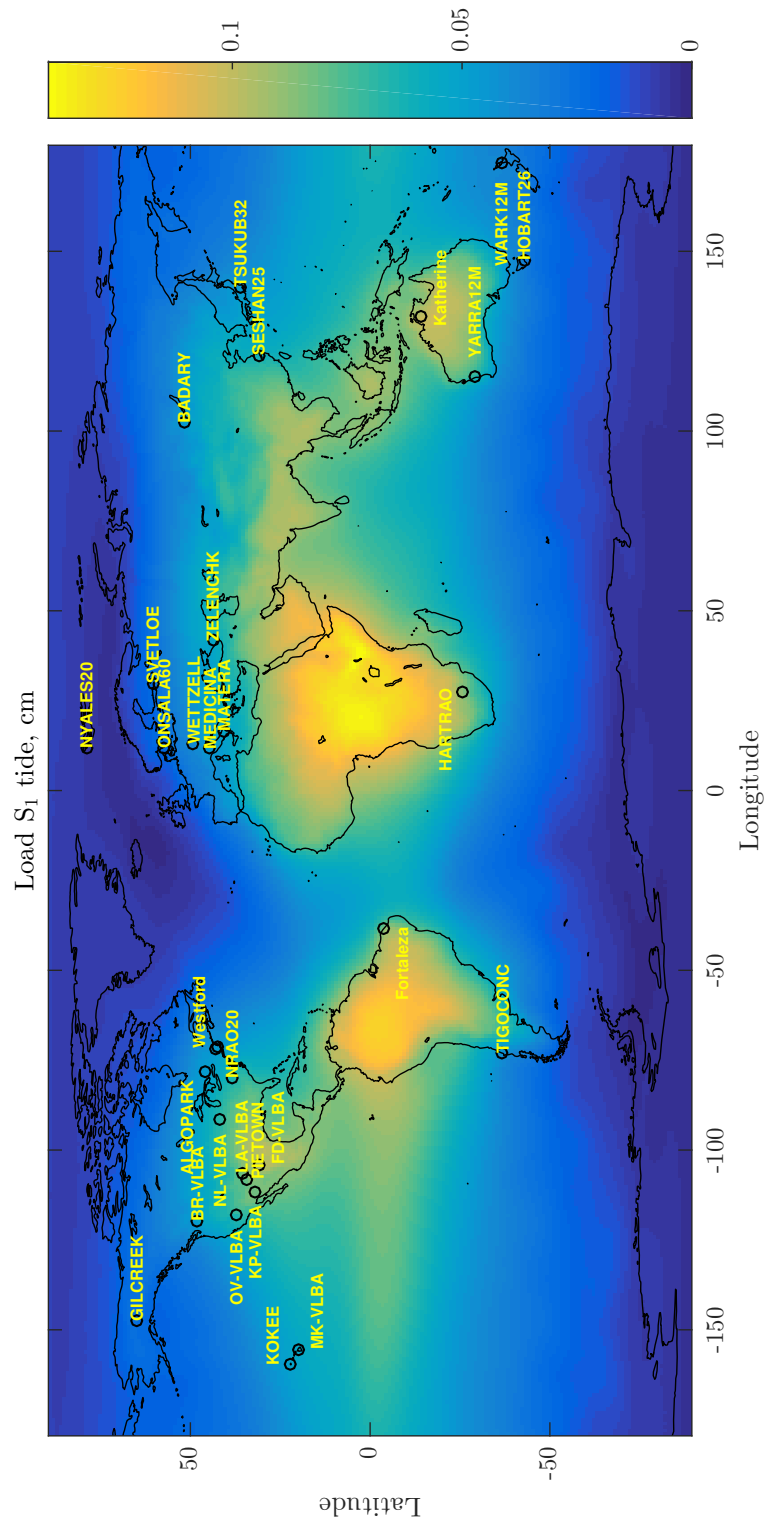
Figure 4.8: Atmospheric tidal loading provided by TU Wien for displacements in radial component given in cm is shown. Frequently observing VLBI stations are plotted as overlay.

masks (Table 4.3). The treatment of the atmospheric pressure field, which is the fundamental quantity in the modeling of the atmospheric loading, is divided into tidal and non-tidal parts (Ponte & Ray, 2002) for both models. The underlying weather models for these computations, however, differ from provider to provider, e.g. ECMWF data is given with shorter time step than data from the U.S. National Centers for Environmental Prediction (NCEP). The ECMWF employs a delay cut-off technique (DCDA) to achieve 3-hourly sampling, which in turn accounts better for the semidiurnal periodicity. Moreover, the ECMWF model is run with finer resolution than the NCEP Reanalysis model. The other distinctive characteristic concerning the atmospheric loading is that the GSFC applies a higher resolution land sea-mask.

The atmospheric tidal loading provided by TU Wien model is shown in Figure 4.8, where the radial component of the load S_1 tide, which carries the majority of tidal loading power, is illustrated. This load S_1 tide exemplifies station displacements, which need to be applied for station positions as reduction. The maximum of this distribution is seen over Central Africa with the second maximum over South America; yet, among geodetic sites the amplitude maximum of the load tide (see Appendix A) is achieved at the frequently observing VLBI station Katherine in Australia (1 mm) followed by station HartRAO (Hartebeesthoek Radio Astronomy Observatory) in South Africa.

The different impact of TU Wien and GSFC models in VLBI analysis is assessed by means of relative variance reduction $\mathscr{R}$ expressed in percentage:

$$\mathscr{R} = \frac{\mathrm{BLR}_m^2 - \mathrm{BLR}_0^2}{\mathrm{BLR}_0^2} * 100\% \tag{4.18}$$

where BLR_m denotes a solution where the geophysical model (TU Wien or GSFC) is used and BLR_0 represents a solution without this model (Table 4.4). The variance reduction is calculated for the baseline length repeatability (BLR):

$$\mathrm{BLR} = \sqrt{\frac{\sum w_i (b_i - \bar{b})^2}{\sum w_i - \frac{\sum w_i^2}{\sum w_i}}}, \qquad \bar{b} = \frac{1}{n} \sum b_i, \tag{4.19}$$

where b_i is a baseline length and $\bar{b}$ is a mean baseline length, w_i is weighted value based on correlation matrix data provided by the LSA (Figure 4.1).

The relative variance characterizes a ratio of the squared repeatabilities per baseline to measure the geophysical model impact for each applied model. For this reason the station coordinates are introduced in the parametrization of the single session solution, which inclusion is only difference from the aforementioned final parametrization (Figure 4.4). As follows, several solutions are obtained additionally for this study (Table 4.4), that is, two solutions with respect to both TU Wien and GSFC (tidal and non-tidal loadings included) and two solutions for each provider
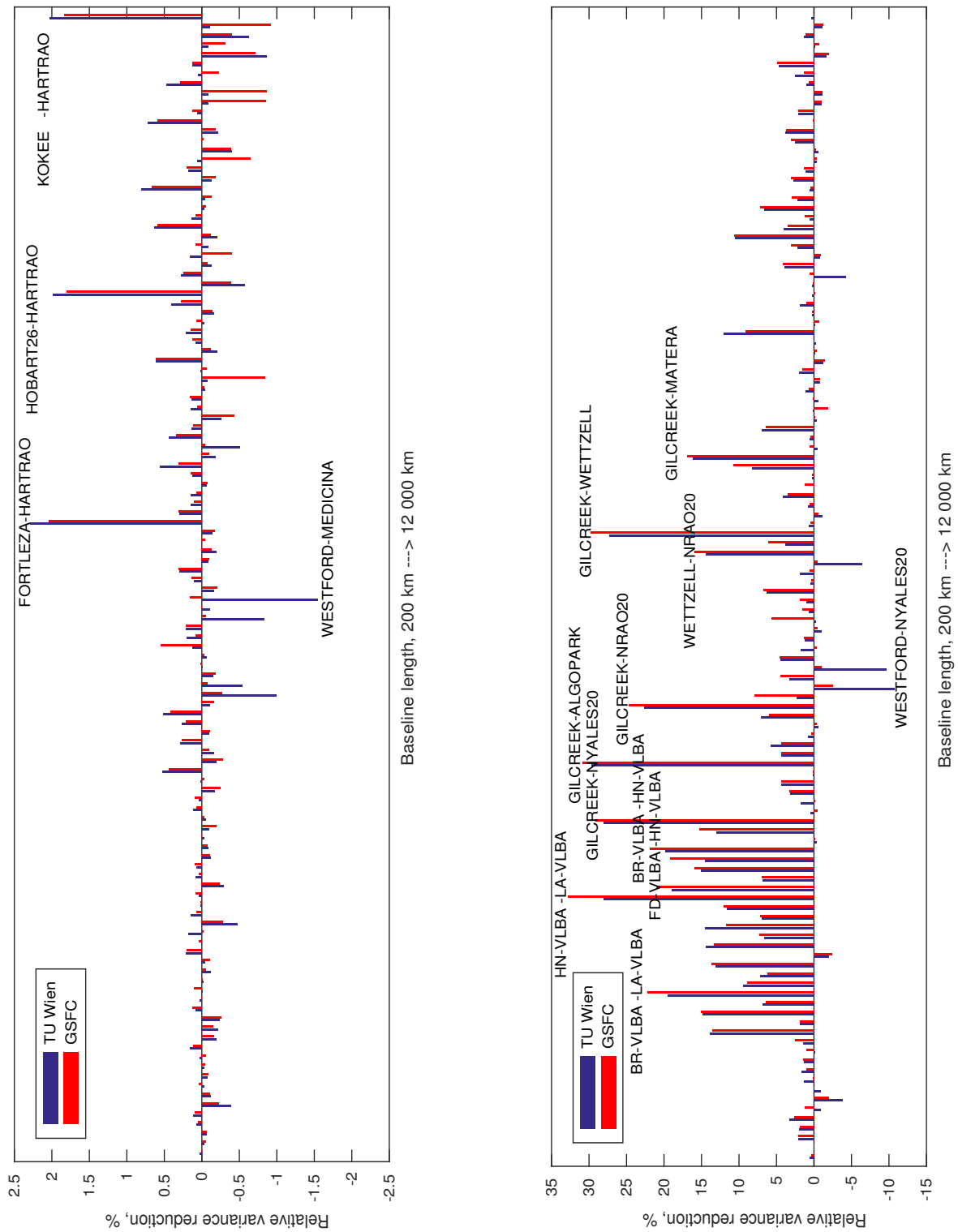
Figure 4.9: Relative variance reduction for VLBI baseline length repeatabilities when applying tidal (right panel) and non-tidal (left panel) loading models by TU Wien and GSFC. Reference solutions are those without loading corrections.

Solution	Included part of atmospheric model TU Wien/GSFC	Ocean model included as FES2004
1	Tidal and non-tidal	Tidal
2	Tidal	Tidal
3	Non-tidal	Tidal
4	Tidal and non-tidal	No model included
5	Tidal and non-tidal	Tidal FES2012

Table 4.4: Solutions are performed to study different models accounted for geophysical effects. The combination of first and third solutions is used to assess atmospheric tidal contribution; the first and second solutions provide a result of the atmospheric non-tidal loading; based on first, forth and fifth solutions the ocean loading impact is tested.

disregarding tidal and non-tidal loading (two solutions as well). To calculate relative variance, the baselines are required to be involved in observations in at least 100 sessions and the tidal and non-tidal loadings should be available from both models for each station over the duration of all sessions. Thus, a number of baselines was excluded in this comparison because of these restrictions.

The results derived from these solutions (Table 4.4) are used to represent the atmospheric tidal loading comparison in the left panel and non-tidal loading in the right panel (Figure 4.9), where the positive half plane contains the baseline length repeatabilities improved by applied corrections. This practical implementation of the tidal and non-tidal atmospheric loadings proves that the results from models by TU Wien and GSFC exhibit statistically insignificant discrepancies. Only a couple of baselines evince improvement in usage of one model instead of the other. For instance, TU Wien model indicates a better account for the tidal loading for baselines Fortleza-HartRAO (Fortleza is accepted shortcut for station in Fortaleza, Brazil) and Kokee-HartRAO (Kokee located in Kauai, Hawaii). By looking at the scattering in Figure 4.9, the relative variance reduction can be found smaller in the case of atmospheric tidal loading than for atmospheric non-tidal loading for both models. By this reason, the non-tidal part of atmospheric loading should be introduced in reductions. However, these corrections are still not a part of the IERS Conventions due to the lack of agreement on which existing model of the non-tidal displacements and a specific procedure for the geodetic reductions may be recommended.

The oceans were already shown to induce larger signals than the atmosphere in the high-frequency ERP band. The ocean loading corrections to the station positions also account for a considerably stronger forcing at the same frequency band as atmospheric loadings. Consistent atmospheric and ocean models need to be applied in the single session solution, because the sum of these corrections is assumed to reduce simultaneously the corresponded geophysical effects. Two ocean model realizations, FES2004 and FES2012 (Lyard *et al.*, 2004, 2006, 2012) were chosen in order to complement to atmospheric models. Loadings from both FES models are calculated on a non-standard mesh and released on a uniform grid, which is different from other models. Besides, FES models are obtained with a much finer resolution compared to the utilized atmospheric models, where the grid is improved for FES2012. The most important characteristic for
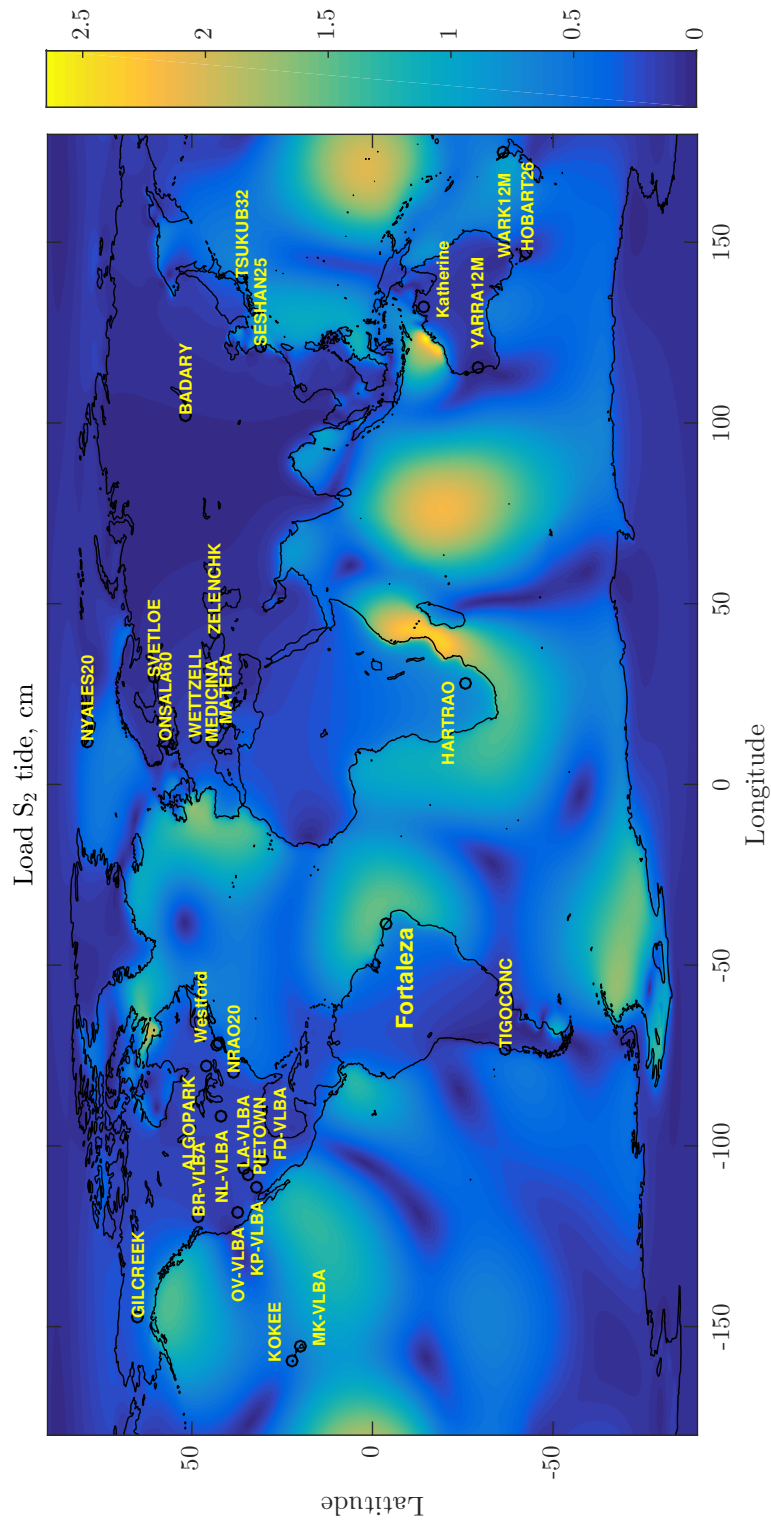
Figure 4.10: S$_2$ load tide from FES2014 ocean model. Frequently observing VLBI stations used in this thesis are added. The maximum of this load tide is found for station Fortaleza.
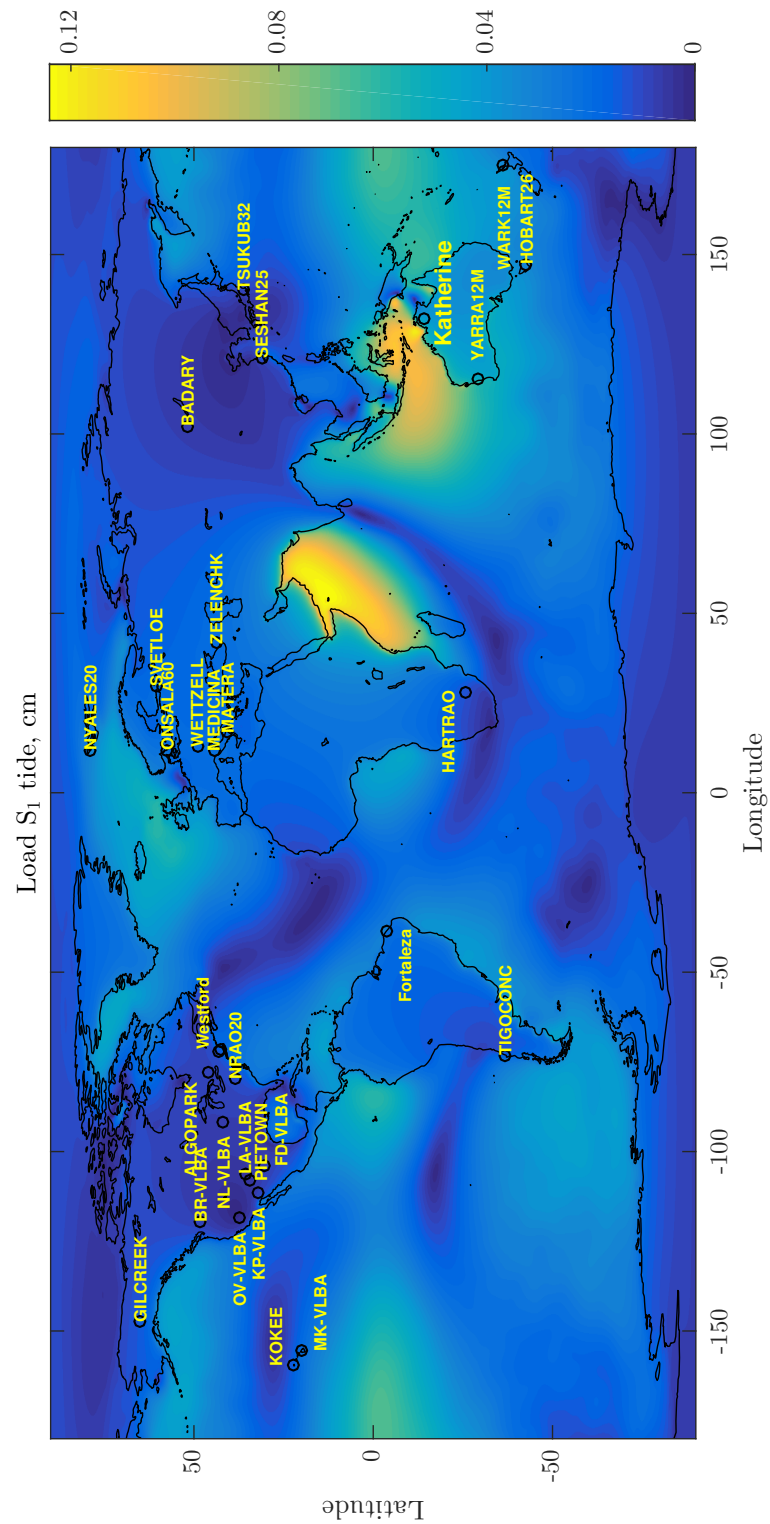
Figure 4.11: The load tide associated with the ocean response at the S_1 frequency as provided by FES2014 ocean model. Frequently observing VLBI stations used in this thesis are added. The maximum of this load tide is found for station Katherine.
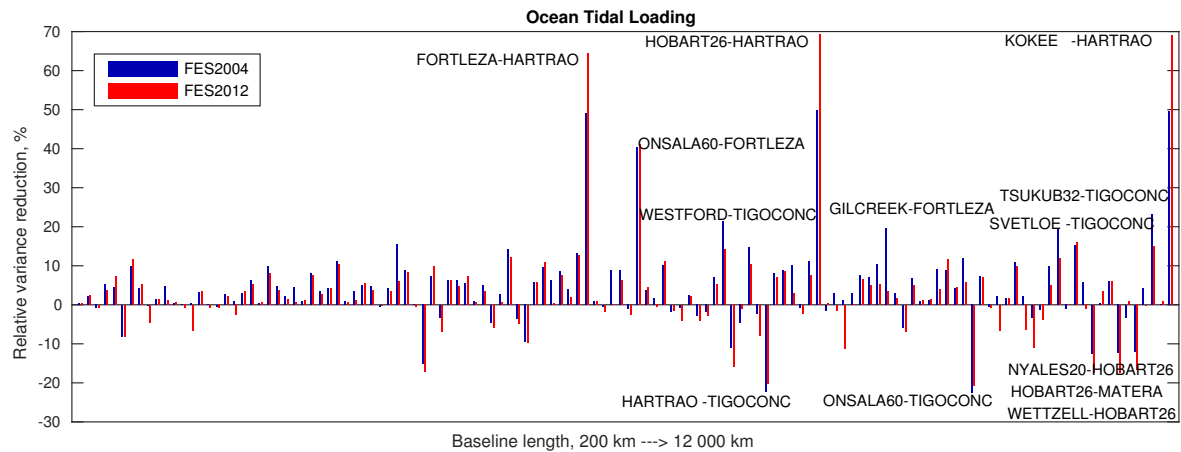
Figure 4.12: Relative variance reduction for VLBI baseline length repeatabilities when tidal ocean loading model is applied by FES2004 or FES2012. Reference solutions are those without loading corrections.

the joint application of ocean and atmospheric models is that the weather model for TU Wien and FES2012 models is common. Thus these models have a better consistency than other potential combinations (cf. GSFC and FES2012).

FES2004 or FES2012 (Lyard *et al.*, 2006, 2012) model report the set of the high-frequency and long-term ocean tides (specified in Section 3.2.1). Especially, the loading effects for the S_1 and S_2 tides are important to be introduced in the model properly, because atmospheric tidal loading exposes signals at the same frequencies. Only the last realizations FES2012 and FES2014b (Lyard *et al.*, 2012, 2014) provide the hydrodynamic response at the S_1 frequency. The load tide associated with the S_1 frequency is of non-gravitational origin and related to the hydrodynamic ocean response to atmospheric forcing. The ratio between this forcing mechanism and atmospheric load S_1 tide can be seen by considering Figure 4.11 in comparison with Figure 4.8. The maximum of atmospheric loading is approximately 10 times larger and, thus, the ocean response to this forcing is not included in the routine reductions. At the other frequency, the amplitude of the S_2 load tide is induced mainly by gravitational origin (Figure 4.10) and less by atmospheric loading. Thus, the hydrodynamic response to the atmospheric forcing is difficult to separate (Arbic, 2005), and it is assumed currently to be included in the ocean budget.

The ocean tidal loading influence in station coordinate changes is tested similar to the atmospheric forcing by means of the relative variance reduction between the two models (FES2004 and FES2012) described in Table 4.3. Corresponding solutions (Table 4.4) are obtained using these models, where the reference solution does not account for ocean loading at all (the forth entry in Table 4.4, the parameter BLR_0 in equation (4.18)) and BLR_m is based on FES2004 or FES2012 model (the first and fifth entries in Table 4.4 accordingly). The station displacements were calculated by M. S. Bos and H.-G. Scherneck (Ocean tide loading provider, Bos & Scherneck (2007)) for FES2004 and by Leonid Petrov (International Mass Loading Service, Petrov (2015)) for FES2012. Again the positive half plane (Figure 4.12) depicts baseline repeatability improved by using FES2004 or FES2012 models. Especially, the largest discrepancies (about 20%) can
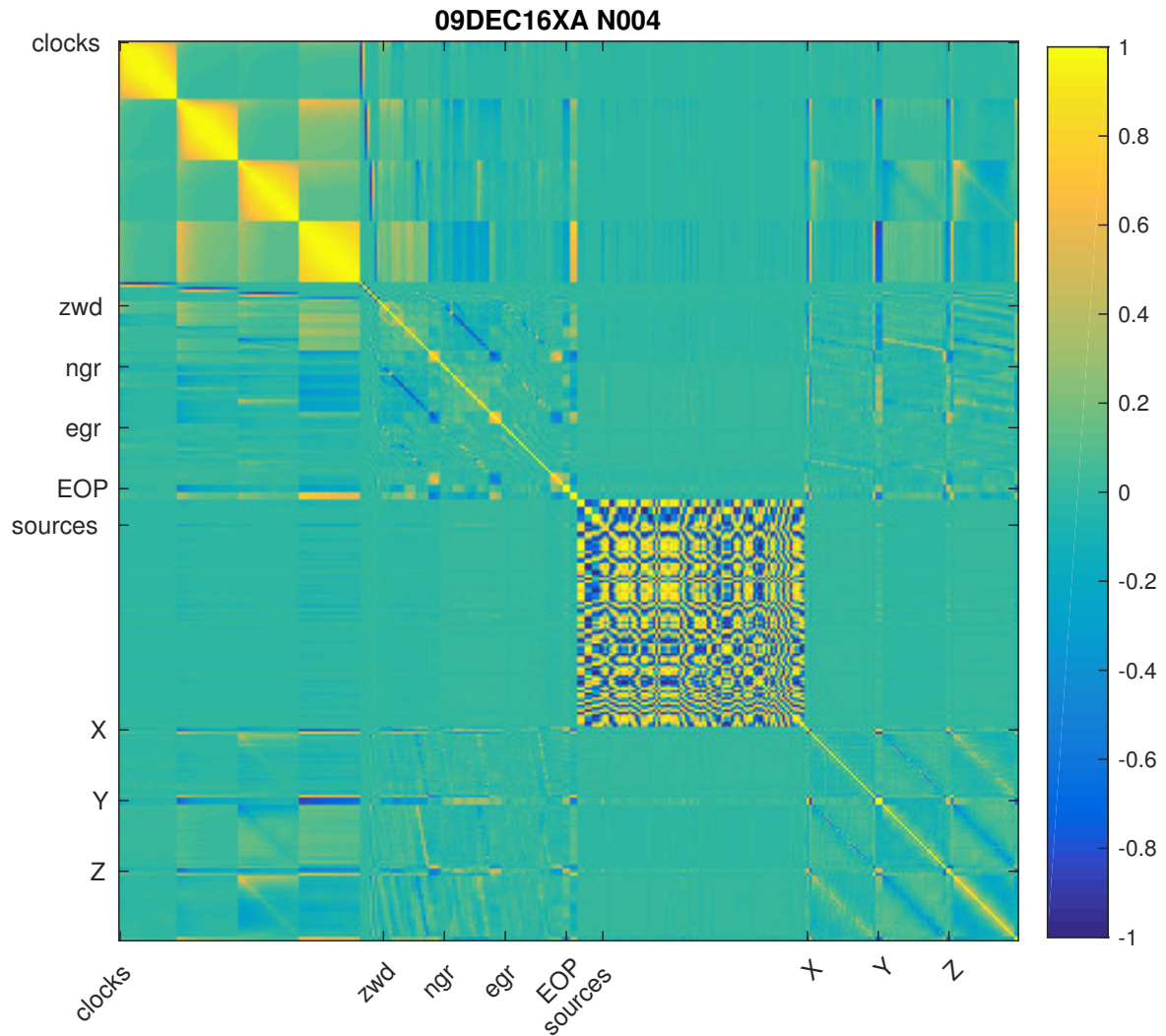
Figure 4.13: The symmetric correlation matrix of single session 09DEC16XA_N004 illustrates the single session parametrization where station positions are estimated hourly.

be found for baselines Fortaleza-HartRAO, Hobart26-HartRAO (Hobart26 located in Tasmania, Australia), Kokee-HartRAO, for which the updated FES2012 ocean model represents a better values. Also, several baselines show degradation of model performance (about 20%), which require further investigation. Overall, similar to the comparison between different atmospheric loading providers no evidence can be seen that one of the ocean models prevails over the other.

4.3.3 Tidal signals in variations of the station positions

As it was demonstrated in the previous Section 4.3.2 by means of the BLR, the station coordinates experience the atmosphere pressure loading and ocean loading effects as a consequence of mass variations in fluid layers. On the one hand, the corresponding account is provided by various numerical models as already discussed in Section 4.3.2. On the other hand, it is possible to estimate daily tidal loading contribution directly in the high-frequency variations of station

Figure 4.14: Zenith wet delay estimated of 6-hour intervals (red) and 1-hour intervals (blue).

positions. The idea of this approach is to assemble the time series of station coordinates for those stations where the atmospheric signals are close to maxima of the pressure field variations (Figure 4.8). At least, the detection of the largest diurnal S_1 atmospheric signal in variations of station position is expected, because amplitude maximum of the atmospheric load tides is about 1 mm. Moreover, the radial component of the S_1 tide is evaluated only. An assessment of its horizontal displacement is discarded in view of their significantly smaller amplitudes. These corrections are on the sub-millimeter level which is currently unacceptable in the VLBI analysis.

To resolve daily effects of the atmospheric tides, the station coordinates need to be estimated more frequently than once per session. To realize this requirement, the standard LSA with the parametrization shown in Figure 4.1 is extended by increasing the number of intervals per station from the one offset (daily) to an hourly basis and relative, very loose, constraints of 10 cm are introduced to the normal equations. These constraints are the same as for daily estimates (Table 4.2). The new matrix parametrization includes three blocks of the hourly station position estimates in accordance with three-dimensional rectangular coordinates (X, Y, Z). Internal variations among all station estimates in Figure 4.13 within of these blocks are assumed to be acceptable for this analysis since the largest signal in radial component is intended to be study only. Also, this analysis requires to adjust the zenith wet delay ZWD interval. In the regular parametrization, it is preferable to estimate zenith wet delay as frequently as possible (20 min till 60 min). Owing to the dependence on the elevation angle e for the zenith wet delay given in equation (4.13) and the station positions in equation (4.15), with assumptions concerning the interval in equation(4.10), the zenith wet delay estimation interval is replaced by a longer time step of 6 hours. These ZWD estimates at 6 hourly basis demonstrates a good approximation to the standard hourly estimates without a rise of standard deviations (Figure 4.14). While it is impossible to avoid these correlations with atmospheric parameters in the parametrization entirely, different underlying models can improve estimates and their standard deviations. For this purpose, the ray-traced delays are introduced as a prior model for the north and east gradients and the zenith wet delay. It was indicated (Hofmeister, 2016) that usage of the ray-traced delays can
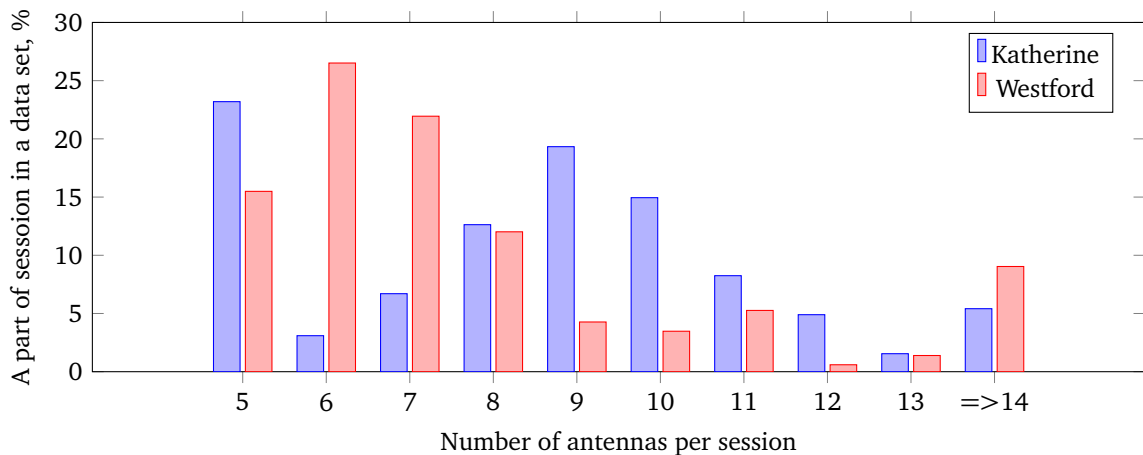
Figure 4.15: The distribution of sessions in accordance with the number of participated stations per session. The relative values are shown for two separate data sets, for Katherine and for Westford.

lead to improvement of the parameter estimates in the analysis of VLBI observations, so several solutions with fixed gradients are undertaken to test this possibility.

In this modified parametrization implementation of the TRF definition should be reformulated accordingly. Usually, a TRF evaluation is represented in solutions by means of station positions estimated by one offset per session for every station in the datum. An origin of the reference frame is obtained from observations along with station positions and other parameters during one session. This approach requires the additional constraints to be introduced in each solution. Thus, for stations in the datum the Helmert transformations are applied by means of no-net-rotation (NNR) and no-net-translation (NNT) conditions. The frame origin has to be common for terrestrial and celestial reference frames, therefore these limitations need to be introduced to define them uniquely. In the case of source coordinates it is sufficient to estimate the coordinates of that sources which are not included in this datum and apply relative constraints if it is considered necessary. The datum of stations is reported by ITRF data, where the reference stations are chosen on the basis of the reliability of available coordinates and their stability in time. The station of interest, where the hourly estimation interval is set, is excluded from the datum on this occasion only (even though these station positions are recommended to use by ITRF). The main reason is that the harmonic variations of hourly estimates propagate in variations of other stations once it is included in the datum.

One of the VLBI stations, Katherine, is chosen as a station of interest. This station is located in an area next to region of the maximum of the atmospheric loading (see Figure 4.8). The ocean response on the S_1 frequency can be used by the ocean tide model, for instance, FES2012 (Figure 4.11). The maximum of the FES2012 model is found for Katherine. The coincidence of these conditions and availability of the models allow this analysis to evaluate the atmospheric part separately.

The Australian network was exceptionally active in the last years (2014-2015) under the project AuScope. These data made available the extension of the original data set with new

sessions. The sessions from this combined data set, in which Katherine participated and match the selection criteria, are spread densely over 5 years: 389 sessions mid-June 2011 until the end of February 2016, and compose 365 000 residuals. By an empirical approach the 5-station network is found to represent the smallest network which is suitable to provide a stable datum; the rest of stations is sufficient to define an origin properly, if one is excluded. To indicate the considerable global coverage of selected data, the distribution of antennas participated per session is shown in Figure 4.15 for Katherine, where the most of data set (23% and 19%) is presented by sessions consisting of 5 and 9 antennas. Also, an amount of sessions composed on large networks of 8 and 10 participated stations (15% and 13%) is sizable, so this data set is appropriate for further analysis.

In contrast to the Katherine solution, station Westford in North America is selected as an example of small modeled corrections to station positions based on pressure variations in one of the regions of the minimum amplitudes (see Figure 4.8). The ocean response at the S_1 frequency can be neglected in this area. Westford has a much longer history of observations combined 930 000 residuals, but they are sparse in time: in sum 1025 sessions fall in the period of January 1995 till September 2014. These sessions were extracted from the original data set given in Table 4.1. By analogue to represent the global character of chosen sessions in the data set obtained for Westford, the dependence on antenna number per session illustrates (Figure 4.15) that the datum per a single session solution also can be provided successfully.

4.4 Global solution vs. single session solution

In VLBI analysis two methods are widely used: a single session solution and a global adjustment (or a global solution). As an extension to single session solution, the global solution is based on the normal equations obtained in single solution. Hundreds of single sessions, thus, are solved simultaneously by the LSA in global solution. The basic set of parameters, which can be estimated in both methods, is rather similar, yet instrumental and atmospheric parameters are normally not considered in a global adjustment, because normal equations are collected over a much longer time span than the periodicities of these parameters. During the time interval of 20 years in the current processing the global solution supplies the parameter estimates of TRF, CRF, the high-frequency tide terms and axis offsets with a better accuracy, however the single session solution provides advantages for a study of dynamical processes, in particular for the finalized parametrization (Figure 4.4).

The goal of global solution building is to achieve significant improvements in the consistent determination of TRF, CRF and EOP, i.e., the main products of geodetic VLBI. At the dawn of VLBI, all stations demanded the definition of positions with high accuracy. Currently, the same procedure is needed for new stations which join the working network such as the modern Australia-New-Zealand network or the brand-new Onsala Twin telescopes. For these stations the single session solution exhibits large offsets with respect to a priori values, which implies that a priori

coordinates need to be estimated more accurately. The global solution is the best approach to determine these coordinates as soon as enough observations become available.

When a reliable TRF and CRF are determined along with EOP, the global solution can be devoted to smaller effects. For instance, the high-frequency ERP tide terms were introduced as the global parameters by Böhm (2012). In this thesis, the alternative approach of the single session solution is applied as the supplementary method to evaluate the high-frequency tide terms. To testify the adequacy of the main assessment, the global solution (Böhm, 2012) is applied for the same sessions as those utilized in the single session solution. To obtain this global solution normal equations are provided by single session solution with parametrization shown in Figure 4.1. Finally, station and source positions were estimated along with tide terms and axis offsets (Krásná, née Spicakova, 2014). The tide terms derived from the global solution are included in Tables B.3 and B.4 and discussed in details in the next Section 5, where the same tide terms are calculated based on the single session solution.

Chapter 5

Detection of the atmospheric tides

The small amplitudes of diurnal and semidiurnal atmospheric tides set a challenge to determine them properly. These effects are deduced in a consistent approach with ocean tides by means of relevant methods represented in this Chapter. The present assessment is dedicated to the atmospheric forcing at the S_1 frequency, which provides a larger contribution over the other excitation sources at this frequency (Ray & Egbert, 2004). The oceanic and atmospheric origins of the S_2 tide cannot be separated easily (Arbic, 2005), thus the S_2 tide is discussed moderately below.

In this chapter, the diurnal and semidiurnal tide terms are evaluated in VLBI-based time series of the high-frequency Earth Rotation Parameters time series. The supplementary study results of daily and sub-daily harmonic station position variations are demonstrated as well. The interdependencies between two these aspects of atmospheric tidal forcing, however, are inaccessible as it is shown in the current processing of the available VLBI data set.

5.1   Method description

The method of the LSA overcomes limitations of the standard method of the frequency analysis, since the obtained data set is inappropriate to resolve all tidal frequencies and phases correctly. The parameter set of the LSA is specified by the sought-for tides, and accordingly a design matrix consists of trigonometric functions with tidal arguments at pre-defined frequencies given by TGP. These orthogonal functions (sinus and cosine parameters) with arguments ω_i based on Delaunay variables compose the corresponding parametrization matrix A for the direct use in the LSA:

$$
A \;=\; \begin{pmatrix} \ldots & \ldots & & \ldots & \ldots \\ \ldots & \cos\omega_i(t_j) & \sin\omega_i(t_j) & \ldots \\ \ldots & \ldots & & \ldots & \ldots \end{pmatrix}^{t_N}_{t_1} . \tag{5.1}
$$

The total number n_{tides} of the considered high-frequency tide terms i is calculated for each
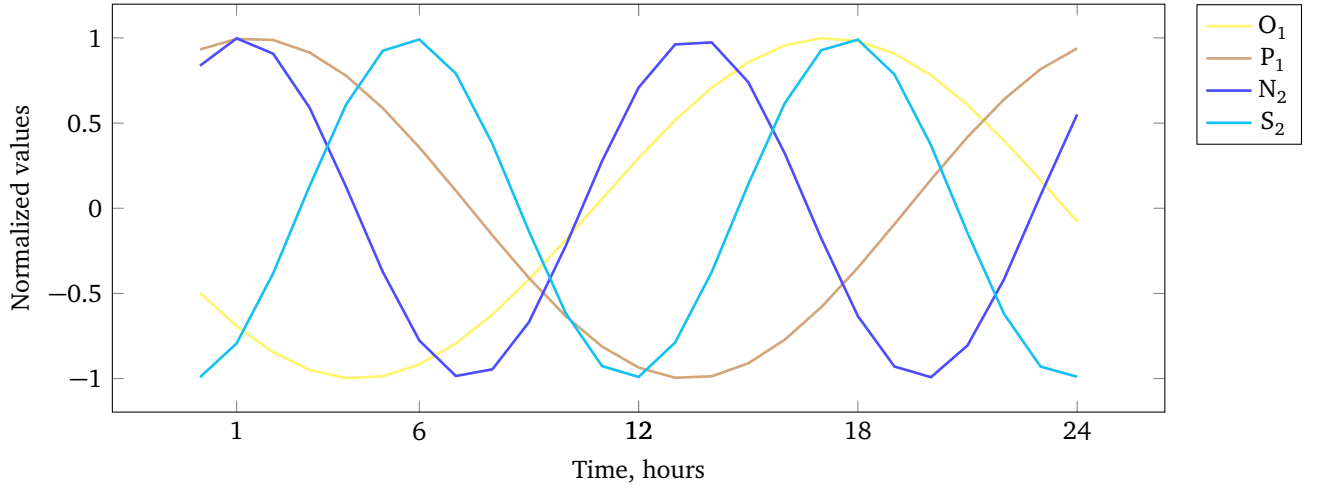
Figure 5.1: Normalized harmonic functions for the cosine parameters are calculated on the basis of Delaunay arguments.

epoch t_j in period of $[t_1 : t_N]$ as given in the obtained time series of the high-frequency ERP (see Section 4.3.1). These tide terms are listed in Table B.1 (Appendix B) and supplied with Delaunay variables. A simulation on the basis of equation (2.28) using data in Table 5.1 (a shortcut of Table B.1 for eight major tides) can be performed to represent the typical harmonic variations which constitute TGP and, consequently, parametrization matrix A. Several of these modeled waves (cosine parameters $\cos \omega_i$) in the diurnal (O_1 and P_1) and semidiurnal (N_2 and S_2) bands can be seen over one day in Figure 5.1. Normalized amplitudes imply that the a priori model is not stipulated. When amplitudes are taken from the IERS Conventions model, a priori variations (Figure 5.2) can be computed as the sum among the eight major tide terms. Also, the variations of observed values around this modeled sum are displayed in Figure 5.2, where the high-frequency polar motion time series derived from the reduced data set (see Section 4.3.1) serve as observed values and their formal errors σ_{obs} provide error bars per value. These observed data ERP_{obs} were already combined with the model (Figure 5.2) to provide the vector of observations in the form of $\hat{b} = (ERP^0 + ERP_{\text{obs}})$. In this case, the total amplitudes $\widetilde{A}$ of tidal terms are evaluated by means of the weighted LSA, where the normal equation system with weight matrix P can be expressed:

$$N\widetilde{A} = A^{\text{T}} P \hat{b}, \tag{5.2}$$

and the variables are

$$N = A^{\text{T}} P A, \quad Q = N^{-1}, \tag{5.3}$$

Tide	Fundamental arguments						Period	A^+	B^+	A^-	B^-	σ
	GMST+π	l	l'	F	D	Ω	(cpd)	µas	µas	µas	µas	µas
Q_1	1	-1	0	-2	0	-2	1.1195	-27.9	8.7	-3.5	-1.0	2.1
O_1	1	0	0	-2	0	-2	1.0758	-129.1	59.3	-1.9	1.9	2.1
P_1	1	0	0	-2	2	-2	1.0027	-49.1	25.6	-3.3	1.5	2.1
K_1	1	0	0	0	0	0	0.9973	156.9	-98.4	0.8	-3.4	2.2
N_2	2	-1	0	-2	0	-2	0.5274	9.5	-11.1	-2.5	40.2	2.1
M_2	2	0	0	-2	0	-2	0.5175	32.4	-73.2	-20.8	255.3	2.1
S_2	2	0	0	-2	2	-2	0.5000	-6.3	-33.9	-78.5	110.6	2.1
K_2	2	0	0	0	0	0	0.4986	2.7	-12.6	-16.5	24.5	2.2

Table 5.1: The fundamental arguments, periods and tide coefficients are listed for eight major tide terms. Corresponding tide coefficients and their formal errors are calculated from the high-frequency time series obtained by the single session solution using reduced data set (see Section 4.3.1).

which provide the solution for total amplitudes of tidal terms:

$$\widetilde{A} = QA^{\mathrm{T}}P\hat{b}. \tag{5.4}$$

By using formal errors σ_{obs} of the observed high-frequency time series ERP_{obs} obtained from the VLBI data analysis of the single session solution (see Section 4.3.1) at the epoch t_j, each element p_j of the diagonal weight matrix P is

$$p_j = \frac{\sum_{j=1}^{N} \sigma_{j\,\mathrm{obs}}^2}{\sigma_{j\,\mathrm{obs}}^2 (N - n_{\mathrm{tides}})}, \tag{5.5}$$

Obtained residuals $\hat{r}$ to the observed time series $ERP_{\mathrm{obs}} + ERP^0$:

$$\hat{r} = A\widetilde{A} - (ERP_{\mathrm{obs}} + ERP^0), \tag{5.6}$$

can be characterized by the variance of unit weight χ^2:

$$\chi^2 = \frac{\hat{r}^{\mathrm{T}}P\hat{r}}{N - 2 \times n_{\mathrm{tides}}}, \tag{5.7}$$

to define the standard deviations $\{\sigma_i\}_{i=1}^{n_{\mathrm{tides}}}$ for the tide amplitudes included in the parametrization A:

$$\sigma = \chi \sqrt{diag(Q)}. \tag{5.8}$$
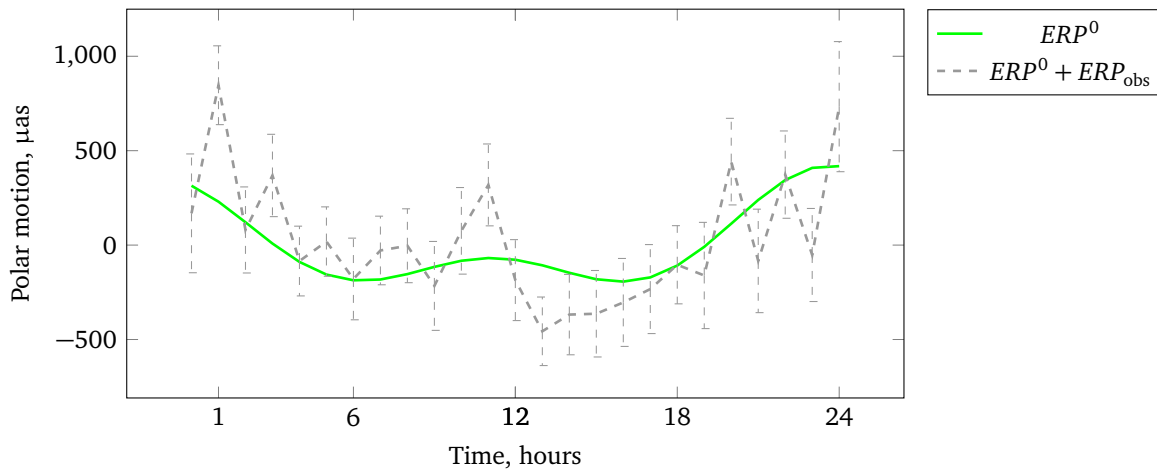
Figure 5.2: The sum of eight major harmonic functions is shown based on the high-frequency model (recommended by the IERS Conventions, green line) and this model in sum with estimates from observations (dashed line).

The LSA is a universal method to obtain a best fit ($\chi^2 = 1$) of required parameters. In general, the implementation described in this section suits for any data, in which harmonic signals are combined, in particular, the high-frequency ERP time series and the daily and sub-daily station position variations. Both sets are processed with focus on the atmospheric contribution at the S_1 frequency.

5.2   Earth Rotation Parameter time series analysis

In this part atmospheric tides are considered to affect the high-frequency Earth rotation. This impact is assessed by means of three methods of the Time Series Approach (TSA) simultaneously with ocean tides in the diurnal prograde band and the semidiurnal prograde and retrograde bands. The retrograde component of S_1 as well as other diurnal signals is related to nutation (Schindelegger *et al.*, 2016), and should be observed in celestial pole offsets which are provided in VLBI analysis internally at the step of the a priori EOP determination. This artificial separation is rigorous, thus, in practice some noises at the frequencies in the retrograde diurnal band can be retained (Tables 5.1 and B.1). To retrieve a small effect at the S_1 frequency over the potential noises two methods of the TSA were adjusted in addition to the standard approach. The first method (standard approach) resolves a system of normal equations for 70 tide terms in the same adjustment. These terms chosen with respect to the IERS Conventions (71 tide term) include the S_1 frequency given by the set of Delaunay arguments (1, 0,-1, 0, 0, 0), where the atmospheric impact is introduced, and exclude another frequency related to the S_1 tide (1, 0, 1,-2, 2,-2). Because these two frequencies are extremely close (separated by the long-term argument p_s, see Section 2.2.3), they cannot be determined together by means of the LSA for the pre-defined tides. In contrast, two additional methods separate the S_1 tide from the other terms of the tide model and assess it alone. The treatment in the second method is applied for the time series, where harmonic variations of
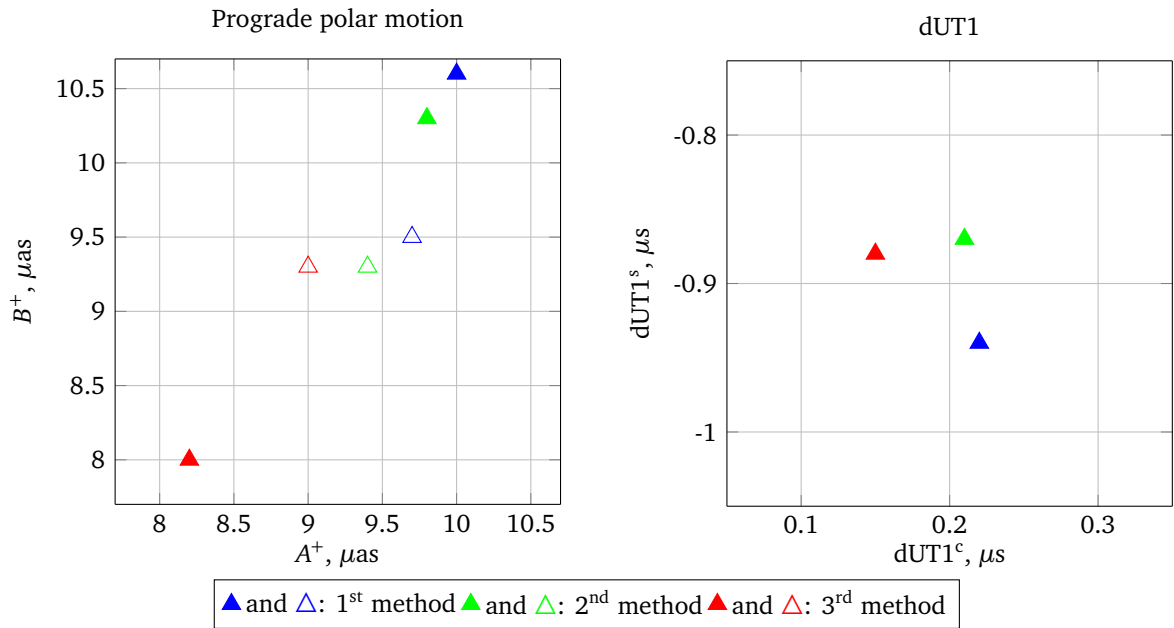
Figure 5.3: Estimates of S_1 in polar motion (left side) for the complete (unfilled triangles) and the reduced (filled triangle) data set and dUT1 (right side) for the complete/reduced data set (indistinguishable) derived from the three methods of the TSA. Blue color denotes estimates of the first method, green color of the second method and red color of the third method.

the 69 tides collected in the first method were subtracted. In the third method these time series are rearranged into stacks of 24 hour to simulate the time series of S_1 signal. The evaluated total amplitudes of the atmospheric S_1 tide are shown in Figure 5.3 as derived from the complete and reduced data sets (Section 4). These values might slightly deviate from the results in Table B.1 due to the fact that the high-frequency ERP time series were obtained based on marginally different observations. While a range of different estimates can be seen for polar motion in dependence on the TSA and used data sets, the S_1 solutions in dUT1 are indistinguishable, so that triangles in the right part of Figure 5.3 depict both data sets outcomes. Since the usage of the TSA for complete and reduced data was indicated (Girdiuk *et al.*, 2016b) to cause larger differences among the obtained S_1 estimates than the change in the background model of the mapping function, Vienna Mapping Function 1 (VMF1) and Global Pressure and Temperature, version 2 (GPT2), or the temperature, GPT2 and VLBI data file (NGS-file), a representation of those influences and a study of the other smaller causes are omitted in this thesis.

5.2.1 The first method

The standard harmonic models of diurnal and semidiurnal oscillations in polar motion read

$$
\begin{aligned}
x(t_j) &= \sum_{i=1}^{n} \left[(-A_i^+ - A_i^-)\cos\alpha_i(t_j) \;+\; (B_i^+ - B_i^-)\sin\alpha_i(t_j) \right], \\
y(t_j) &= \sum_{i=1}^{n} \left[(B_i^+ + B_i^-)\;\cos\alpha_i(t_j) \;+\; (A_i^+ - A_i^-)\sin\alpha_i(t_j) \right],
\end{aligned}
\tag{5.9}
$$

where coefficients next to the trigonometric functions are estimated by means of the LSA and, in general, form the resultant $\widetilde{A}$. In particular case of equation (5.9), $\widetilde{A}$ can be substituted by $x^{\cos}$, $x^{\sin}$, $y^{\cos}$, $y^{\sin}$ for both ERP time series $x = x(t_j)$ and $y = y(t_j)$, where $t_j \in [t_1 : t_N]$. Hence, the coefficients of the components of polar motion can be written as follows:

$$
\begin{aligned}
x^{\cos} &= -A_i^+ - A_i^-, & x^{\sin} &= B_i^+ - B_i^-, \\
y^{\cos} &= B_i^+ + B_i^-, & y^{\sin} &= A_i^+ - A_i^-,
\end{aligned}
\tag{5.10}
$$

where $\{A_i^+, B_i^+\}$ denote harmonic variations in prograde polar motion and $\{A_i^-, B_i^-\}$ in the retrograde polar motion:

$$
\begin{aligned}
A_i^+ &= -\tfrac{1}{2}(x^{\cos} - y^{\sin}), & B_i^+ &= \tfrac{1}{2}(x^{\sin} + y^{\cos}), \\
A_i^- &= -\tfrac{1}{2}(x^{\cos} + y^{\sin}), & B_i^- &= -\tfrac{1}{2}(x^{\sin} - y^{\cos}).
\end{aligned}
\tag{5.11}
$$

The diurnal and semidiurnal variations of the third parameter dUT1, which describes the Earth rotation, are expressed easier than polar motion because of an independence on the other components

$$
\mathrm{dUT1}(t_j) = \sum_{i=1}^{n} \left[\mathrm{dUT1}_i^{c}\cos\alpha_i(t_j) \;+\; \mathrm{dUT1}_i^{s}\sin\alpha_i(t_j) \right],
\tag{5.12}
$$

or in terms of LOD

$$
\mathrm{LOD}(t_j) = \sum_{i=1}^{n} \left[\mathrm{LOD}_i^{c}\cos\alpha_i(t_j) \;+\; \mathrm{LOD}_i^{s}\sin\alpha_i(t_j) \right],
\tag{5.13}
$$

and their coefficients are related in accordance with the requested tide frequencies ν_i in radian:

$$
\mathrm{LOD}_i^{c} = -\,\mathrm{dUT1}_i^{s}\cdot\nu_i, \quad \mathrm{LOD}_i^{s} = \mathrm{dUT1}_i^{c}\cdot\nu_i.
\tag{5.14}
$$
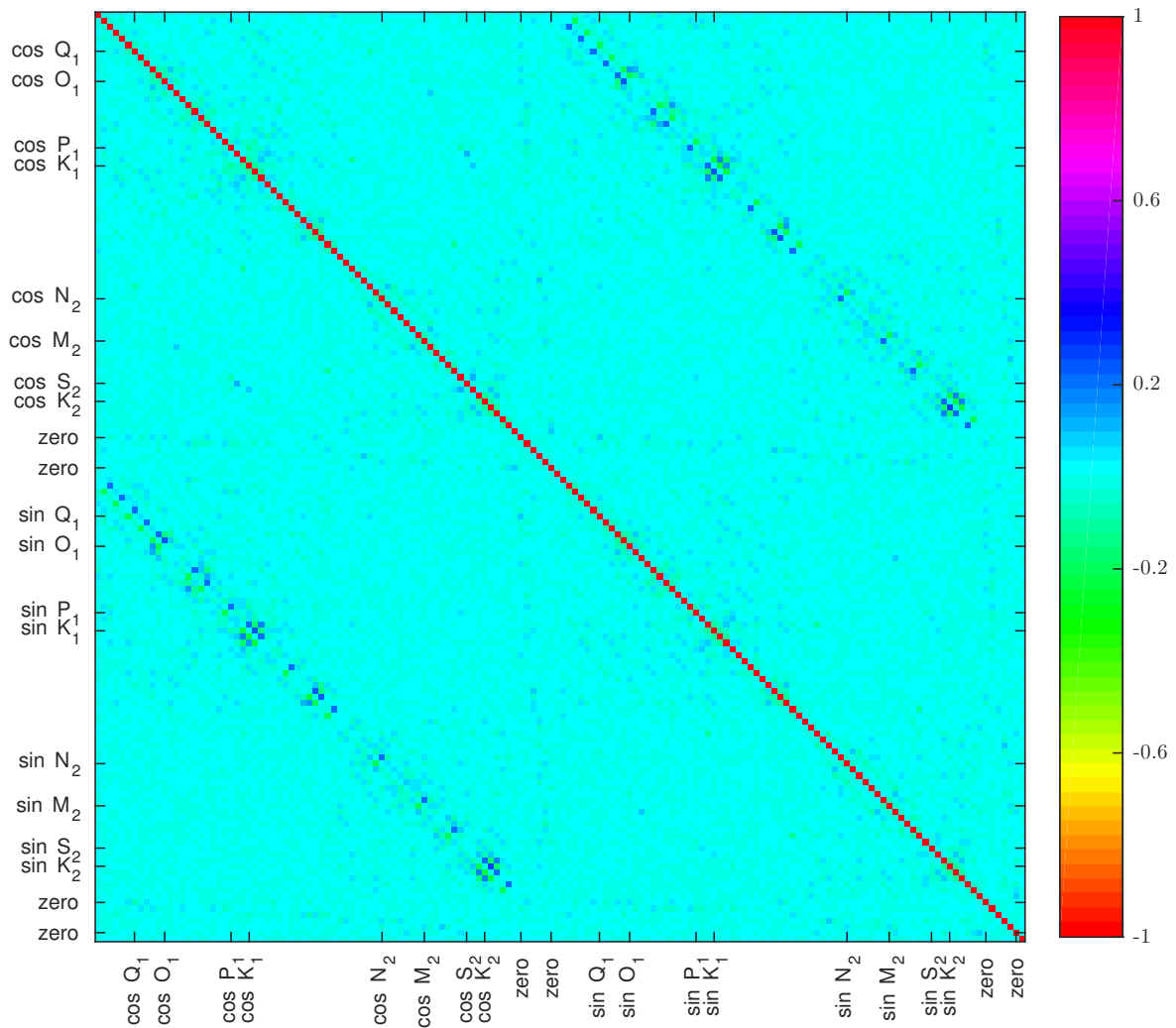
Figure 5.4: The symmetric matrix includes dependencies among 70 tide terms and set of six zero tides obtained by means of the first method. Cosine and sine components are marked for the major tides by horizontal and vertical axes correspondingly. Similar, six zero tides are represented in-between labels 'zero'.

These coefficients given in equations (5.11) and (5.14) were evaluated in the first (standard) method applied in this thesis for 70 tide frequencies and zero tides, where no excitation signals based on TGP are expected (Table B.1). Zero tides are introduced as extension of the defined tides to provide an additional tool for statistical assessment with frequencies extracted from the work by Böhm *et al.* (2012, b). Namely, by means of zero tides a so-called noise threshold is determined in addition to the definition of 3 σ reliability level, so that all variations under this level are considered as insignificant. In the standard approach the obtained amplitudes of the atmospheric S_1 tide satisfies this limitation. In details, the S_1 tide in polar motion (Figure 5.3) shows a discrepancy of 1 μas between complete and reduced data sets, which is considered insignificant in view of the obtained level of onefold standard deviations (2.2 μas) or similar average among

zero tide amplitudes in the diurnal band (Table B.1). In dUT1 the amplitudes of the S_1 tide does not reveal any dependency on strategy of the data set selection as it can be seen for the polar motion. Besides, the onefold standard deviation in dUT1 (0.1 µs) is twice smaller than zero tide amplitudes in the diurnal band (Table B.1) and still S_1 estimate is above 3 σ-level.

The standard deviations for the tide terms coefficients in equation (5.11) can be computed by equation (5.8):

$$
\begin{aligned}
\bar{\sigma}_1(A_i^+/A_i^-) &= \frac{\sigma(x^{\cos})+\sigma(y^{\sin})}{2}, \\
\bar{\sigma}_2(B_i^+/B_i^-) &= \frac{\sigma(x^{\sin})+\sigma(y^{\cos})}{2},
\end{aligned}
\tag{5.15}
$$

where $\bar{\sigma}_1(A_i^+/A_i^-) \cong \bar{\sigma}_2(B_i^+/B_i^-)$, what implies that all of coefficients are accessed at the same accuracy level. An insignificant scattering of the standard deviations among the tide terms can indicate the absence of distortion factors at the particular frequencies. General dependencies are demonstrated by means of the covariance matrix Q based on the matrix P of known weights. A whole solution reliability for the other tides can be shown in polar motion in Figure 5.4, which correlations between tide terms reveal the same trends in dUT1. Thus, polar motion correlation coefficients can be specified as

$$
\rho(x^{\cos},x^{\sin}) = \frac{cov(x^{\cos},x^{\sin})}{\sigma_{x^{\cos}}\sigma_{x^{\sin}}} = \frac{Q}{\sqrt{diagQ\,diagQ^{\mathrm{T}}}},
\tag{5.16}
$$

The largest correlations appear for couples of the same tide components (cos Q_1, sin Q_1) in Figure 5.4, as expected because those components are orthogonal. The set of six zero tides are shown between labels marked 'zero'. A trace of the correlation coefficients can be conjectured but these displayed dependencies with other parameters are neglected. This important fact can serve as a validation for initially arbitrary choice of these zero tides (Böhm *et al.*, 2012, b).

5.2.2   The reconstruction method of the time series

The tide term amplitudes obtained in the first method can be constituted to equation (2.28) along with the appropriate fundamental arguments to define modeled time series. These time series can be considered as "perfect" to the extent that only modeled variations are included, and consequently any noises and unrecognized systematics relative to the original time series have no impact. With respect to the method of building, these time series are referred to as reconstructed time series.

Practically, the tide terms in Table B.1 excluding S_1 tide were used to compose the reconstructed time series to fit to the original ERP time series by means of the LSA similar to the first approach. The differences $\Delta\Theta(t_j)$ between the original and reconstructed time series at observed epoch t_j include the S_1 signal and inherit the noise and possible systematic effects from the original time series. These time series $\Delta\Theta(t_j)$ are used to estimate the S_1 tide only, adopting the

stochastic model from the first method. In this case, standard deviations ($\sigma \approx 2.1$ µas) of the polar motion coefficients at the S_1 frequency are almost equaled to the values of the first approach (Table B.1). Also, the statistical assessment in dUT1 is on the same level as in the standard approach.

In Figure 5.3 a change due to application of the second method can be seen within the 1σ level in polar motion. Since the same stochastic model is introduced this variation might not be significant. The advantage of this separation is the parametrization of the LSA, which contains only S_1 frequency and six zero tides. The closely located frequencies, the P_1, S_1 and K_1 triplet, thus, are divided between the reconstructed and original time series. This evaluation using two time series might prevent leakage of the signal from estimated frequencies, which one might expect based on the correlation matrix in Figure 5.4. In the current case, the potential for leakage is enhanced by the fact that the P_1 and K_1 are major tides and their amplitudes are approximately 5 and 15 times larger than the S_1 tide amplitude measured in polar motion. By this reason, the reconstructed time series is practicable method to focus on the subject of the interest, namely the S_1 tide. In dUT1 this approach is less efficient, yet the obtained estimate of the S_1 tide is valid.

Besides the LSA method to retrieve the S_1 tide, a window spectral analysis is worth being applied. The advantage of this method is its ability to detect irregular effects of atmospheric tides over different time spans, thereby giving clues about the instability on inter-seasonal and seasonal frequencies or even shorter. Thus, anomalies estimates from the VLBI analysis can be compared to results from geophysical modeling. For instance, weather phenomena such as El Niño and La Niña are recognized in atmospheric pressure fields and modulate tides to a considerable degree (Schindelegger *et al.*, 2017). Due to small amplitude variations and unequidistant samples in the obtained time series, a real detection of these events by means of the LSA is questionable and corrupted by large formal errors. Currently, it is concluded that the VLBI observations cannot be used to measure these events.

5.2.3   The stacked time series

The last method of the LSA implemented for evaluation of the S_1 tide only is a stacking approach. In this third method, the hourly ERP residual time series can be mapped to the S_1 tide cycle of exactly 24 hours duration by stacking values to a mean day composite of exactly 24 points $\{\Theta_k\}_{k=0^h}^{23^h}$ for each of ERP components labeled as Θ. The stacking by aid of a weighted average for each integer hour k with corresponding time stamps t_l (a subset of observed time moments t_j) is expressed as

$$\{\Theta_k\}_{k=0^h}^{23^h} = \sum_{l=1}^{N_k} \Delta\Theta(t_l)p_l \Big/ \sum_{l=1}^{N_k} p_l, \; p_l = \frac{1}{\sigma^2(\Delta\Theta(t_l))}, \tag{5.17}$$

where $\sigma(\Delta\Theta(t_l))$ is the formal error at epoch t_l in the original time series and N_k denotes the total count of ERP residuals $\Delta\Theta(t_l)$ used in the averaging at each hour. As an example, the stacked x- and y-components of polar motion are shown in Figures 5.6 and 5.7.

Figure 5.5: The number of observations N_k per hour.
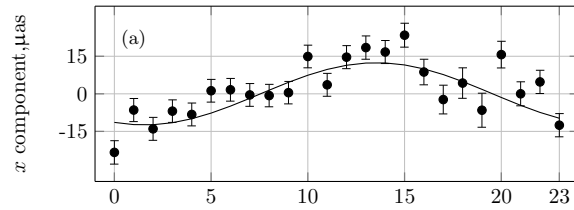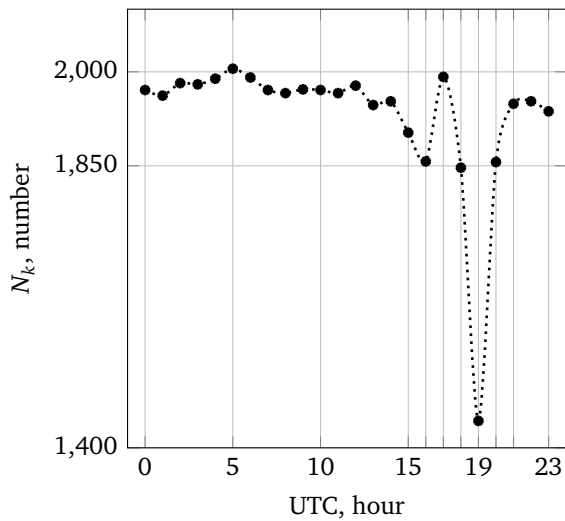
Figure 5.6: The stacked time series of x

Figure 5.7: The stacked time series of y

Finally, the diurnal harmonics, a 24-hour trend, and a mean value are adjusted to the stacked composites. The obtained sinusoids with hourly sampling are then repeated to simulate the S_1 series of several years duration. These time series are processed by means of the LSA with parametrization matrix which includes the S_1 tide only. The total S_1 amplitudes obtained thereof can be found (Figure 5.3) to suggest a smaller amplitude than the first and second methods. Similar to the differences between these first two methods, the third solution possesses an insignificant discrepancy on the formal error level.

Even though the results among these methods are rather similar, the third method is exceptional because its analysis revealed an interesting detail on the technical issue of VLBI schedules. In addition to network geometry which is calculated for observations, the hourly interval within the stacking approach supports a statistical count of parameter number of each epoch over the VLBI data set. This observation count demonstrates a decrease in the number of ERP residuals at around 19 hour of Coordinated Universal Time (UTC), cf. Figure 5.5. This loss of observations occurs presumably, when some of the stations take a break from regular sessions to participate in 1-hour intensive sessions from 18 UTC to 19 UTC (Behrend, 2013; Vandenberg, 1999a). For both, complete and reduced data sets, this fall in the number of VLBI observations represents approximately the same value.

5.2.4 The validation of the obtained empirical model

Empirical ocean tide models can be deduced in a stand-alone VLBI analysis (Gipson, 1996; Böhm *et al.*, 2012, b; Artz *et al.*, 2011) or in a combined solution of VLBI and GPS (Artz *et al.*, 2012). The current empirical solution is another solution purely based on VLBI observations. This newly-built model obtained by means of the first (standard) method of the TSA is validated using eight major tide term amplitudes (Figure 5.8) against the set of VLBI-based models provided by Artz *et al.* (2011), Böhm *et al.* (2012, b) and Gipson (1996, personal communica-
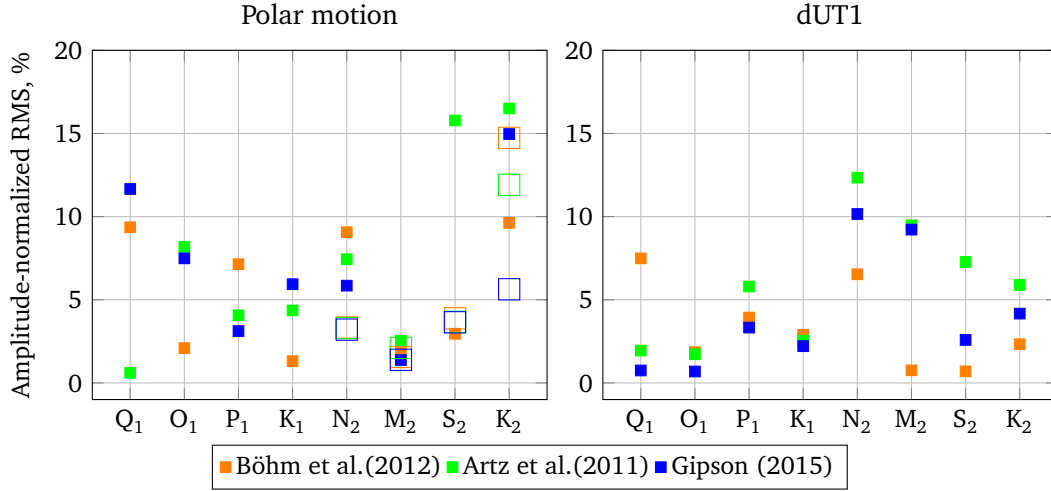
Figure 5.8: Previous VLBI-based solutions are compared against this thesis's results. The amplitude-normalized RMS differences for eight major ocean tides observed in polar motion are on the left side and dUT1 on the right. In polar motion unfilled squares indicate retrograde components of the semidiurnal tides. In polar motion the amplitude normalized RMS for S_2 tide attains 37.5% (off scale) with the solution by J. Gipson (2015).

tion, 2015). To quantify the resemblance between these models and the current solution, the amplitude-normalized root mean square (RMS) difference is used in percentage:

$$\Delta\text{RMS}_i \quad = \quad \sqrt{\frac{(|A_i^+|-|\hat{A}_i^+|)^2+(|B_i^+|-|\hat{B}_i^+|)^2}{(\hat{A}_i^+)^2+(\hat{B}_i^+)^2}} \cdot 100\%, \tag{5.18}$$

where the compared model data are marked by $\hat{A}_i^+$, $\hat{B}_i^+$, which coefficients are parameterized as given in equation (5.11) per tide term i. The amplitude-normalized RMS differences for the retrograde polar motion are calculated by equation (5.18) only for the four semidiurnal tides marked with unfilled squares (Figure 5.8). The devised algorithm evaluates simultaneously the diurnal band of the retrograde polar motion, and while the other models usually set these terms to zero to satisfy the Conventions requirement, there cannot be any crosscheck. In this thesis the amplitudes at those frequencies are assumed to exhibit no signals (Table B.1), because these values are under 3σ level and below the noise threshold. Consequently, the conventional separation of these signals by the virtue of CIP definition is introduced correctly.

Among these eight major tides, the largest amplitude of the principal lunar M_2 tide in the semidiurnal band and O_1, P_1 and K_1 tides in the diurnal band show a smaller scattering of values per constituent (Figure 5.8) comparably to the smaller amplitudes of the Q_1 and K_2 tides. A disagreement with these general trend can be recognized for the principal lunar semidiurnal M_2 tide in dUT1. The N_2 tide shows similar discrepancies in percentage, because this wave is smaller than the M_2 tide, it gives a rise to larger amplitude-normalized RMS differences in the prograde polar motion and dUT1. Another major tide in the same band is the principal solar S_2 tide, for
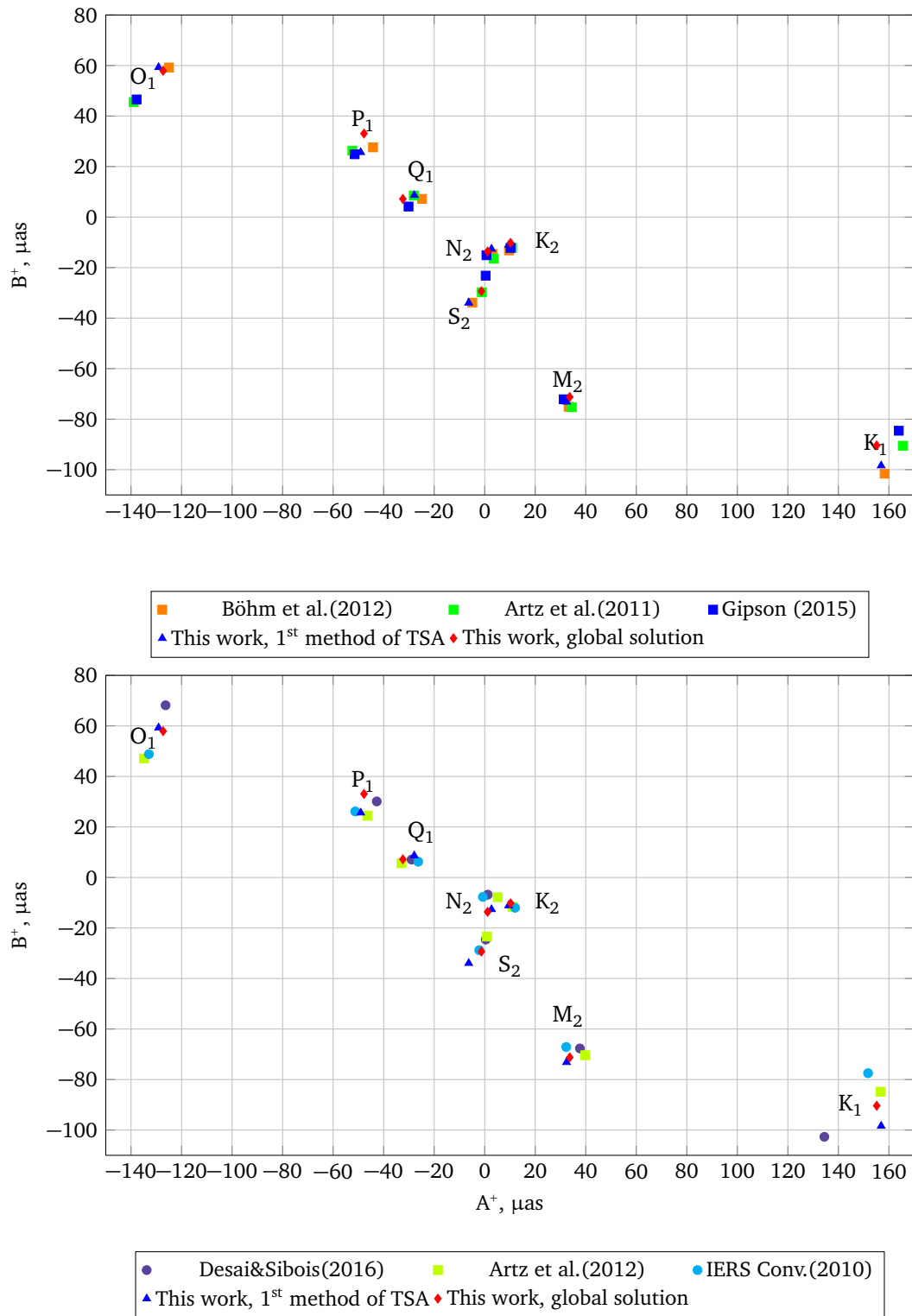
Figure 5.9: The prograde polar motion is shown for eight major tides from previous VLBI-based solutions (upper panel) and solutions based on the updated ocean model by Desai & Sibois (2016), the old model introduced in the IERS Conventional model (IERS Conv.) and the combined solution by Artz et al.(2012). Corresponding data from the first method of TSA and global solution in this work are added to both plots.
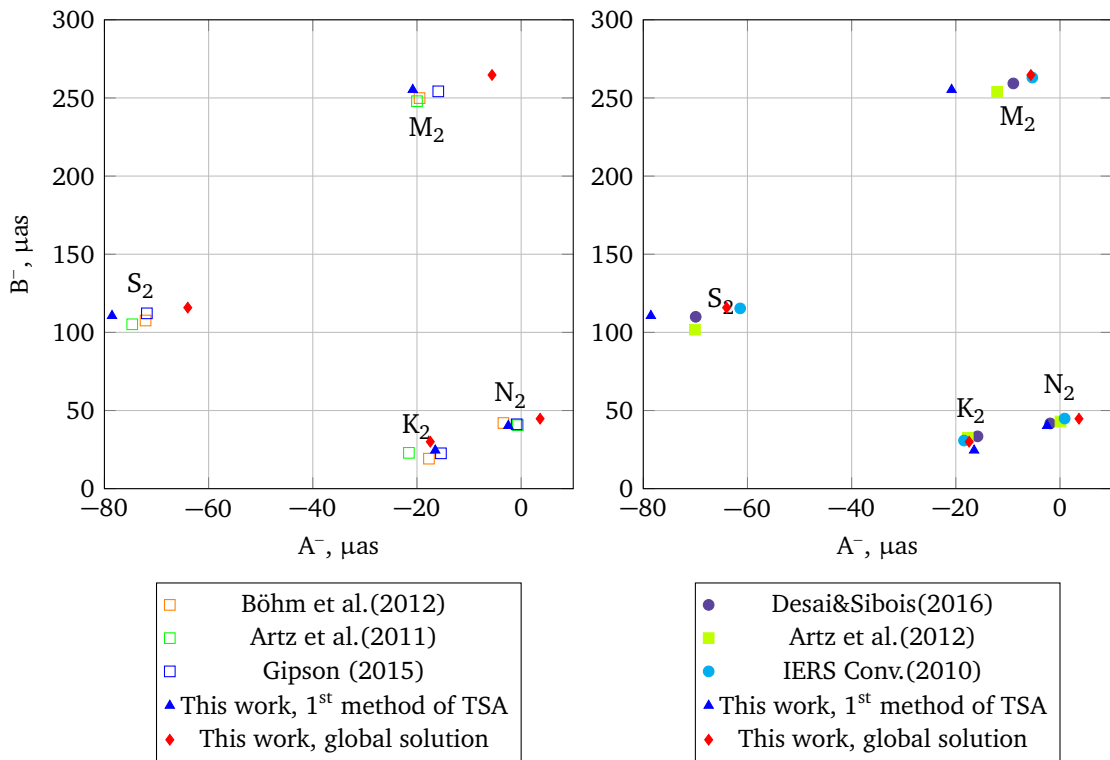
Figure 5.10: The retrograde polar motion is shown as in Figure 5.9.
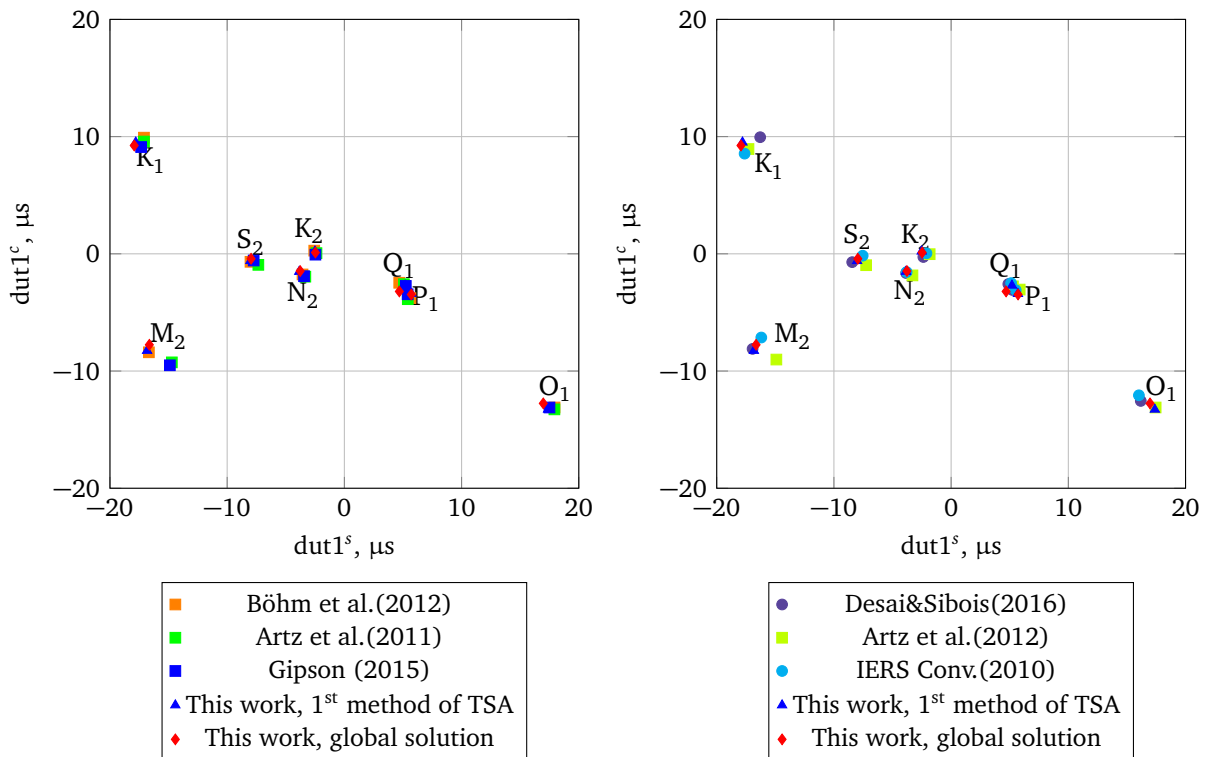
Figure 5.11: The dUT1 tide terms are shown as in Figure 5.9.

which the dUT1 result from J. Gipson's solution deviates insignificantly from the other solutions. In the prograde polar motion, however, the range of RMS differences for the S_2 tide is the widest (37.5%) based on the model by Gipson (1996), while values in the retrograde band are extremely close. In contrast, the remarkably small RMS differences among values of all models can be seen for other constituents in the semidiurnal retrograde band. An exception is found at the combined lunar-solar K_2 tide, which is similar to the N_2 or Q_1 tide case (smaller amplitudes), but with a wider RMS scatter.

The good agreement of the current evaluation with results from Böhm *et al.* (2012, b) are mainly evident in the semidiurnal band of dUT1 in Figure 5.8 possibly owing to the usage of the same VLBI software VieVS (Böhm *et al.*, 2012, a), while the solution by J. Gipson is obtained by a rather different package (Calc/Solve, https://lupus.gsfc.nasa.gov/software_calc_solve.htm). In fact, recent research on this topic of the software error propagation (Minttu *et al.*, 2016) reports small but for some cases critical statistical estimates. Specially, the weighted mean difference over 24 hour VLBI sessions were found on the level of -1.66 µs with a weighted root mean square (WRMS) scatter of 5.46 µs in UT1. At the same time, the largest obtained discrepancy in dUT1 ($\approx$10%) of the Artz *et al.* (2011) and Gipson (1996) models with Böhm *et al.* (2012, b) solution is approximately 1.5µs, thus variations of the amplitude-normalized RMS differences among solutions on this level are supposed to be insignificant. A complementary comparison for polar motion is unavailable, but a similar error propagation might be assumed. Overall, this comparison in Figure 5.8 indicates that the current assessment for the ocean tide terms is somewhat in between the models of Gipson (1996), Böhm *et al.* (2012, b) and Artz *et al.* (2011).

5.2.5 The S_1 tide in Earth Rotation

In this particular study the commonly accepted high-frequency IERS Conventional model (Petit & Luzum, 2010) is utilized as a reference for a new empirical tide model. This model was derived by an assimilation method (Egbert *et al.*, 1994) based on the analysis of the TOPEX/Poseidon global tidal model (TPXO) version 2 of satellite altimetry measurements and the ocean tidal angular momentum extended in the Arctic region (Ray *et al.*, 1997). The routines were built to produce the coefficients of the corresponding tidal terms (Model C) as presented by Chao *et al.* (1996). Eight major tide terms were shown to explain 60% of tide impact in polar motion variations derived from observations during Continuous VLBI (CONT)94 (VLBI campaign). For the tide tables in the IERS Conventions these routines and tide terms were provided by Eanes (Petit & Luzum, 2010). The tabulations at the S_1 frequency contain no atmospheric contribution, but a small gravitational part (Section 2.2.3), so that, when this model is introduced in the reductions, the correction obtained by means of TSA represents the atmospheric part explicitly.

An updated altimeter-dependent model (Egbert & Erofeeva, 2002, TPXO8) was implemented in a recent prediction model for diurnal and semidiurnal tides in the ERP (Desai & Sibois, 2016). The tide terms (Figure 5.9, 5.10, 5.11) were evaluated against GPS observations, where radi-

ational tides being not considered. In fact, the model by Desai & Sibois (2016) comes with a gravitational part at S_1 frequency (Figure 5.12 and 5.13). Similarly, Madzak *et al.* (2016) used satellite altimetry observations of ocean tides to improve the current IERS Conventional model. In particular, the S_2 tide exhibits a good agreement between model and ERP observations because altimeter data contain the combined effect of the ocean tide and ocean response at this frequency to the atmospheric forcing. The S_1 tide is still set to gravitational part only (Madzak *et al.*, 2016). Another empirical model (Artz *et al.*, 2012), which includes the GPS observations (Figure 5.9, 5.10, 5.11), confirms the recognized discrepancies in the diurnal band. This combined solution (Artz *et al.*, 2012) involves VLBI observations on the normal equation level in order to reduce the deficiency in the diurnal band. As result, the ERP tide terms model of this solution is close to that of Artz *et al.* (2011), however, estimates for the atmospheric tide appear to be even less accurate (Figure 5.12 and 5.13).

In view of the mismodeling of the atmospheric tides seen in the above studies, this thesis was devoted to the VLBI method advance. The first method of analyzing the high-frequency ERP time series have provided accurate results for the major ocean tides (Figure 5.8). Based on their reliability, the atmospheric S_1 tide was evaluated in the the second and third methods. The results displayed in Figure 5.3 exhibit a particularly close agreement for the first and the second method of TSA. The stacking approach results in a reduction of A^+ from 10 μas (in the standard approach) to 8.0 μas—a change that is only in a slight excess of the onefold standard deviation of any solution. Test calculations have shown that this small reduction arises from the inclusion of a 24-hour trend component in the fit of the stacked x and y components which has no analogue in the other TSA solutions. Such a trend over the duration of each session might have a physical explanation or not; nevertheless, the dependence of S_1 estimates on small details in the post-processing is illustrated. More general, it is not possible to identify one approach being "better" or more feasible than the others, thus the values of the third method of TSA are chosen to represent the assessment of the atmospheric S_1 tide in this work (Figure 5.12 and 5.13).

In this analysis the associated standard deviations σ as provided by stochastic modeling in equation (5.15) were found to vary barely across the set of coefficients A^+, B^+, A^-, B^- for each tide. The corresponding standard deviations are tabulated as tide-specific averages (Tables B.1 and B.3). The accepted $3\,\sigma$ level is 6 μas throughout and consistent with the largest zero tides (4 μas) that serve as separate measurements for the solution noise level. All retrograde diurnal polar motion coefficients fall below this threshold, suggesting that the signal content in this frequency band has been correctly attributed to nutation and the post-processing does not produce questionable signals in the retrograde band. For the S_1 in polar motion, both tide components (A^+ and $B^+ \approx 8$ μas) are significantly above the noise level, yet these estimates might still be affected by some systematic errors, e.g., due to various problems at individual stations or an uneven distribution of observations over the course of a 24 hour session and the entire time span. In an attempt to mitigate these influences and explore the stability of the S_1 results, other time series analysis strategies were tested.

In addition to the presented three methods of TSA, the global solution was applied to the same
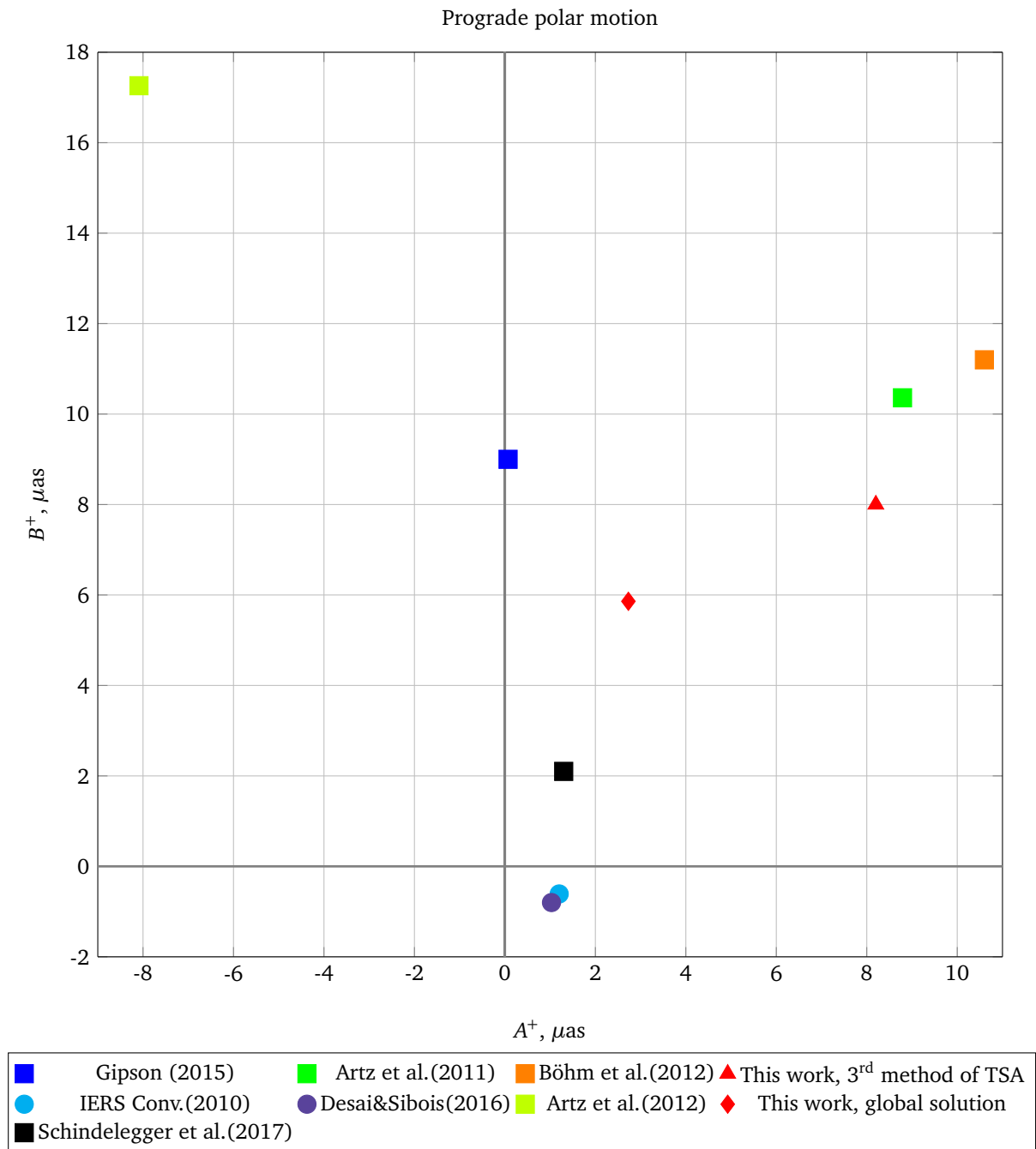
Figure 5.12: The atmospheric S$_1$ amplitudes in polar motion are obtained from VLBI analysis (Gipson (2015), Artz et al. (2011), Böhm et al. (2012)), the third method of TSA and global solution in this work, and the combined solution based on the VLBI and GPS observations (Artz et al. (2012)). The gravitational S$_1$ amplitudes in polar motion are provided by the IERS Conventions (2010) and Desai & Sibois (2016).

data set. The global solution for evaluation of tide terms is based on the principle of complex demodulation introduced by Böhm *et al.* (2012, b) and also implemented in VieVS (Böhm *et al.*, 2012, a). The results of this global adjustment are found to be in a good agreement with the
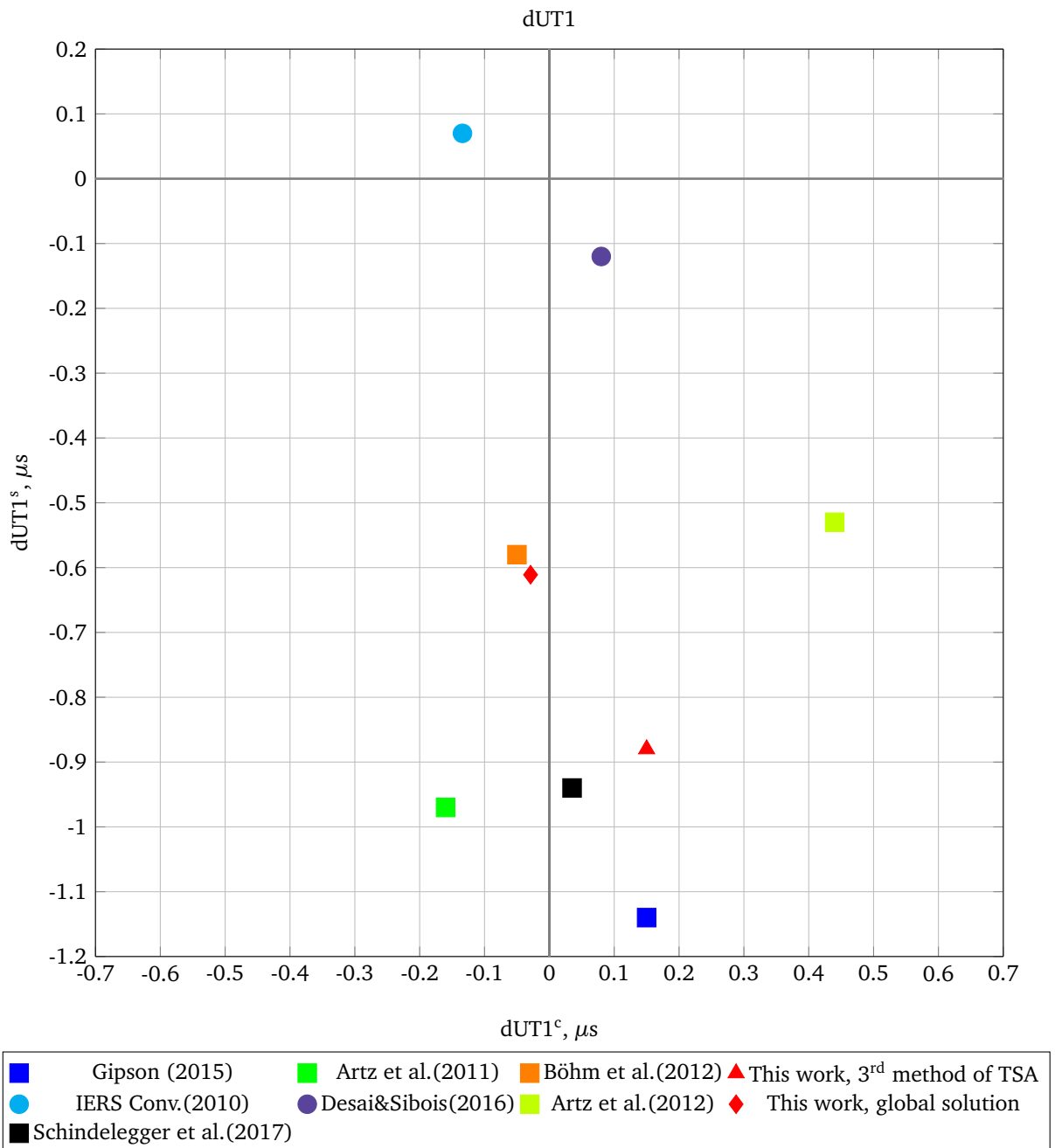
Figure 5.13: The atmospheric S_1 amplitudes in dUT1 are shown as in Figure 5.12.

estimates from third method of TSA in polar motion within $1 \div 2$ σ level and under 3 σ level in dUT1 (Figures 5.12 and 5.13). The Table B.3 contains the full data set of estimated tide terms in global solution as recommended by IERS Conventions, which is similar for the first method of the TSA in Table B.1. These two solutions performed in the global adjustment and standard TSA demonstrate a good agreement as it can be expected for the same data set and software.

Overall, the obtained results confirm the recognized discrepancy at the S_1 frequency between

the geodetic estimates (both VLBI-based solutions and combined solution with GPS) and geophysical models (Figure 5.12 and 5.13) in terms of the the polar motion (Girdiuk *et al.*, 2016a). The previous VLBI-based results in Figures 5.12 and 5.13 display the combined effect of the gravitational S_1 part, the radiational S_1 tide and hydrodynamic ocean response to the atmospheric forcing. The gravitational part can be easily subtracted by introducing corresponding signal in the time series variations, and the obtained results in this work, thus, represent the sum of the radiational part and the ocean response at the S_1 frequency. An independent estimate of the S_1 tide in polar motion was deduced by Schindelegger *et al.* (2017) from the atmospheric and oceanic angular momentum series. The amplitude depicted in Figure 5.12 is an average value based on computations from three modern atmospheric reanalyses (see for details Schindelegger *et al.*, 2017). The atmospheric S_1 tide from global adjustment is the closest value (within 5 μas) to this geophysical estimate. The S_1 perturbations in LOD were computed in a different approach by means of torque quantities and ocean angular momentum (Schindelegger *et al.*, 2017). These estimates exhibit a good agreement with VLBI-based results, especially with Artz *et al.* (2011) and the third method of TSA. The VLBI-based estimates still disagree with geophysical model values (Schindelegger *et al.*, 2017), because the deviations between these solutions are more than $3\,\sigma \approx 6$μas in polar motion and $3\,\sigma \approx 0.3$μs in dUT1 of formal errors, which supplies VLBI estimates. In comparison with previous assessment of the atmospheric tides from VLBI analysis (10 μas in polar motion, Girdiuk *et al.*, 2016b) the discrepancy was reduced to 5 μas.

5.3 Station positions time series analysis

The atmospheric tides in the hourly station position time series (Section 4.3.3) can be estimated by the LSA in the same manner as tide variations in the high-frequency ERP time series. The major difference is the parametrization matrix *A*, which in case of the station position analysis needs to include only the radiational S_1 and S_2 tides of the frequencies $\nu_{1,2} = 1, 2$ cpd as expressed by arguments

$$\alpha_i = \nu_i \cdot t + \varphi_i, i \in (1:2), \tag{5.19}$$

where phase lag is not introduced $\varphi_{1,2} = 0$. To evaluate atmospheric tides in station positions the corresponding modeled values were not added in the reductions. Thus, effects of atmospheric tides are included in the residuals of the hourly station position time series obtained from the single session solution. In fact, this approach deals with three time series of station positions in rectangular coordinates (X,Y,Z), which are transformed to (R,E,N) system to report atmospheric tides in format of cos- and sin-components of total amplitudes similar to the numerical models (see Section 3). With respect to the main intention (Section 4.3.3) to evaluate the atmospheric contribution, this approach examines the S_1 tide. An estimate at the S_2 frequency can not be related entirely to the atmospheric tide (see Section 4.3.2). Any mismodeling in the ocean loading

Solution	Atmospheric loading	Ocean loading	Delay model	Parametrization
1	-	+	VMF1	gradients estimated
2	-	+	VMF1	gradients fixed
3	-	+	Ray-tracing	gradients estimated
4	-	+	Ray-tracing	gradients fixed

Table 5.2: The differences in the reductions and the parametrization of the single session solutions are applied for the study of atmospheric effects in the harmonic variations of the station positions. Symbols "-" indicates that the atmospheric tidal loading is not included in the reductions, "+" signifies that the ocean tidal loading is introduced (FES2012 (MLP) model).

can be seen and misinterpreted therein as atmospheric part when the corresponding model is taken into account in reductions.

Since the recommended reduction for the tidal ocean loading FES2004 does not take into account the ocean response to the atmospheric forcing at the S_1 frequency, the updated version FES2012 (MLP) of the ocean model (Petrov, 2015) is implemented in the current analysis. Besides, an effort to assess this small response is undertaken. In accordance with this purpose, VLBI analyses are performed with the inclusion of the atmospheric tidal loading and exclusion of the ocean tidal loading. Equation (5.19) used for the evaluation of the eight major tide terms and S_1 tide in variations of the harmonic station positions demonstrates reliable assessment. Yet, the particular S_1 frequency requires a detailed discussion.

5.3.1 Atmospheric tides in harmonic variations of station positions

As discussed in Section 4.3.3 on the one hand, model values provided by TU Wien and GSFC represent an account for the atmospheric tidal loading and reveal a reasonable agreement for the amplitude and phase at the chosen stations (Figure 5.14). On the other hand, atmospheric tides computed for two stations, Katherine and Westford, are compared against numerical models (Figure 5.14). The differences among the estimated components exhibit an insignificant amplitude scatter (under 3 σ level). Their phases indicate the moment of the atmospheric tidal loading maximum, and a typical phase lead is 8 hours for Katherine and 6 hours for Westford. Since the empirical approach deals with the observed variations, which are overwhelmed by a number of deficiencies similar to the ERP time series, the phase is unavoidable issue. And, because all obtained amplitudes are less than the 3 σ level for Katherine or close to this level, this assessment can not be reliable entirely for this particular station. In this case, the phase problem is not decisive issue. In contrast to Katherine, significant amplitudes are detected for Westford. The station Westford was chosen to accomplish the atmospheric tidal loading study; however these exaggerated results (Figure 5.14) find a different argument.

The physics of daily insolation can be suspected to be involved in the miscalculation at the S_1 frequency. Because the physical processes of heating can contaminate measurements significantly (Ray & Egbert, 2004) it is an unavoidable problem, especially, when atmospheric tides are the subject of evaluation. In the VLBI analysis, this process is taken into account by thermal antenna
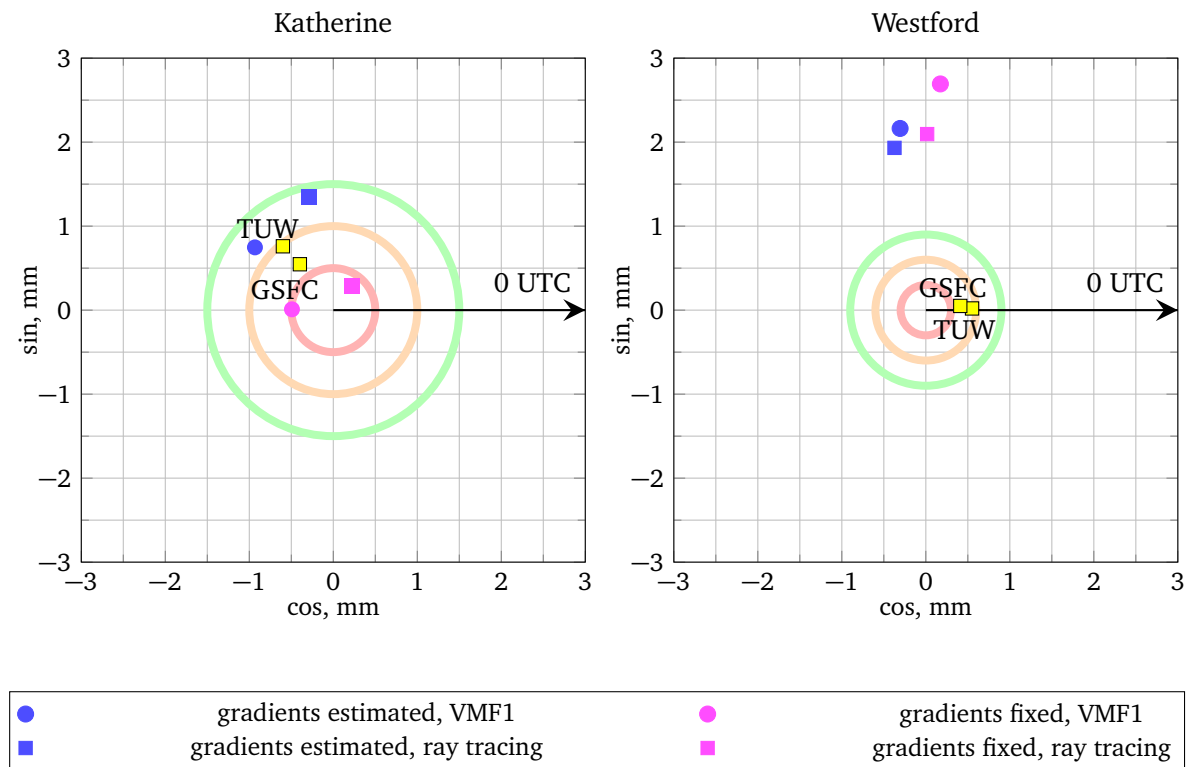
Figure 5.14: Atmospheric S_1 tide is retrieved in radial component variations of station positions for Katherine (on the left side) and Westford (on the right side) as obtained from single session solutions (Table 5.2). The basic set of reductions includes the high-frequency Conventional model. The total amplitudes are represented by cos- and sin-components. The solutions, in which ray-traced delays are applied, are marked with squares, VMF1 with circles, pink color denote solutions where gradients are fixed, blue where gradients are estimated. The 1 σ level of standard deviations is depicted on both planes as circle of pink color, 2 σ of orange color, 3 σ of green color. The phase reference is Greenwich midnight (0 UTC).

deformation in the reductions. To explore the sensitivity to this effect, the solutions, in which the thermal antenna deformation model is discarded, were undertaken (Figure 5.15). With respect to Figure 5.14 the total amplitudes deviate by 0.2-0.7 mm at station Westford. The phase scatter of these solutions is about 4 hours for Katherine and 2 hours for Westford. A less disturbed scatter at the station Westford can be also explained by the fact that antenna 18.3 m in diameter in Westford has a 28 m radome to protect the dish from the environment. In view of the small size of the Katherine dish (12 m) the deformations are expected to be smaller and better predicted, thus this antenna is supposed to have no need for the radome. Yet, this wide scatter might indicate an influence of nonlinear effects of the dish.

The station position estimates by means of the single session solution can be improved by the data set expanding. Further observations provided in intensive scheduling (as it had been done during last couple years until the current moment for Katherine) should advance these results. For instance, the consideration of the second example station Westford can justify a better accuracy in terms of standard deviations. The 1 σ standard deviation is approximately on 40 % smaller for station Westford than for station Katherine. This difference mostly can be traced back to the
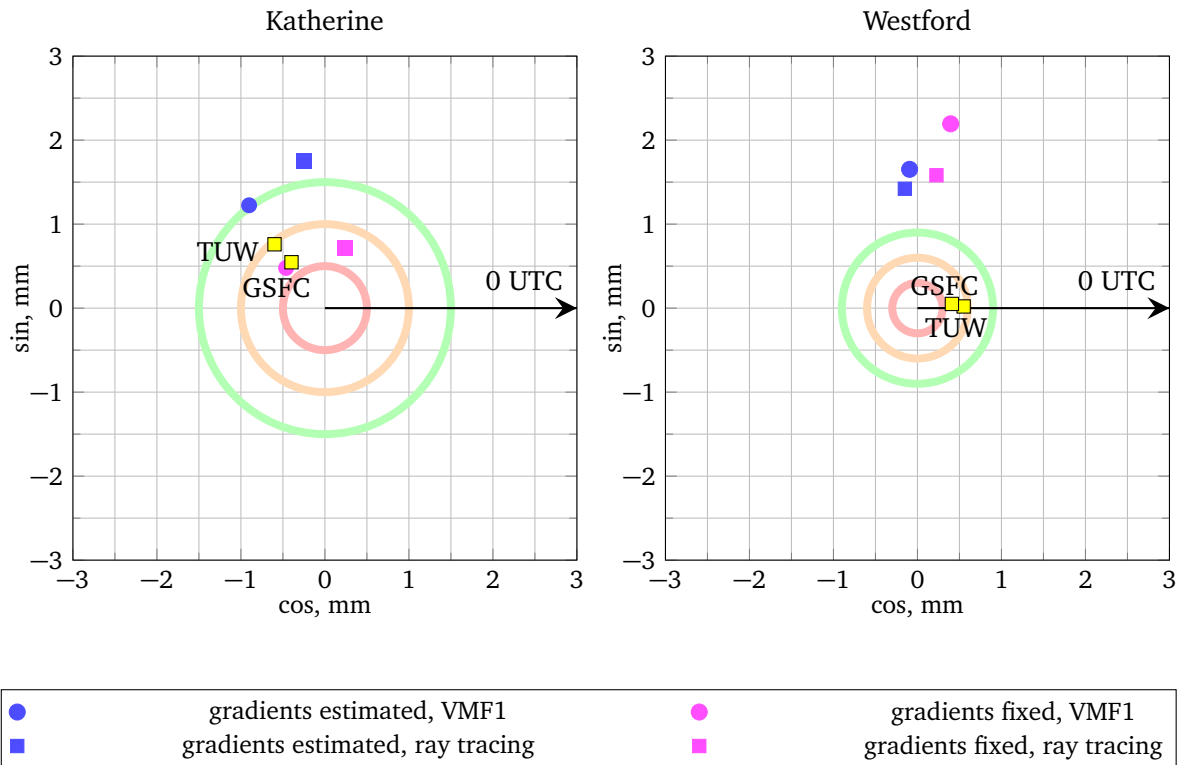
Figure 5.15: Atmospheric S_1 tide is shown as in Figure 5.14 but disregarding the thermal antenna deformation.

Ratio	Westford, %	Katherine, %	absolute values	Westford, mm	Katherine, mm
$\frac{S_1}{P_1}$	62	49	P_1	1.5	1.9
$\frac{S_1}{K_1}$	19	16	K_1	5.0	5.9

Table 5.3: Relative and absolute S_1 tidal term amplitudes with respect to the P_1 and K_1 tides for stations Westford and Katherine as provided by FES2012 (MLP).

length of time series for station Westford, which is about 20 years long in comparison with 5 years for Katherine. Katherine was built as a part of Australian network about 10 years ago, and it is a relatively new station in the VLBI network. In contrast to Katherine, the first radio observations at Westford were started in 1962, joining the VLBI network in 1981. Hence, this station is more reliable in terms of stability defined for ground-based observatories due to the length of continuous observations.

The total amplitude estimates at station Westford for all solutions in Figure 5.14 disclose a sizable discrepancy with atmospheric model values. Given the data set reliability for station Westford, this problem cannot be explained in a straight-forward manner, because the analysis of the time series at the station Westford was expected to reveal no signal. These obtained variations
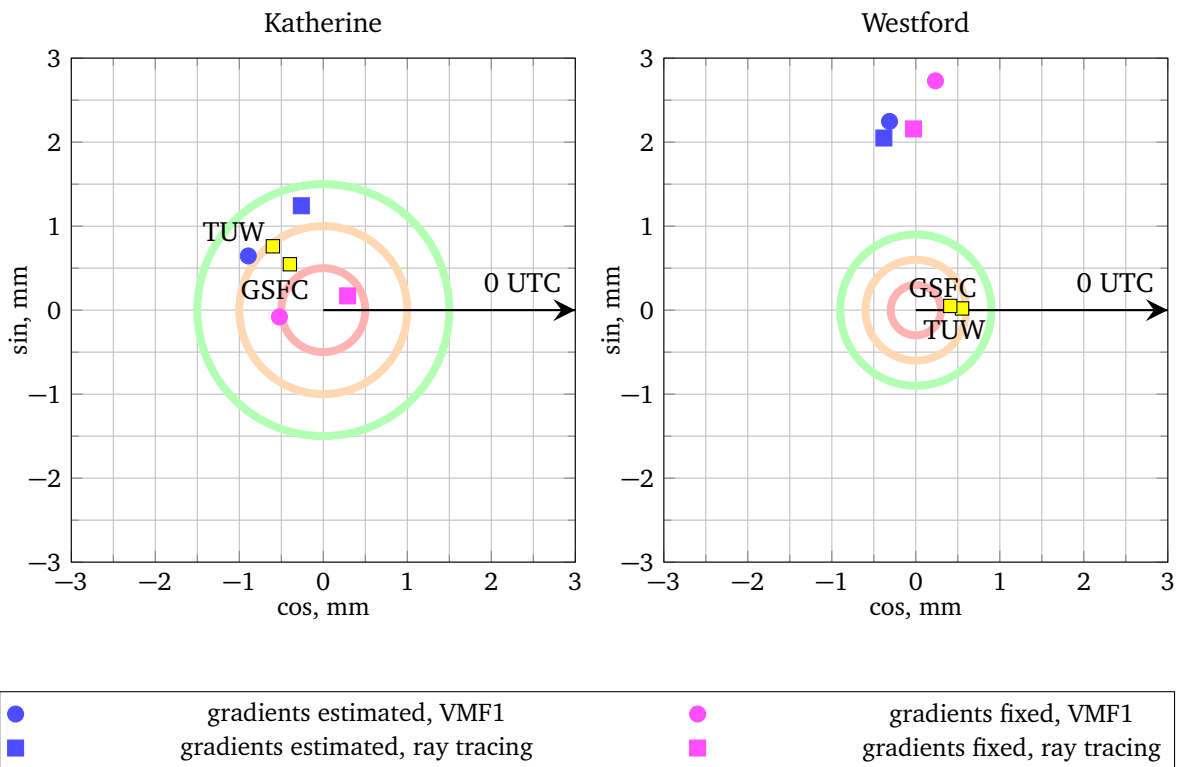
Figure 5.16: Atmospheric S_1 tide is shown as in Figure 5.14 but the high-frequency conventional model replaced by the model of Madzak *et al.* (2016).

can arise from the applied method of the LSA at the predefined frequencies because of possible leakage from side lobes. The closest frequencies containing the larger ocean loading tides P_1 and K_1 can corrupt the atmospheric loading S_1 signal, and thus the results in Figure 5.14 might present this complex effect instead of the tidal loading amplitude at the S_1 frequency. The ratio of modeled amplitudes for these tides are collected in Table 5.3, where the same tidal amplitudes for the station Katherine are shown for the comparison. Moreover, the signal measured at the S_1 frequency represents a complicated combination by itself consisted of the gravitational part, radiational tide and hydrodynamic ocean response to the atmospheric forcing. The gravitationally induced S_1 constituent is a product of the P_1 and K_1 side lobes as derived from the tide generating potential (TGP). This tide is not included in the current set of reductions since models neglect its small impact. In fact, the obtained estimates in Figure 5.14 demonstrate the total effect of the atmospheric S_1 tide composed by the radiational part and hydrodynamic ocean response.

To further test the obtained station position variations, two types of models described in the Section 4.3.3, the ray-tracing and standard approach (VMF1) were varied. As follows, four combinations were generated (Table 5.2), where gradients are fixed to the a priori values in the single session solution parametrization and where gradient estimates are included in the parametrization matrix as usual. A possible improvement of the assessment by means of ray-traced delays and gradients fixed to this a priori model was expected. The insignificant deviations between

Solution	Atmospheric loading	Ocean loading	Delay model	Parametrization
1	+	-	VMF1	gradients estimated
2	+	-	VMF1	gradients fixed
3	+	-	Ray-tracing	gradients estimated
4	+	-	Ray-tracing	gradients fixed

Table 5.4: The differences in the reductions and the parametrization of the single session solutions are applied for the study of atmospheric effects in the harmonic variations of the station positions. Symbols "+" indicates that the atmospheric tidal loading is not included in the reductions (TU Wien model), "-" signifies that the ocean tidal loading is not introduced

these solutions, however, cannot point to any of these strategies as more reliable.

The dependence on the high-frequency ocean model is explored by changing the a priori high-frequency tide model in the reductions. For this purpose, the recently developed model by Madzak *et al.* (2016) is chosen because this updated solution is based on modern ocean model. Still the obtained estimates of the S_1 tide in Figure 5.16 exhibit no statistically significant deviations. A similar dependence was investigated by changing the underlying ocean and atmospheric loadings (Section 4.3.2) to find any deviations in the obtained high-frequency tide terms (Girdiuk *et al.*, 2016a). In overall, both methods to study these dependencies are not able to provide definitive conclusions, thus underlining a possible limitation of the VLBI method.

5.3.2 Ocean tides in harmonic variations of station positions

The importance of the daily and sub-daily oceanic impact was already presented in the Section 4.3.2 for the joint analysis of the atmospheric tides. The atmospheric tidal term analysis in harmonic variations of station positions indicated a possibility to assess this kind of variations. The main problematic issues of this approach are small amplitudes at the chosen frequency (S_1) and the leakage effect of the major ocean tides alongside (P_1 and K_1). Since S_1 tide leads to an ambiguous assessment, the reliability of the presented estimation approach needs to be exemplified by inspecting other tidal terms. The major ocean tides P_1 and K_1, which tower above in the diurnal band, are suited for this evaluation.

The same approach of the LSA at pre-defined tidal frequencies introduced in the previous section is extended by the eight ocean tides $i \in (1:8)$ modeled in accordance with their frequencies ν_i and phases φ_i of the equilibrium tide (HW95 catalogue) based on Doodson numbers (see Appendix A):

$$\alpha_i = \nu_i \cdot t + \varphi_i, i \in (1:9), \tag{5.20}$$

where $i = 9$ is for the radiational S_1 part.

To deduce ocean tides in the variations of the station positions from the single session solution of the same sessions (as for atmospheric tidal loading analysis), the set of implemented reductions
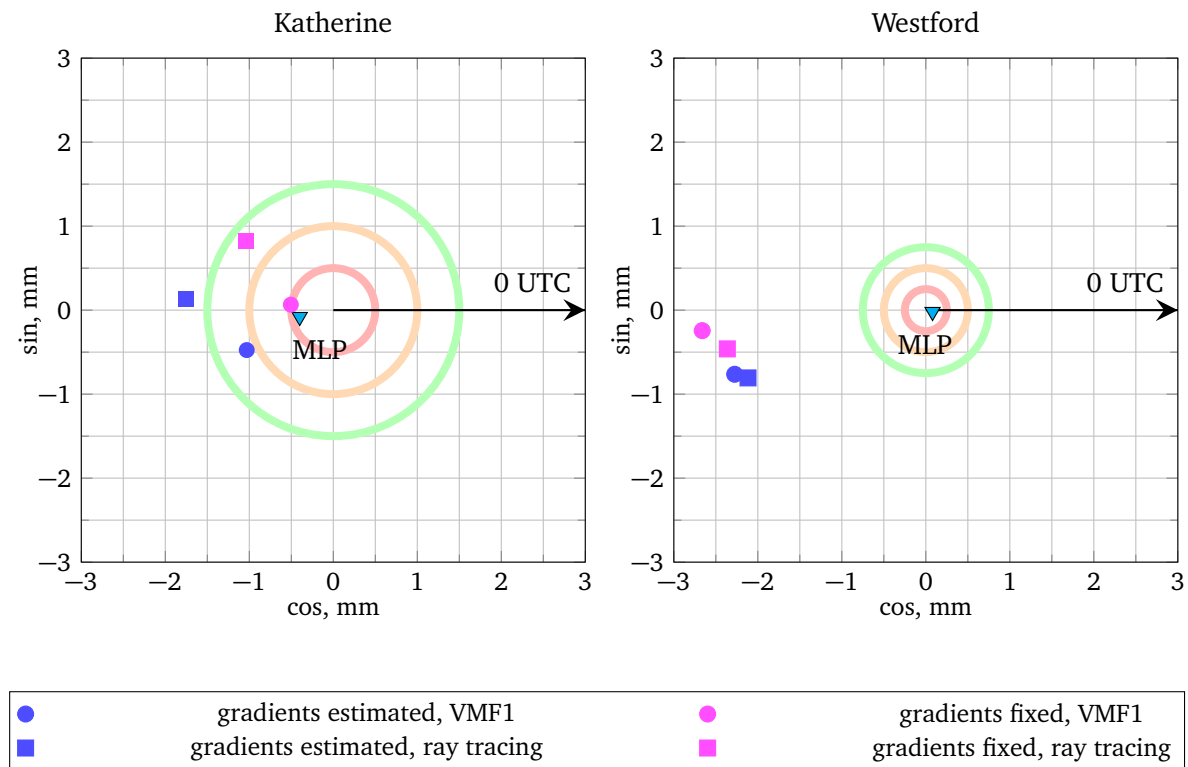
Figure 5.17: Ocean response to the atmospheric forcing of S_1 frequency is retrieved in radial component variations of station positions (Katherine and Westford, also see Table 5.4). The basic set of reductions includes the high-frequency Conventional model. The total amplitudes are represented by cos- and sin-components. The solutions, in which ray-traced delays are applied, are marked with squares, VMF1 with circles, pink color denote solutions where gradients are fixed, blue where gradients are estimated. The $1\,\sigma$ level of standard deviations is depicted on both planes as circle of pink color, $2\,\sigma$ of orange color, $3\,\sigma$ of green color. The phase reference is Greenwich midnight (0 UTC). MLP signifies FES2012 ocean model provided by Petrov (2015).

needs to be modified appropriately (Table 5.4). The complete set of 11 ocean tides, which is the recommended standard by the IERS Convention to apply, is eliminated entirely for the station Katherine (or Westford) only. The current study can be exempted from three long-term tides because their account is expected to be irrelevant in the diurnal and semidiurnal bands.

Concerning the S_1 tide in this thesis, the atmospheric contribution is taken into account in the reductions at the single session solution (Table 5.4), so the signal at the S_1 frequency should contain the ocean response to the atmospheric forcing. The results of the LSA are depicted in Figure 5.17, in which the methods for treating the tropospheric impact were varied. The amplitude scatter shows a close similarity with the results of the atmospheric tides (Figure 5.14). Any deviations between particular solutions (fixed gradients to the ray-traced delays) can not be considered as reliable because these values are within $3\,\sigma$ level. The discrepancies of estimated and modeled values are sizable for Katherine and, especially, for Westford (Figure 5.17). The model value marked as MLP stems from the calculations of corrections to the station positions by Petrov (2015) for FES2012 model. At S_1 frequency, Petrov (2015) introduces a 90° phase lag. To be con-
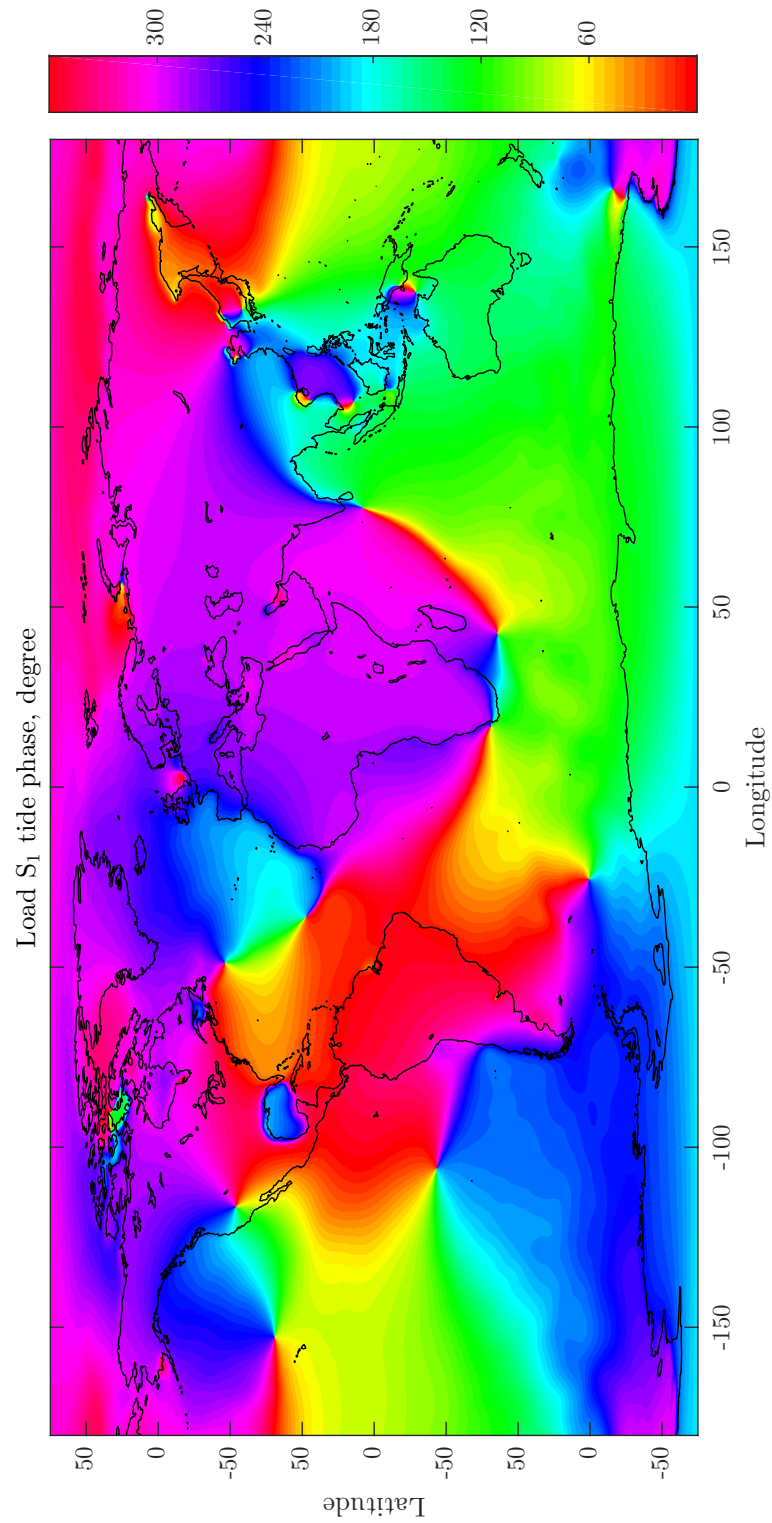
Figure 5.18: The phase lags (degree) for the load tide associated with the ocean response at the S_1 frequency as provided by FES2014 ocean model is shown.
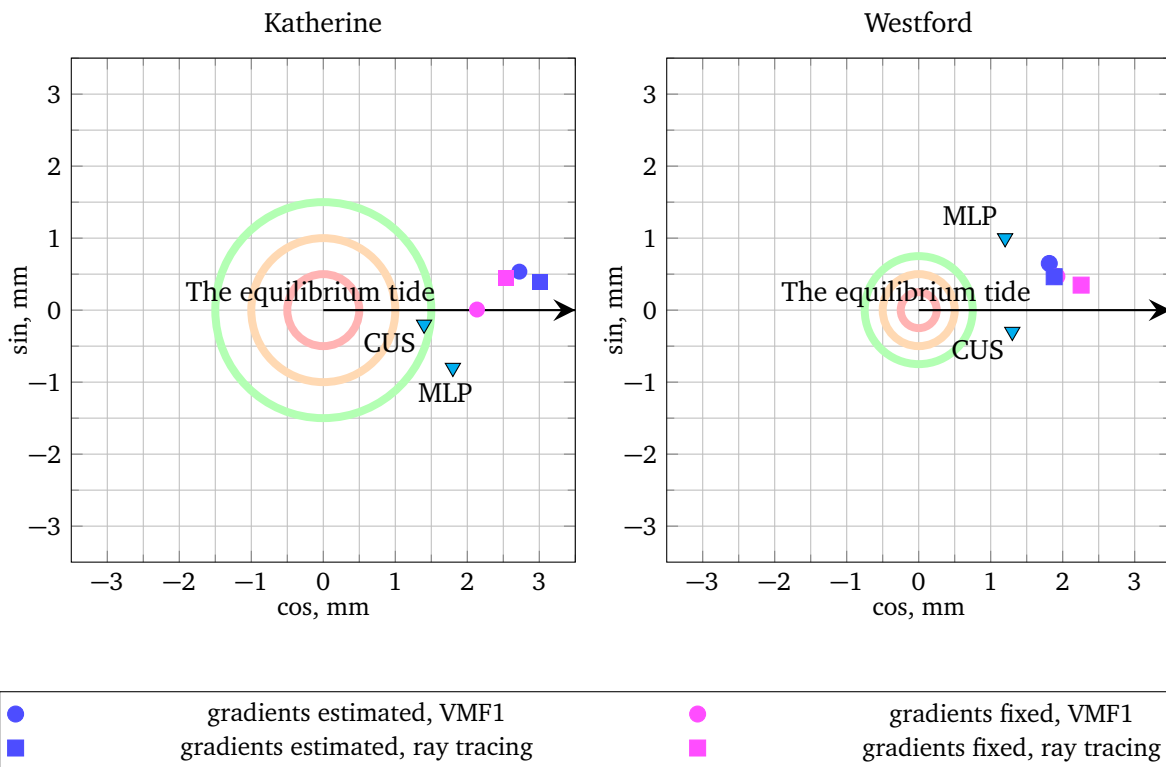
Figure 5.19: P_1 ocean tide is shown as in Figure 5.17. CUS stands for FES2012 ocean model provided by Bos & Scherneck (2007).

sistent with this model values, the same phase lag was added to the argument at the S_1 frequency in the current parametrization in Figure 5.17. A close agreement by phase can be seen for the results at Katherine (Figure 5.17), which is still broader than for Westford. This service (Petrov, 2015) is only one which provides S_1 tide for operational analysis, thus for the comparison the load tide at the S_1 frequency is represented in Figure 4.11 by the FES2014b model (Lyard *et al.*, 2014). The amplitude of the S_1 from the FES2014b model is rather similar to the MLP value. The phase in Figure 5.18, which demonstrates the phase of S_1 tide provided by the FES2014b model, mirrors values for Katherine ($\approx 180°$) and Westford ($\approx 0°$).

The station position variations at the frequencies of the P_1 and the K_1 tides are illustrated in Figures 5.19 and 5.20 correspondingly. The modeled values for these major tides are taken for two providers of the station corrections (CUS by Bos & Scherneck (2007) and MLP by Petrov (2015)) derived from the same ocean model (FES2012, Lyard *et al.*, 2006). The amplitudes show a reasonable agreement with both model values (MLP and CUS). These obtained estimates deviate within 1 mm from each other, which might serve as an explanation for the discrepancy registered at the station Westford in the analysis of the atmospheric S_1 tide. The phase discrepancy between particular solution up to 3 hours is acceptable since the scattering of the obtained solutions is less broad than the difference between model values of two providers. The set of four solutions (Table 5.4) is shown in each plot, where no specific solution can be noticed because the two
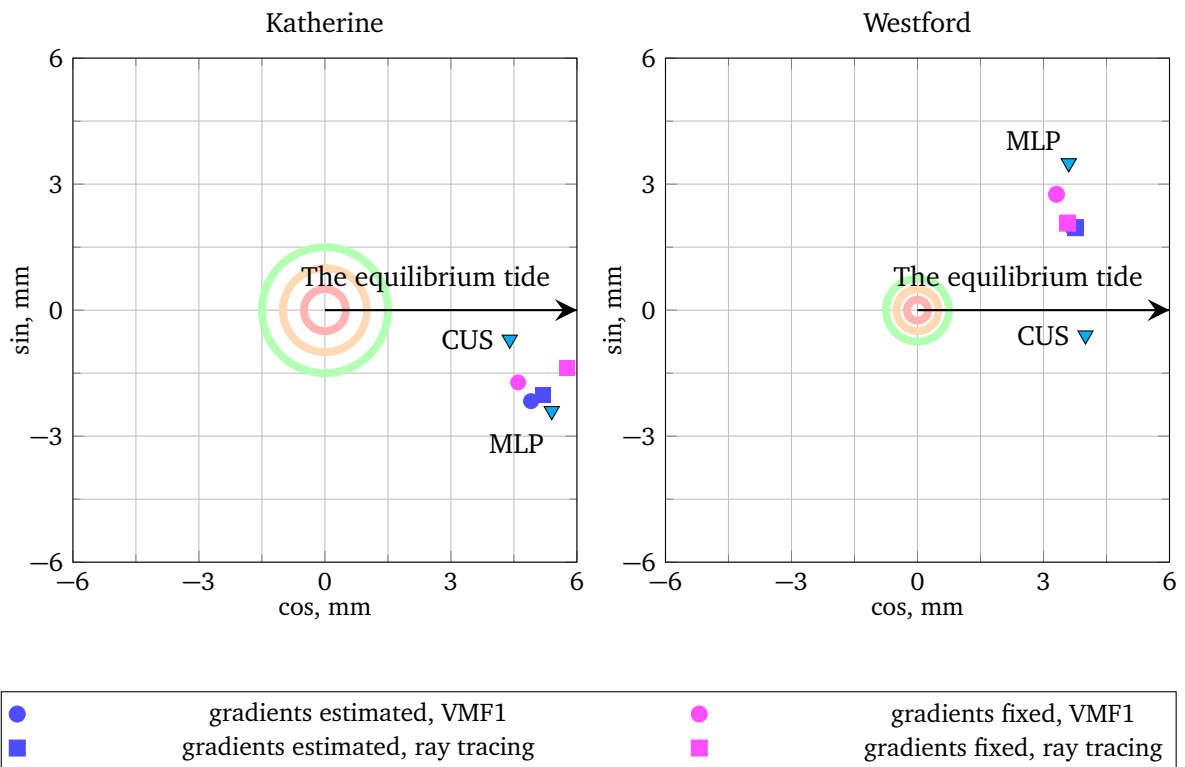
Figure 5.20: K_1 ocean tide is shown as in Figure 5.19.

model values deviate significantly. However, the remarkable agreement among these four VLBI solutions is evident.

Chapter 6

Conclusion

In recent years geodetic VLBI analysis has made progress to detect the smallest tide signals in the high-frequency Earth's rotation variations. The thesis's emphasis has been placed on the recognized anomalies in the high-frequency band, namely the atmospheric S_1 tide. Unlike the major ocean tides, which are forced by the lunar-solar gravitation potential, the excitation source of radiational tides is continuous insolation of the atmosphere. Besides the effect of direct solar heating, the atmosphere incites motions in the oceans at the same frequencies. This hydrodynamic response to the atmospheric forcing can be estimated by the use of ocean model with atmospheric forcing on its surface, where the ocean angular momentum may be computed consistently with the atmospheric angular momentum. Corresponding regular variations occur in the diurnal and semidiurnal bands of the polar motion and LOD with periods of 24 hours (S_1) and 12 hours (S_2). These geophysical model estimates can be compared by a high-frequency empirical model derived from geodetic VLBI analysis, sensing tides as the combination of the atmospheric variations and the hydrodynamic response to the atmospheric forcing with the gravitational tides taken into account in the applied reductions. Contrary to S_1, the semidiurnal atmospheric S_2 tide cannot be evaluated by the geodetic methods yet, mainly owing to the strong gravitational forcing at this frequency and possible mismodeling in the separation of the different excitation sources.

Determination of the atmospheric tide effects in Earth's rotation may be intrinsically linked to the station displacement variations at the very same frequencies. Atmosphere and oceans envelope the Earth and, thus, contribute to the variations of the Earth's body shape directly. The geodetic VLBI stations located on the crust undergo the corresponding tidal loading deformations, which have been independently estimated in this thesis to study the impact of these atmospheric and ocean tidal loading models. Despite all efforts, the obtained variations were found insufficient to draw a definitive picture of tidal loading model performances mainly due to the existing limitation of the VLBI analysis in the determination of both the high-frequency tide terms and station positions.

The last 20 years of VLBI observations (1995-2015) were sifted, reviewed and reprocessed to facilitate the computation of the atmospheric S_1 tide estimates in the high-frequency Earth's rotation and the station positions. Half of the available VLBI data were removed in this revision

without a recession of the high-frequency tide term accuracy in comparison to the last similar evaluation by Böhm (2012). A stacking of the VLBI single session solutions is used to compose the time series of the high-frequency ERP as well as station position estimates. The obtained length of the time series is considered appropriate for an accurate evaluation of the smallest tides, because the long-term modulations are represented by at least one full period, except for the argument of period 20 940 years included at the S_1 tide. Since this constituent can be obtained from independent models, the gravitational S_1 account is assumed to be subtracted correctly. The radiational S_1 tide follows the Sun, thus the assembled ERP and station position time series include an acceptable number of approximately 20 years (5 years for Katherine only).

6.1 The atmospheric S_1 tide in the high-frequency ERP time series

The obtained high-frequency ERP time series variations are considerably accurate for purposes of small tide determination. The fitted empirical model was found to be in the good agreement with the previous VLBI solutions (Gipson, 1996; Artz *et al.*, 2011; Böhm *et al.*, 2012, b), a combined solution of VLBI and GPS observations (Artz *et al.*, 2012) as well as an altimetry-based tide ERP model (Desai & Sibois, 2016). The noteworthy fact is that all these geodetic results include the gravitational S_1 part and atmospheric S_1 tide. The altimetry-dependent ocean models, which also the high-frequency Conventional model, specify the amplitude at the S_1 frequency by the gravitational part only. In contrast, the current assessment implements the high-frequency Conventional model in the reductions and reports finally the the atmospheric S_1 tide amplitude. As geophysical model values (Schindelegger *et al.*, 2017) represent the atmospheric S_1 tide, the validation of the VLBI results is rigorous.

In this thesis, first of all, the ocean tide effects in the high-frequency ERP time series and their reliability were assessed, and, secondly, based on the obtained ocean tide terms, the atmospheric tides were pinpointed in the residuals at the corresponding frequencies. In the processing of the high-frequency ERP time series the atmospheric S_1 tide was evaluated by means of three methods of the time series approach. These methods were undertaken in order to reduce noises in the available time series, yet differences among these estimates are on the one-fold level of the standard deviations, which might not be significant. Additionally, the atmospheric S_1 tide along with the diurnal and semidiurnal tide terms was obtained in a global solution, which reduces the time series imperfections by averaging over the whole observed time span. Still, the differences between the S_1 estimates from the global solution and the time series approaches are approximately on the threefold formal error level. The atmospheric S_1 tide in polar motion obtained by means of the global solution was shown to be closer to the corresponding estimate provided by geophysical modeling (Schindelegger *et al.*, 2017) than the values derived from the time series approaches. And dUT1 estimates from the time series approaches were represented in a better agreement with geophysical modeling (Schindelegger *et al.*, 2017) than the global solution result. Specifically, the difference was reduced to 5 μas in polar motion, yet the retained deviation

is still significant. Previously published high-frequency ERP models based on geodetic techniques (Gipson, 1996; Artz *et al.*, 2011; Böhm *et al.*, 2012, b) achieved the discrepancies in polar motion in the order of 10 µas or larger (Girdiuk *et al.*, 2016b), especially when the signal at the S_1 frequency had not attributed correctly to the excitation source.

6.2 The diurnal and semidiurnal atmospheric tides in the station position variations

The station positions were evaluated using different sets of geophysical models in reductions to allow for a distinction of the impact of applying atmospheric and ocean models. Implementation of the corresponding corrections instead of a loading-free solution demonstrates the substantial improvement of the geodetic station position estimates by means of the baseline length repeatability. Yet, at the current stage of the geodetic VLBI observations, no distinction could be made among particular atmospheric and ocean loading models regarding their reliability on the longer time scales and daily and sub-daily periodicities.

A similar exploration was made in the supplementary study of the VLBI station position variations forced by the diurnal and semidiurnal atmospheric tides. The station position estimates were processed to detect atmospheric signals at the pre-defined radiational frequencies. Also, larger ocean tide signals were obtained by the same approach to confirm this assessment. The undertaken analysis utilized a straight-forward estimation where tide terms are not constrained unlike in previous efforts (Petrov & Ma, 2003). The comparison of the atmospheric tide amplitudes at particular VLBI stations, for instance, station Katherine, where the maximum of the atmospheric field forcing is achieved, revealed amplitudes on the same level as those suggested by numerical models. However, the threefold formal errors are still as large or larger than the displacement signal, therefore limiting the reliability of this assessment and emphasizing that the geodetic VLBI observations require a certain improvement.

6.3 Remark on the VLBI method

This thesis underlines certain limitations, in view of which the VLBI technique cannot serve as the precise standalone method for evaluation of signals in the Earth system. The particular and challenging test cases adopted in the present work are the atmospheric tide effects in the high-frequency ERP time series and in the station position variations. At least the quality assessment of these effects was accomplished, where the applied analysis for both time series is advanced by the straight-forward manner. This manner does not necessitate any additional constraints and incorporation of external geophysical models into the parameter limitation. The reliability of the applied approaches is confirmed by the obtained ocean tide terms which are in good agreement with other models in both time series, the high-frequency ERP and station position variations

Overall, the geodetic VLBI method is credited for the high accuracy of the IERS main products,

that is, the terrestrial and celestial reference frame and EOP time series. Recently, the small geophysical effects of ocean tides in the high-frequency ERP time series were determined on the substantial formal error level (Böhm, 2012). The present thesis was intended to expend this result by the accurate assessment of the even smaller geophysical effects associated with the atmospheric tides. Achieving consistency with the geophysical model results (Schindelegger, 2014; Schindelegger *et al.*, 2016, 2017) was a prime target. The most deterrent factor on the road to precise parameter determination, as undertaken in the present analysis, is the formal error level, even though the parameter estimates were obtained on the expected level from reference studies. Thus, this thesis encourages future work, in particular, repeat of the analysis when longer and more dense VLBI time series become available to improve the formal error level and reduce uncertainties.

Appendix A

Auxiliary calculations

Legendre polynomials

The central angle ψ between $(\vec{r}, \phi, \lambda)$ and $(\vec{r'}, \delta, \lambda')$ is defined (Beutler *et al.*, 2006; Simon *et al.*, 2013) on the sphere as

$$\cos\psi = \sin\phi \sin\delta + \cos\phi \cos\delta \cos(\lambda - \lambda'). \tag{A.1}$$

Analytical expression for Legendre polynomials (Hobson, 1931) to which angle ψ is substituted can be presented by the recursion formula (in which n can take value $n \geqslant 1$)

$$P_{n+1}(x) = \frac{2n+1}{n+1} x P_n(x) - \frac{n}{n+1} P_{n-1}(x), \tag{A.2}$$

where first terms are

$$P_0(x) = 1, \quad P_1(x) = x, P_2(x) = \frac{1}{2}(3\cos^2 x - 1), \quad \text{for every } x. \tag{A.3}$$

Legendre polynomials $P_n(\cos\psi)$ can be calculated using the Legendre addition theorem (Hobson, 1931)

$$P_n(\cos\psi) = P_n(\sin\phi)P_n(\sin\delta) + 2\sum_{k=1}^{n} \frac{(n-k)!}{(n+k)!} P_n^k(\sin\phi) P_n^k(\sin\delta) \cos[k(\lambda - \lambda')] \tag{A.4}$$

where P_n^k are the associated Legendre polynomials. Using spherical harmonics functions instead of the Cartesian approach, one introduces $Y_n^k(\phi, \lambda)$ for which the complex conjugation is
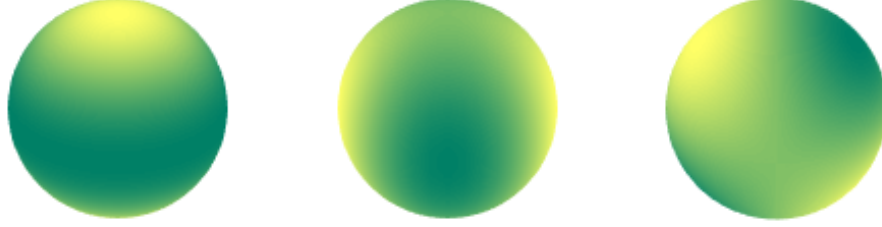
Figure A.1: Spherical harmonics: zonal, sectoral, tesseral.

defined as $Y_n^{k*} = (-1)^n Y_n^k$

$$Y_n^k(\phi, \lambda) = \sqrt{\frac{(2k+1)(n-k)!}{4\pi(n+k)!}} P_n^k(\cos\phi)[A_{nk}\cos k\lambda + B_{nk}\sin k\lambda], \tag{A.5}$$

A_{nk} and B_{nk} are constant coefficients, so that Legendre polynomials $P_n(cos\psi)$ take into account $\cos[k(\lambda' - \lambda)] = \cos k\lambda \cos k\lambda' + \sin k\lambda \sin k\lambda'$, leading to

$$V_{TGP} = \frac{GM}{L} \sum_{n=2}^{\infty} \left(\frac{R_\oplus}{L}\right)^n \frac{4\pi}{2n+1} \sum_{k=-n}^{n} Y_n^k(\phi, \lambda) Y_n^{k*}(\phi', \lambda'). \tag{A.6}$$

The Laplace spherical harmonics $Y_n^k(\phi, \lambda)$ can be visualized in Figure A.1. Specially, the graphical presentation of spherical harmonics reduces to finding the roots of $Y_n^k(\phi, \lambda)$. Three groups of solutions are defined as zonal, sectoral and tesseral harmonics (Hobson, 1931). Zonal harmonics appear in case $k = 0$ and provide locus parallel to equator of the sphere. Sectoral harmonics $n = |k|$ divide the sphere into pieces from one pole to another. The last group are tesseral harmonics on the sphere. A combination of the above-mentioned solutions, forming a chess-board (Beutler *et al.*, 2006).

Lunar-solar fundamental arguments

Variables referred to the fundamental epoch of 2000, January 1, 12 h TDB as recommended by (Petit & Luzum, 2010) at given time T read as follows

$$
\begin{aligned}
F_1 = l \quad &= \quad \text{Mean anomaly of the Moon} \\
&= \quad 134.96340251° + 1717915923.2178''t + 31.8792''t^2 + \\
&\qquad\qquad +0.051635''t^3 - 0.00024470''t^4, \\
F_2 = l' \quad &= \quad \text{Mean anomaly of the Sun} \\
&= \quad 357.52910918° + 129596581.0481''t - 0.5532''t^2 + \\
&\qquad\qquad +0.000136''t^3 - 0.00001149''t^4, \\
F_3 = F \quad &= \quad s - N = \\
&= \quad 93.27209062° + 1739527262.8478''t - 12.7512''t^2 - \\
&\qquad\qquad -0.001037''t^3 + 0.00000417''t^4, \\
F_4 = D \quad &= \quad \text{Mean Elongation of the Moon from the Sun} \\
&= \quad 297.85019547° + 1602961601.2090''t - 6.3706''t^2 + \\
&\qquad\qquad +0.006593''t^3 - 0.00003169''t^4, \\
F_5 = \Omega = N \quad &= \quad \text{Mean Longitude of the Ascending Node of the Moon} \\
&= \quad 125.04455501° - 6962890.5431''t + 7.4722''t^2 + \\
&\qquad\qquad +0.007702''t^3 - 0.00005939''t^4,
\end{aligned} \tag{A.7}
$$

where the fundamental arguments F_j are called the set of Delaunay variables.

The Delaunay variable need to be substituted as harmonics function argument ω by integer numbers related as:

$$
\omega = \sum_{i=1}^{5} N_i F_i. \tag{A.8}
$$

Doodson number

In the tidal catalogs the Doodson number appear to be positive values as listed in the table A.1. These numbers are obtained by substitution

$$
\{d_j\}_1^6 \quad = \quad \begin{Bmatrix} 0 \\ 1 \\ 2 \end{Bmatrix} \{m_i\}_1^5 \quad -\{055555\}, \tag{A.9}
$$

Tide	Multipliers						Doodson number	Delaunay arguments					
	m_1	m_2	m_3	m_4	m_5								
Diurnal tides													
Q_1	1	-2	0	1	0	0	135.655	1	-1	0	-2	0	-2
O_1	1	-1	0	0	0	0	145.555	1	0	0	-2	0	-2
P_1	1	1	-2	0	0	0	163.555	1	0	0	-2	2	-2
K_1	1	1	0	0	0	0	165.555	1	0	0	0	0	0
Lunar semidiurnal tides													
N_2	2	-1	0	1	0	0	245.655	2	-1	0	-2	0	-2
M_2	2	0	0	0	0	0	255.555	2	0	0	-2	0	-2
S_2	2	2	-2	0	0	0	273.555	2	0	0	-2	2	-2
K_2	2	2	0	0	0	0	275.555	2	0	0	0	0	0

Table A.1: Doodson numbers.

where m_i are multipliers for Doodson numbers. Values $\begin{Bmatrix} 0 \\ 1 \\ 2 \end{Bmatrix}$ mark zonal, diurnal and semidiurnal waves correspondingly. Therefore, frequencies at solar day (def. $360°/\omega_\odot = 1$) of potential can be expressed

$$\omega_n = d_1\omega_\odot + d_2\dot{s} + d_3\dot{h} + d_4\dot{p} + d_5\dot{N}' + d_6\dot{p}_s, \tag{A.10}$$

for instance, M_2 or O_1:

$$\omega_{M_2} = 2\omega_\odot - 2\dot{s} + 2\dot{h}, \quad \omega_{0_1} = \omega_\odot - 2\dot{s} + \dot{h}. \tag{A.11}$$

Arguments can be calculated by means of Doodson or Delaunay arguments (GMST$+\pi$ included) consisted of 6 variables, $j = 6$, thus integer multipliers can be connected as

$$k_j = T^{-1}F_j \iff F_j = Tk_j: \quad T = \begin{pmatrix} 0 & 0 & 0 & -1 & 0 & 0 \\ 0 & 0 & 0 & 0 & 0 & -1 \\ -1 & 1 & 1 & 1 & 0 & 1 \\ 0 & 0 & -1 & 0 & 0 & -1 \\ -1 & 1 & 1 & 1 & -1 & 1 \\ 1 & 0 & 0 & 0 & 0 & 0 \end{pmatrix} \tag{A.12}$$

Note, that Doodson's variables can be related to Delaunay arguments as

$$
\begin{aligned}
\tau \quad & \text{Greenwich lunar time} = \text{Sidereal time} + 180° - s, \\
s \quad & \text{Mean longitude of the Moon} = F + N, \\
h \quad & \text{Mean longitude of the Sun} = s - D, \\
p \quad & \text{Mean longitude of the lunar perigee} = s - l, \\
N' \quad & = -N, \\
p_s \quad & \text{Mean longitude of the solar perigee} = s - D - l'.
\end{aligned} \tag{A.13}
$$

Angular Momentum Function

The position vector $\vec{x}$ and velocities $\vec{v}$ can be written in spherical coordinates for latitude φ and longitude λ for the sphere of the Earth radius r:

$$
\begin{aligned}
\vec{x} = \quad & r \begin{pmatrix} \cos\varphi\cos\lambda \\ \cos\varphi\sin\lambda \\ \sin\varphi \end{pmatrix}, \\
\vec{v} = \quad & u e_{\mathrm{E}} + v e_{\mathrm{N}} + w e_{\mathrm{R}},
\end{aligned} \tag{A.14}
$$

where velocities are given in local system for Radial (R), East (E) and North (N) components, so that the angular momentum functions separated in the pressure (p) and wind term (w) can be presented (Schindelegger *et al.*, 2013):

$$
\begin{aligned}
\hat{\chi} = \quad \boldsymbol{\chi_p} + \boldsymbol{\chi_w} = \quad & \frac{1.100\,\Omega\Delta\hat{I}}{C - A'} \int\int\int \rho r^4 \sin\varphi\cos^2\varphi\, e^{i\lambda}\,d\lambda\,d\varphi\,dr + \\
& + \frac{1.608}{(C - A')\Omega} \int\int\int \rho r^3 (u\sin\varphi + iv)\cos\varphi\, e^{i\varphi}\,d\lambda\,d\varphi\,dr \\
\chi_z = \quad \chi_p' + \chi_w' = \quad & \frac{0.748 I_{zz}\Omega}{\Omega C_m} \int\int\int \rho r^4 \cos^3\varphi\,d\lambda\,d\varphi\,dr + \\
& + \frac{0.997 h_z}{\Omega C_m} \int\int\int \rho r^3 u\cos^2\varphi\,d\lambda\,d\varphi\,dr
\end{aligned} \tag{A.15}
$$

where ρ is the density of the considered fluid.

Load tide

The surface deformations due to ocean loading can be expressend by means of infinite complex Green functions $\mathscr{G}(\theta)$ and load Love numbers h' and k' (Scherneck, 1991)

$$d_r = \mathscr{G}(\theta)^{(h')}dm = \int\int \zeta \frac{G\rho_w R_\oplus}{g} \sin\theta \, d\theta \, d\lambda \sum_{n=0}^{\infty} h'_n P_n(\cos\theta), \qquad\qquad (A.16)$$

$$d_h = \mathscr{G}(\theta)^{(k')}dm = \int\int \zeta \frac{G\rho_w R_\oplus}{g} \sin\theta \, d\theta \, d\lambda \sum_{n=0}^{\infty} k'_n \frac{\partial P_n(\cos\theta)}{\partial\theta},$$

where d_r and d_h are displacement in the radial and horizontal directions and the tidal elevations ζ are represented as harmonic functions in equation (2.28) and at practice introduced by the global tide maps for the largest signals in the TGP. Usually, Green functions which are introduced in equation (A.16) as an infinite sum over the spherical harmonics are provided by tables (Farrell, 1972) and θ specifies an angular distance from the given load to the chosen field point on the surface (Farrell, 1972; Scherneck, 1991), thus in equation (A.16) the integration over the glob should be done only. The typical displacement for M_2 and O_1 tides are illustrated in Figure A.2, which are also called load tide to underline the fact of crust deformation.

Load M$_2$ tide, cm
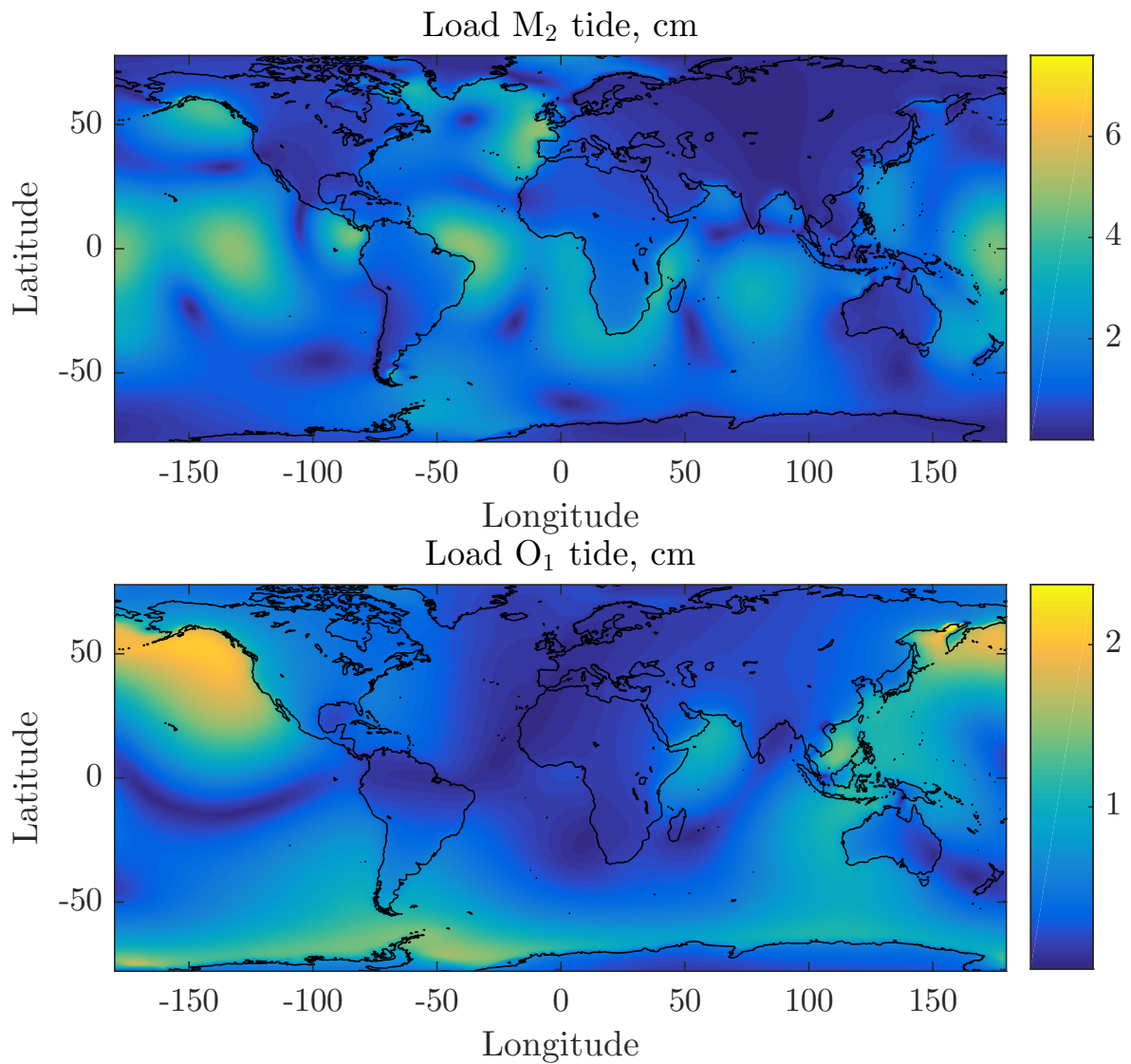
Load O$_1$ tide, cm

Figure A.2: Load M$_2$ tide (top) and load O$_1$ tide (bottom) calculated on the basis of a global tide map. The radial displacement in cm.

Appendix B

Auxiliary tables

Table B.1: Polar motion tidal terms estimated in this work in single session solution. Zero tides are included to assess the time series noise level. The last columns list average of the specific standard deviations that are representative of the formal errors of the individual coefficients $\{A^+, B^+, A^-, B^-\}$.

	Period (solar days)	γ	l	l'	F	D	Ω	A^+ µas	B^+ µas	A^- µas	B^- µas	$\bar{\sigma}_1$ µas	$\bar{\sigma}_2$ µas
	1.2114	1	-1	0	-2	-2	-2	-1.87	2.24	-1.50	-0.20	2.07	2.07
	1.1671	1	-2	0	-2	0	-1	-4.56	-5.07	1.43	0.48	2.13	2.13
$2Q_1$	1.1669	1	-2	0	-2	0	-2	-2.29	0.41	0.26	2.61	2.13	2.13
	1.1605	1	0	0	-2	-2	-1	-0.18	-0.38	1.11	-0.50	2.13	2.13
σ_1	1.1603	1	0	0	-2	-2	-2	-4.61	-0.19	-2.52	-2.65	2.12	2.12
	1.1197	1	-1	0	-2	0	-1	-6.15	1.82	1.41	-0.86	2.12	2.12
Q_1	1.1195	1	-1	0	-2	0	-2	-27.89	8.66	-3.48	-1.03	2.13	2.13
	1.1136	1	1	0	-2	-2	-1	-1.45	-1.70	1.40	-2.09	2.13	2.13
RO_1	1.1135	1	1	0	-2	-2	-2	-2.23	-0.44	-0.40	-0.21	2.13	2.13
	1.0761	1	0	0	-2	0	0	0.72	0.61	0.25	-0.90	2.17	2.17
	1.0760	1	0	0	-2	0	-1	-24.16	13.74	-2.28	-2.01	2.19	2.19
O_1	1.0758	1	0	0	-2	0	-2	-129.09	59.28	-1.85	1.94	2.16	2.16
	1.0751	1	-2	0	0	0	0	2.17	-1.77	-0.37	-2.98	2.11	2.11
$T0_1$	1.0695	1	0	0	0	-2	0	-0.41	-0.67	0.08	2.71	2.09	2.09
	1.0406	1	-1	0	-2	2	-2	-2.25	2.87	-0.85	0.32	2.10	2.10
	1.0355	1	1	0	-2	0	-1	2.49	2.09	0.13	-1.03	2.17	2.17
	1.0354	1	1	0	-2	0	-2	-1.00	1.03	0.64	-2.08	2.15	2.16
M_1	1.0347	1	-1	0	0	0	0	5.10	-2.00	0.12	0.97	2.15	2.15
	1.0346	1	-1	0	0	0	-1	0.63	-1.80	0.45	-0.50	2.17	2.17
χ_1	1.0295	1	1	0	0	-2	0	4.94	-1.11	-2.69	2.48	2.10	2.10
π_1	1.0055	1	0	-1	-2	2	-2	-2.63	5.33	-0.66	0.14	2.11	2.11

Table B.1: Polar motion tidal terms estimated in this work in single session solution. Zero tides are included to assess the time series noise level. The last columns list average of the specific standard deviations that are representative of the formal errors of the individual coefficients $\{A^+, B^+, A^-, B^-\}$.

| | Period (solar days) | Delaunay argument | | | | | | A^+ μas | B^+ μas | A^- μas | B^- μas | $\bar{\sigma}_1$ μas | $\bar{\sigma}_2$ μas |
		γ	l	l'	F	D	Ω						
	1.0029	1	0	0	-2	2	-1	-0.58	-2.82	3.36	0.03	2.15	2.15
P_1	1.0027	1	0	0	-2	2	-2	-49.08	25.62	-3.30	1.50	2.15	2.16
S_1	1.0000	1	0	-1	0	0	0	9.19	9.59	-0.12	0.41	2.13	2.13
	0.9974	1	0	0	0	0	1	1.35	-2.15	-0.73	-0.19	2.23	2.22
K_1	0.9973	1	0	0	0	0	0	156.93	-98.40	0.82	-3.39	2.25	2.24
	0.9971	1	0	0	0	0	-1	19.87	-12.23	-3.17	1.00	2.23	2.23
	0.9970	1	0	0	0	0	-2	1.48	0.12	1.48	3.22	2.20	2.20
ψ_1	0.9946	1	0	1	0	0	0	1.51	-0.40	2.07	0.89	2.12	2.11
φ_1	0.9919	1	0	0	2	-2	2	5.43	4.79	-0.06	-0.10	2.11	2.11
TT_1	0.9670	1	-1	0	0	2	0	0.53	-2.89	1.20	0.67	2.08	2.08
J_1	0.9624	1	1	0	0	0	0	8.88	-7.23	1.09	2.21	2.12	2.13
	0.9623	1	1	0	0	0	-1	2.09	2.05	1.14	-0.81	2.13	2.13
So_1	0.9342	1	0	0	0	2	0	1.75	-2.26	0.35	2.66	2.09	2.09
	0.9300	1	2	0	0	0	0	1.10	0.86	2.30	0.97	2.10	2.10
Oo_1	0.9294	1	0	0	2	0	2	4.49	-5.02	1.91	1.83	2.15	2.16
	0.9293	1	0	0	2	0	1	0.63	-4.36	2.33	-1.10	2.20	2.20
	0.9292	1	0	0	2	0	0	1.60	-0.43	-1.10	2.51	2.17	2.17
ν_1	0.8991	1	1	0	2	0	2	-3.76	-2.92	-2.49	3.05	2.14	2.14
	0.8990	1	1	0	2	0	1	-0.75	-1.06	-0.34	3.26	2.12	2.12
zero	1.1065	1	1	0	0	-4	-1	-0.87	0.84	0.52	0.25	2.10	2.09
zero	1.0176	1	1	1	0	-2	-1	2.15	2.34	-1.03	-0.37	2.10	2.10
zero	0.9142	1	1	-1	0	2	0	-2.20	0.22	-0.70	-0.94	2.08	2.08
	0.5484	2	-3	0	-2	0	-2	-0.23	2.04	1.93	2.64	2.06	2.07
	0.5470	2	-1	0	-2	-2	-2	-0.35	0.38	-1.59	4.14	2.06	2.07
$2N_2$	0.5377	2	-2	0	-2	0	-2	0.98	-0.55	-1.58	8.04	2.10	2.10
μ_2	0.5363	2	0	0	-2	-2	-2	1.24	-2.28	2.85	9.88	2.07	2.07
	0.5355	2	0	1	-2	-2	-2	1.23	-0.64	-2.19	3.26	2.09	2.09
	0.5282	2	-1	-1	-2	0	-2	-1.42	3.11	2.33	-0.36	2.09	2.09
	0.5275	2	-1	0	-2	0	-1	-1.78	1.60	-0.79	-0.28	2.13	2.13
N_2	0.5274	2	-1	0	-2	0	-2	9.49	-11.11	-2.47	40.25	2.13	2.13
	0.5267	2	-1	1	-2	0	-2	-1.40	-1.29	0.87	-2.98	2.09	2.09
ν_2	0.5261	2	1	0	-2	-2	-2	0.92	-1.59	2.00	7.40	2.08	2.08
	0.5253	2	1	1	-2	-2	-2	-0.58	0.62	0.76	0.72	2.09	2.09

Table B.1: Polar motion tidal terms estimated in this work in single session solution. Zero tides are included to assess the time series noise level. The last columns list average of the specific standard deviations that are representative of the formal errors of the individual coefficients $\{A^+, B^+, A^-, B^-\}$.

| | Period (solar days) | Delaunay argument | | | | | | A^+ µas | B^+ µas | A^- µas | B^- µas | $\bar{\sigma}_1$ µas | $\bar{\sigma}_2$ µas |
		γ	l	l'	F	D	Ω						
	0.5188	2	-2	0	-2	2	-2	-0.04	2.03	-0.89	-2.16	2.09	2.09
	0.5183	2	0	-1	-2	0	-2	-4.07	-0.81	0.12	0.45	2.09	2.10
	0.5176	2	0	0	-2	0	-1	-7.79	6.92	4.59	-8.01	2.13	2.13
M_2	0.5175	2	0	0	-2	0	-2	32.39	-73.17	-20.81	255.27	2.13	2.13
	0.5168	2	0	1	-2	0	-2	-1.14	-2.02	0.73	2.01	2.11	2.11
λ_2	0.5092	2	-1	0	-2	2	-2	1.60	-0.18	0.30	-0.11	2.09	2.09
L_2	0.5080	2	1	0	-2	0	-2	-0.92	1.32	-0.12	-9.07	2.08	2.09
	0.5078	2	-1	0	0	0	0	-2.04	-1.43	-2.54	-1.59	2.13	2.13
	0.5078	2	-1	0	0	0	-1	4.09	-3.41	0.70	1.26	2.15	2.15
T_2	0.5007	2	0	-1	-2	2	-2	2.90	-2.21	-1.92	7.24	2.11	2.10
S_2	0.5000	2	0	0	-2	2	-2	-6.33	-33.94	-78.54	110.63	2.09	2.09
R_2	0.4993	2	0	1	-2	2	-2	-1.61	1.13	-3.57	0.68	2.10	2.10
	0.4987	2	0	0	0	0	1	-1.10	0.59	7.84	1.41	2.18	2.19
K_2	0.4986	2	0	0	0	0	0	2.70	-12.63	-16.49	24.51	2.21	2.22
	0.4986	2	0	0	0	0	-1	6.02	1.89	-5.98	9.16	2.21	2.21
	0.4986	2	0	0	0	0	-2	0.30	1.79	-1.49	0.37	2.19	2.19
	0.4898	2	1	0	0	0	0	-1.37	1.58	-3.89	2.61	2.12	2.12
	0.4897	2	1	0	0	0	-1	1.01	1.79	2.83	0.26	2.12	2.12
	0.4811	2	0	0	2	0	2	2.07	0.81	-2.88	3.66	2.07	2.07
zero	0.5319	2	-4	0	-2	2	-2	0.73	-0.77	-1.49	-1.65	2.09	2.09
zero	0.5130	2	0	1	0	-2	0	1.55	1.03	3.08	-1.97	2.09	2.09
zero	0.4543	2	0	0	0	2	-2	-1.34	0.62	3.59	-0.81	2.08	2.08

Table B.2: dUT1 tidal terms estimated in this work in single session solution. Zero tides are included to assess the time series noise level. The columns list average of the specific standard deviations that are representative of the formal errors of the dUT1^c, dUT1^s individual coefficients.

	Period (solar days)	γ	l	l'	F	D	Ω	dUT1^c μas	dUT1^s μas	$\bar{\sigma}_1$ μas	$\bar{\sigma}_2$ μas
	1.2114	1	-1	0	-2	-2	-2	-0.22	0.16	0.11	0.11
	1.1671	1	-2	0	-2	0	-1	0.22	0.38	0.11	0.11
2Q$_1$	1.1669	1	-2	0	-2	0	-2	-0.10	1.45	0.11	0.11
	1.1605	1	0	0	-2	-2	-1	0.12	-0.04	0.11	0.11
	1.1603	1	0	0	-2	-2	-2	-0.35	1.13	0.11	0.11
	1.1197	1	-1	0	-2	0	-1	-0.65	0.94	0.11	0.11
Q$_1$	1.1195	1	-1	0	-2	0	-2	-2.70	5.19	0.11	0.11
	1.1136	1	1	0	-2	-2	-1	-0.43	0.20	0.11	0.11
RO$_1$	1.1135	1	1	0	-2	-2	-2	-0.48	0.93	0.11	0.11
	1.0761	1	0	0	-2	0	0	0.19	-0.22	0.11	0.11
	1.0760	1	0	0	-2	0	-1	-2.65	3.20	0.11	0.11
O$_1$	1.0758	1	0	0	-2	0	-2	-13.28	17.38	0.11	0.11
	1.0751	1	-2	0	0	0	0	-0.01	-0.34	0.11	0.11
T0$_1$	1.0695	1	0	0	0	-2	0	0.10	0.42	0.11	0.11
	1.0406	1	-1	0	-2	2	-2	0.18	-0.10	0.11	0.11
	1.0355	1	1	0	-2	0	-1	-0.07	-0.08	0.11	0.11
	1.0354	1	1	0	-2	0	-2	0.14	-0.42	0.11	0.11
M$_1$	1.0347	1	-1	0	0	0	0	0.63	-0.75	0.11	0.11
	1.0346	1	-1	0	0	0	-1	-0.03	-0.53	0.11	0.11
χ_1	1.0295	1	1	0	0	-2	0	0.18	0.04	0.11	0.11
π_1	1.0055	1	0	-1	-2	2	-2	-0.16	-0.01	0.11	0.11
	1.0029	1	0	0	-2	2	-1	-0.17	0.06	0.11	0.11
P$_1$	1.0027	1	0	0	-2	2	-2	-3.41	5.70	0.11	0.11
S$_1$	1.0000	1	0	-1	0	0	0	0.22	-0.94	0.11	0.11
	0.9974	1	0	0	0	0	1	-0.33	0.51	0.11	0.11
K$_1$	0.9973	1	0	0	0	0	0	9.51	-17.80	0.11	0.11
	0.9971	1	0	0	0	0	-1	0.82	-2.21	0.11	0.11
	0.9970	1	0	0	0	0	-2	0.15	0.17	0.11	0.11
ψ_1	0.9946	1	0	1	0	0	0	0.14	0.05	0.11	0.11
φ_1	0.9919	1	0	0	2	-2	2	-0.03	-0.30	0.11	0.11
TT$_1$	0.9670	1	-1	0	0	2	0	0.25	0.06	0.11	0.11
J$_1$	0.9624	1	1	0	0	0	0	0.84	-1.12	0.11	0.11
	0.9623	1	1	0	0	0	-1	0.01	-0.17	0.11	0.11

Table B.2: dUT1 tidal terms estimated in this work in single session solution. Zero tides are included to assess the time series noise level. The columns list average of the specific standard deviations that are representative of the formal errors of the dUT1^c, dUT1^s individual coefficients.

	Period (solar days)	γ	l	l'	F	D	Ω	dUT1^c µas	dUT1^s µas	$\bar{\sigma}_1$ µas	$\bar{\sigma}_2$ µas
So$_1$	0.9342	1	0	0	0	2	0	0.23	-0.19	0.11	0.11
	0.9300	1	2	0	0	0	0	-0.02	-0.30	0.11	0.11
Oo$_1$	0.9294	1	0	0	2	0	2	0.63	-0.66	0.11	0.11
	0.9293	1	0	0	2	0	1	0.41	-0.84	0.11	0.11
	0.9292	1	0	0	2	0	0	0.16	-0.15	0.11	0.11
ν_1	0.8991	1	1	0	2	0	2	-0.03	0.01	0.11	0.11
	0.8990	1	1	0	2	0	1	0.03	0.30	0.11	0.11
zero	1.1065	1	1	0	0	-4	-1	-0.13	-0.07	0.11	0.11
zero	1.0176	1	1	1	0	-2	-1	-0.08	-0.16	0.11	0.11
zero	0.9142	1	1	-1	0	2	0	-0.22	0.16	0.11	0.11
	0.5484	2	-3	0	-2	0	-2	0.15	0.14	0.11	0.11
	0.5470	2	-1	0	-2	-2	-2	-0.21	-0.00	0.11	0.11
2N$_2$	0.5377	2	-2	0	-2	0	-2	-0.51	-0.67	0.11	0.11
μ_2	0.5363	2	0	0	-2	-2	-2	-0.67	-0.64	0.11	0.11
	0.5355	2	0	1	-2	-2	-2	0.06	-0.05	0.11	0.11
	0.5282	2	-1	-1	-2	0	-2	-0.04	0.04	0.11	0.11
	0.5275	2	-1	0	-2	0	-1	-0.05	0.05	0.11	0.11
N$_2$	0.5274	2	-1	0	-2	0	-2	-1.52	-3.85	0.11	0.11
	0.5267	2	-1	1	-2	0	-2	-0.04	-0.02	0.11	0.11
ν_2	0.5261	2	1	0	-2	-2	-2	-0.21	-0.57	0.11	0.11
	0.5253	2	1	1	-2	-2	-2	-0.02	-0.02	0.11	0.11
	0.5188	2	-2	0	-2	2	-2	-0.03	-0.09	0.11	0.11
	0.5183	2	0	-1	-2	0	-2	-0.14	-0.13	0.11	0.11
	0.5176	2	0	0	-2	0	-1	0.13	0.58	0.11	0.11
M$_2$	0.5175	2	0	0	-2	0	-2	-8.26	-16.83	0.11	0.11
	0.5168	2	0	1	-2	0	-2	0.17	0.31	0.11	0.11
λ_2	0.5092	2	-1	0	-2	2	-2	0.19	0.23	0.11	0.11
L$_2$	0.5080	2	1	0	-2	0	-2	0.11	0.39	0.11	0.11
	0.5078	2	-1	0	0	0	0	0.00	-0.14	0.11	0.11
	0.5078	2	-1	0	0	0	-1	0.12	0.05	0.11	0.11
T$_2$	0.5007	2	0	-1	-2	2	-2	-0.13	-0.50	0.11	0.11
S$_2$	0.5000	2	0	0	-2	2	-2	-0.60	-8.02	0.11	0.11
R$_2$	0.4993	2	0	1	-2	2	-2	0.06	0.13	0.11	0.11

Table B.2: dUT1 tidal terms estimated in this work in single session solution. Zero tides are included to assess the time series noise level. The columns list average of the specific standard deviations that are representative of the formal errors of the dUT1^c, dUT1^s individual coefficients.

	Period (solar days)	Delaunay argument						dUT1^c μas	dUT1^s μas	$\bar{\sigma}_1$ μas	$\bar{\sigma}_2$ μas
		γ	l	l'	F	D	Ω				
K$_2$	0.4987	2	0	0	0	0	1	0.08	0.18	0.11	0.11
	0.4986	2	0	0	0	0	0	0.21	-2.51	0.11	0.11
	0.4986	2	0	0	0	0	-1	-0.08	-1.13	0.11	0.11
	0.4986	2	0	0	0	0	-2	0.18	0.14	0.11	0.11
	0.4898	2	1	0	0	0	0	0.06	-0.21	0.11	0.11
	0.4897	2	1	0	0	0	-1	-0.11	0.06	0.11	0.11
	0.4811	2	0	0	2	0	2	0.02	0.09	0.11	0.11
zero	0.5319	2	-4	0	-2	2	-2	-0.06	0.26	0.11	0.11
zero	0.5130	2	0	1	0	-2	0	0.24	-0.22	0.11	0.11
zero	0.4543	2	0	0	0	2	-2	0.02	-0.09	0.11	0.11

Table B.3: Polar motion tidal terms estimated by the global solution. Zero tides are included to assess the time series noise level. The last columns list average of the specific standard deviations that are representative of the formal errors of the individual coefficients $\{A^+, B^+, A^-, B^-\}$.

| | Period (solar days) | Delaunay argument | | | | | | A^+ µas | B^+ µas | A^- µas | B^- µas | $\bar{\sigma}_1$ µas | $\bar{\sigma}_2$ µas |
		γ	l	l'	F	D	Ω						
	1.2114	1	-1	0	-2	-2	-2	-4.32	0.51			0.92	0.92
	1.1671	1	-2	0	-2	0	-1	-7.51	-0.39			0.90	0.90
$2Q_1$	1.1669	1	-2	0	-2	0	-2	-4.42	1.85			0.85	0.85
	1.1605	1	0	0	-2	-2	-1	-0.42	-0.55			0.88	0.88
	1.1603	1	0	0	-2	-2	-2	-9.34	2.73			0.88	0.88
	1.1197	1	-1	0	-2	0	-1	-2.76	1.64			0.87	0.87
Q_1	1.1195	1	-1	0	-2	0	-2	-32.40	7.19			0.87	0.87
	1.1136	1	1	0	-2	-2	-1	0.07	-0.99			0.87	0.87
RO_1	1.1135	1	1	0	-2	-2	-2	-0.70	5.37			0.87	0.87
	1.0761	1	0	0	-2	0	0	-0.11	2.05			0.86	0.86
	1.0760	1	0	0	-2	0	-1	-25.77	11.91			0.87	0.87
O_1	1.0758	1	0	0	-2	0	-2	-127.30	57.91			0.89	0.89
	1.0751	1	-2	0	0	0	0	-1.80	-2.09			0.90	0.90
$T0_1$	1.0695	1	0	0	0	-2	0	-0.41	0.57			0.88	0.88
	1.0406	1	-1	0	-2	2	-2	-1.29	-0.19			0.85	0.85
	1.0355	1	1	0	-2	0	-1	-0.61	0.72			0.83	0.83
	1.0354	1	1	0	-2	0	-2	2.18	4.56			0.85	0.85
M_1	1.0347	1	-1	0	0	0	0	11.60	-4.35			0.88	0.88
	1.0346	1	-1	0	0	0	-1	4.45	0.61			0.86	0.86
χ_1	1.0295	1	1	0	0	-2	0	1.41	0.95			0.86	0.86
π_1	1.0055	1	0	-1	-2	2	-2	-3.06	5.24			0.87	0.87
	1.0029	1	0	0	-2	2	-1	2.34	0.28			0.84	0.84
P_1	1.0027	1	0	0	-2	2	-2	-47.78	33.07			0.84	0.84
S_1	1.0000	1	0	-1	0	0	0	2.73	5.86			0.84	0.84
	0.9974	1	0	0	0	0	1	-2.47	4.69			0.87	0.87
K_1	0.9973	1	0	0	0	0	0	155.17	-90.38			0.89	0.89
	0.9971	1	0	0	0	0	-1	20.31	-13.14			0.89	0.89
	0.9970	1	0	0	0	0	-2	3.97	-5.38			0.89	0.89
ψ_1	0.9946	1	0	1	0	0	0	-6.14	0.46			0.87	0.87
φ_1	0.9919	1	0	0	2	-2	2	3.97	-3.03			0.87	0.87
TT_1	0.9670	1	-1	0	0	2	0	0.75	1.09			0.83	0.83
J_1	0.9624	1	1	0	0	0	0	3.08	-2.58			0.83	0.83
	0.9623	1	1	0	0	0	-1	-1.41	-5.71			0.82	0.82

Table B.3: Polar motion tidal terms estimated by the global solution. Zero tides are included to assess the time series noise level. The last columns list average of the specific standard deviations that are representative of the formal errors of the individual coefficients $\{A^+, B^+, A^-, B^-\}$.

| | Period (solar days) | | Delaunay argument | | | | | A^+ µas | B^+ µas | A^- µas | B^- µas | $\bar{\sigma}_1$ µas | $\bar{\sigma}_2$ µas |
		γ	l	l'	F	D	Ω						
So_1	0.9342	1	0	0	0	2	0	4.21	-2.94			0.84	0.84
	0.9300	1	2	0	0	0	0	3.51	1.84			0.83	0.83
Oo_1	0.9294	1	0	0	2	0	2	3.32	-3.51			0.80	0.80
	0.9293	1	0	0	2	0	1	2.12	-3.30			0.82	0.82
	0.9292	1	0	0	2	0	0	-0.28	2.15			0.84	0.84
ν_1	0.8991	1	1	0	2	0	2	-1.58	-2.23			0.86	0.86
	0.8990	1	1	0	2	0	1	0.85	-1.60			0.84	0.84
zero	1.1065	1	1	0	0	-4	-1	-1.05	1.72			0.85	0.85
zero	1.0176	1	1	1	0	-2	-1	1.11	2.00			0.84	0.84
zero	0.9142	1	1	-1	0	2	0	-2.52	-0.10			0.82	0.82
	0.5484	2	-3	0	-2	0	-2	0.30	3.23			0.74	0.74
	0.5470	2	-1	0	-2	-2	-2	0.00	1.29			0.73	0.73
$2N_2$	0.5377	2	-2	0	-2	0	-2	0.01	0.29	-0.66	8.03	0.70	0.73
μ_2	0.5363	2	0	0	-2	-2	-2	2.90	-1.94	2.32	6.57	0.70	0.70
	0.5355	2	0	1	-2	-2	-2	1.88	1.85	0.64	4.40	0.70	0.74
	0.5282	2	-1	-1	-2	0	-2	0.42	-1.47	2.27	0.99	0.70	0.73
	0.5275	2	-1	0	-2	0	-1	-1.09	2.59	-3.15	2.24	0.70	0.74
N_2	0.5274	2	-1	0	-2	0	-2	10.24	-10.22	3.64	44.75	0.70	0.74
	0.5267	2	-1	1	-2	0	-2	-0.31	0.75	0.27	2.76	0.71	0.74
	0.5261	2	1	0	-2	-2	-2	1.20	0.04	0.76	7.68	0.72	0.73
	0.5253	2	1	1	-2	-2	-2	-3.32	-0.14	0.58	-1.04	0.70	0.75
	0.5188	2	-2	0	-2	2	-2	1.99	0.87	-1.54	-2.84	0.70	0.75
	0.5183	2	0	-1	-2	0	-2	-0.12	0.93	0.28	-2.69	0.70	0.74
	0.5176	2	0	0	-2	0	-1	-5.55	4.73	-1.84	-10.42	0.70	0.73
M_2	0.5175	2	0	0	-2	0	-2	33.65	-71.23	-5.59	264.69	0.70	0.73
	0.5168	2	0	1	-2	0	-2	-1.53	0.44	1.43	0.75	0.71	0.73
λ_2	0.5092	2	-1	0	-2	2	-2	1.58	0.45	-5.91	-7.52	0.71	0.73
L_2	0.5080	2	1	0	-2	0	-2	-1.89	1.97	3.35	-3.45	0.69	0.73
	0.5078	2	-1	0	0	0	0	-0.89	-0.79	-6.69	3.05	0.69	0.74
	0.5078	2	-1	0	0	0	-1	3.34	-0.74	-0.91	0.77	0.71	0.72
T_2	0.5007	2	0	-1	-2	2	-2	0.27	-2.83	-4.35	7.14	0.71	0.71
S_2	0.5000	2	0	0	-2	2	-2	-1.31	-29.34	-64.00	115.83	0.71	0.73
R_2	0.4993	2	0	1	-2	2	-2	0.28	0.32	-0.61	-3.58	0.70	0.73

Table B.3: Polar motion tidal terms estimated by the global solution. Zero tides are included to assess the time series noise level. The last columns list average of the specific standard deviations that are representative of the formal errors of the individual coefficients {A^+, B^+, A^-, B^-}.

	Period (solar days)	Delaunay argument						A^+ µas	B^+ µas	A^- µas	B^- µas	$\bar{\sigma}_1$ µas	$\bar{\sigma}_2$ µas
		γ	l	l'	F	D	Ω						
	0.4987	2	0	0	0	0	1	-0.62	2.37	-7.52	-2.94	0.72	0.73
K_2	0.4986	2	0	0	0	0	0	1.14	-13.62	-17.44	30.02	0.71	0.72
	0.4986	2	0	0	0	0	-1	5.89	-1.80	-7.95	7.83	0.74	0.75
	0.4986	2	0	0	0	0	-2	-0.28	4.76	2.48	-4.86	0.74	0.73
	0.4898	2	1	0	0	0	0	1.64	3.39	-2.68	2.06	0.73	0.77
	0.4897	2	1	0	0	0	-1	0.01	-0.91	-1.68	-1.17	0.72	0.76
	0.4811	2	0	0	2	0	2	0.16	-0.01	-1.04	-2.87	0.69	0.75
zero	0.5319	2	-4	0	-2	2	-2	1.07	-0.31	0.71	0.41	0.30	0.74
zero	0.5130	2	0	1	0	-2	0	-0.08	1.29	0.69	-0.24	1.92	0.71
zero	0.4543	2	0	0	0	2	-2	1.96	-0.60	0.69	-0.39	0.23	0.71

Table B.4: dUT1 tidal terms estimated by the global solution. Zero tides are included to assess the time series noise level. The last columns list average of the specific standard deviations that are representative of the formal errors of the individual coefficients dUT1^c and dUT1^s.

	Period (solar days)	γ	l	l'	F	D	Ω	dUT1^c µas	dUT1^s µas	$\bar{\sigma}_1$ µas	$\bar{\sigma}_2$ µas
	1.2114	1	-1	0	-2	-2	-2	-0.12	0.15	0.05	0.05
	1.1671	1	-2	0	-2	0	-1	0.18	0.60	0.05	0.05
2Q$_1$	1.1669	1	-2	0	-2	0	-2	-0.66	0.91	0.06	0.06
	1.1605	1	0	0	-2	-2	-1	0.42	0.02	0.06	0.06
	1.1603	1	0	0	-2	-2	-2	-0.15	0.79	0.06	0.06
	1.1197	1	-1	0	-2	0	-1	-0.44	0.97	0.06	0.06
Q$_1$	1.1195	1	-1	0	-2	0	-2	-3.21	4.69	0.06	0.06
	1.1136	1	1	0	-2	-2	-1	0.25	0.10	0.06	0.06
RO$_1$	1.1135	1	1	0	-2	-2	-2	-0.82	0.68	0.06	0.06
	1.0761	1	0	0	-2	0	0	0.07	-0.35	0.06	0.06
	1.0760	1	0	0	-2	0	-1	-2.79	3.46	0.06	0.06
O$_1$	1.0758	1	0	0	-2	0	-2	-12.76	16.97	0.06	0.06
	1.0751	1	-2	0	0	0	0	0.13	0.20	0.06	0.06
T0$_1$	1.0695	1	0	0	0	-2	0	-0.38	0.66	0.06	0.06
	1.0406	1	-1	0	-2	2	-2	0.16	-0.56	0.06	0.06
	1.0355	1	1	0	-2	0	-1	0.08	0.28	0.06	0.06
	1.0354	1	1	0	-2	0	-2	0.60	-0.47	0.06	0.06
M$_1$	1.0347	1	-1	0	0	0	0	0.91	-0.93	0.06	0.06
	1.0346	1	-1	0	0	0	-1	0.17	-0.36	0.06	0.06
χ_1	1.0295	1	1	0	0	-2	0	-0.29	-0.18	0.06	0.06
π_1	1.0055	1	0	-1	-2	2	-2	-0.23	0.33	0.06	0.06
	1.0029	1	0	0	-2	2	-1	-0.34	-0.39	0.06	0.06
P$_1$	1.0027	1	0	0	-2	2	-2	-3.47	5.71	0.06	0.06
S$_1$	1.0000	1	0	-1	0	0	0	-0.029	-0.611	0.06	0.06
	0.9974	1	0	0	0	0	1	-0.76	0.56	0.06	0.06
K$_1$	0.9973	1	0	0	0	0	0	9.24	-17.93	0.06	0.06
	0.9971	1	0	0	0	0	-1	0.84	-2.26	0.06	0.06
	0.9970	1	0	0	0	0	-2	0.41	0.26	0.06	0.06
ψ_1	0.9946	1	0	1	0	0	0	-0.18	-0.41	0.06	0.06
φ_1	0.9919	1	0	0	2	-2	2	-0.05	-0.33	0.06	0.06
TT$_1$	0.9670	1	-1	0	0	2	0	0.05	-0.31	0.06	0.06
J$_1$	0.9624	1	1	0	0	0	0	0.32	-1.05	0.06	0.06
	0.9623	1	1	0	0	0	-1	-0.23	0.08	0.06	0.06

Table B.4: dUT1 tidal terms estimated by the global solution. Zero tides are included to assess the time series noise level. The last columns list average of the specific standard deviations that are representative of the formal errors of the individual coefficients dUT1^c and dUT1^s.

	Period (solar days)	Delaunay argument						dUT1^c μas	dUT1^s μas	$\bar{\sigma}_1$ μas	$\bar{\sigma}_2$ μas
		γ	l	l'	F	D	Ω				
So$_1$	0.9342	1	0	0	0	2	0	0.44	0.11	0.06	0.06
	0.9300	1	2	0	0	0	0	-0.09	-0.57	0.06	0.06
Oo$_1$	0.9294	1	0	0	2	0	2	0.54	-1.20	0.06	0.06
	0.9293	1	0	0	2	0	1	0.31	-0.85	0.06	0.06
	0.9292	1	0	0	2	0	0	0.23	0.23	0.06	0.06
ν_1	0.8991	1	1	0	2	0	2	0.01	-0.29	0.06	0.06
	0.8990	1	1	0	2	0	1	0.07	0.16	0.06	0.06
zero	1.1065	1	1	0	0	-4	-1	0.025	-0.143	0.058	0.057
zero	1.0176	1	1	1	0	-2	-1	0.135	0.060	0.057	0.057
zero	0.9142	1	1	-1	0	2	0	-0.071	-0.031	0.056	0.056
	0.5484	2	-3	0	-2	0	-2	0.05	-0.16	0.05	0.05
	0.5470	2	-1	0	-2	-2	-2	-0.17	-0.01	0.05	0.05
2N$_2$	0.5377	2	-2	0	-2	0	-2	-0.39	-0.56	0.05	0.05
μ_2	0.5363	2	0	0	-2	-2	-2	-0.89	-0.75	0.05	0.05
	0.5355	2	0	1	-2	-2	-2	0.16	-0.06	0.05	0.05
	0.5282	2	-1	-1	-2	0	-2	-0.10	0.13	0.05	0.05
	0.5275	2	-1	0	-2	0	-1	-0.09	-0.11	0.05	0.05
N$_2$	0.5274	2	-1	0	-2	0	-2	-1.47	-3.77	0.05	0.05
	0.5267	2	-1	1	-2	0	-2	-0.07	-0.20	0.05	0.05
ν_2	0.5261	2	1	0	-2	-2	-2	-0.22	-0.69	0.05	0.05
	0.5253	2	1	1	-2	-2	-2	-0.11	-0.03	0.05	0.05
	0.5188	2	-2	0	-2	2	-2	-0.01	0.10	0.05	0.05
	0.5183	2	0	-1	-2	0	-2	-0.06	-0.24	0.05	0.05
	0.5176	2	0	0	-2	0	-1	0.19	0.47	0.05	0.05
M$_2$	0.5175	2	0	0	-2	0	-2	-7.76	-16.64	0.05	0.05
	0.5168	2	0	1	-2	0	-2	0.02	0.20	0.05	0.05
λ_2	0.5092	2	-1	0	-2	2	-2	-0.31	-0.16	0.05	0.05
L$_2$	0.5080	2	1	0	-2	0	-2	0.18	0.29	0.05	0.05
	0.5078	2	-1	0	0	0	0	0.08	-0.04	0.05	0.05
	0.5078	2	-1	0	0	0	-1	0.01	-0.05	0.05	0.05
T$_2$	0.5007	2	0	-1	-2	2	-2	0.09	-0.81	0.05	0.05
S$_2$	0.5000	2	0	0	-2	2	-2	-0.42	-7.96	0.05	0.05
R$_2$	0.4993	2	0	1	-2	2	-2	0.21	0.01	0.05	0.05

Table B.4: dUT1 tidal terms estimated by the global solution. Zero tides are included to assess the time series noise level. The last columns list average of the specific standard deviations that are representative of the formal errors of the individual coefficients dUT1[c] and dUT1[s].

| | Period (solar days) | Delaunay argument | | | | | | dUT1[c] μas | dUT1[s] μas | $\bar{\sigma}_1$ μas | $\bar{\sigma}_2$ μas |
		γ	l	l'	F	D	Ω				
	0.4987	2	0	0	0	0	1	0.07	-0.17	0.05	0.05
K_2	0.4986	2	0	0	0	0	0	0.11	-2.47	0.05	0.05
	0.4986	2	0	0	0	0	-1	0.15	-0.86	0.05	0.05
	0.4986	2	0	0	0	0	-2	0.04	-0.27	0.05	0.05
	0.4898	2	1	0	0	0	0	-0.09	-0.36	0.05	0.05
	0.4897	2	1	0	0	0	-1	-0.00	-0.06	0.05	0.05
	0.4811	2	0	0	2	0	2	-0.09	-0.04	0.05	0.05
zero	0.5319	2	-4	0	-2	2	-2	0.102	-0.081	0.049	0.049
zero	0.5130	2	0	1	0	-2	0	-0.112	0.029	0.048	0.047
zero	0.4543	2	0	0	0	2	-2	0.011	0.154	0.047	0.047

Acronyms

List of Figures

List of Tables

Bibliography

ALIZADEH, M.M., WIJAYA, D.D., HOBIGER, T., WEBER, R. AND SCHUH, H. (2013). Ionospheric Effects on Microwave Signals. In J. Böhm and H. Schuh, eds., *Atmospheric Effects in Space Geodesy*, 35–71, Springer Berlin Heidelberg, Berlin, Heidelberg.

ALTAMIMI, Z., REBISCHUNG, P., MÈTIVIER, L. AND COLLILIEUX, X. (2016). ITRF2014: A new release of the International Terrestrial Reference Frame modeling nonlinear station motions. *Journal of Geophysical Research: Solid Earth*, 121, 6109–6131, 2016JB013098.

ARBIC, B.K. (2005). Atmospheric forcing of the oceanic semidiurnal tide. *Geophysical Research Letters*, 32, L02610.

ARBIC, B.K., GARNER, S.T., HALLBERG, R.W. AND SIMMONS, H.L. (2004). The accuracy of surface elevations in forward global barotropic and baroclinic tide models. *Deep Sea Research Part II: Topical Studies in Oceanography*, 51, 3069 – 3101, small and mesoscale processes and their impact on the large scale.

ARTZ, T., TESMER NÉE BÖCKMANN, S. AND NOTHNAGEL, A. (2011). Assessment of periodic sub-diurnal Earth rotation variations at tidal frequencies through transformation of VLBI normal equation systems. *Journal of Geodesy*, 85, 565–584.

ARTZ, T., BERNHARD, L., NOTHNAGEL, A., STEIGENBERGER, P. AND TESMER, S. (2012). Methodology for the combination of sub-daily Earth rotation from GPS and VLBI observations. *Journal of Geodesy*, 86, 221–239.

BARNES, R.T.H., HIDE, R., WHITE, A.A. AND WILSON, C.A. (1983). Atmospheric angular momentum fluctuations, length-of-day changes and polar motion. *Proceedings of the Royal Society of London A: Mathematical, Physical and Engineering Sciences*, 387, 31–73.

BEHREND, D. (2013). "Coordinating Center Report". In K.D. Baver, D. Behrend and K. Armstrong, eds., *International VLBI Service for Geodesy and Astrometry*, 55–57.

BEUTLER, G., MERVART, L. AND VERDUN, A. (2006). *Methods of Celestial Mechanics: Volume II: Application to Planetary System, Geodynamics and Satellite Geodesy*. Astronomy and Astrophysics Library, Springer Berlin Heidelberg.

BIZOUARD, C., LAMBERT, S., BECKER, O. AND RICHARD, J.Y. (2017, preliminary draft on 9/Jan/2017). Combined solution C04 for Earth Rotation Parameters consistent with International Terrestrial Reference Frame 2014. In *IERS Earth Orientation Centre*.

BÖHM, J., WERL, B. AND SCHUH, H. (2006). Troposphere mapping functions for GPS and very long baseline interferometry from European Centre for Medium-Range Weather Forecasts operational analysis data. *Journal of Geophysical Research: Solid Earth*, 111, b02406.

BÖHM, J., BÖHM, S., NILSSON, T., PANY, A., PLANK, L., SPICAKOVA, H., TEKE, K. AND SCHUH, H. (2012). The New Vienna VLBI Software VieVS. In Kenyon, S. and Pacino, M. C. and Marti, U., ed., *Geodesy for Planet Earth: Proceedings of the 2009 IAG Symposium, Buenos Aires, Argentina, 31 August 31 - 4 September 2009*, 1007–1011, Springer Berlin Heidelberg, Berlin, Heidelberg.

BÖHM, S. (2012). *Tidal excitation of Earth rotation observed by VLBI and GNSS*. Schriftenreihe der Studienrichtung VERMESSUNG UND GEOINFORMATION, Geowissenschaftliche Mitteilungen, Heft Nr. 90.

BÖHM, S., BRZEZIŃSKI, A. AND SCHUH, H. (2012). Complex demodulation in VLBI estimation of high frequency Earth rotation components. *Journal of Geodynamics*, 62, 56–68.

BOS, M.S. AND SCHERNECK, H.G. (2007). "Free ocean tide loading provider". *Data set accessed YYYY-MM-DD at* http://www.oso.chalmers.se/loading.

CAPITAINE, N., WALLACE, P.T. AND CHAPRONT, J. (2003). Expressions for IAU 2000 precession quantities. *Astronomy and Astrophysics*, 412, 567–586.

CARRÉRE, L. AND LYARD, F. (2003). Modeling the barotropic response of the global ocean to atmospheric wind and pressure forcing - comparisons with observations. *Geophysical Research Letters*, 30, n/a–n/a, 1275.

CHAO, B.F., RAY, R.D., GIPSON, J.M., EGBERT, G.D. AND MA, C. (1996). Diurnal/semidiurnal polar motion excited by oceanic tidal angular momentum. *Journal of Geophysical Research: Solid Earth*, 101, 20151–20163.

CHAPMAN, S. AND LINDZEN, R.S. (1970). *Atmospheric Tides: Thermal and Gravitational*. Springer Netherlands, Dordrecht.

CHARLOT, P. (1990). Radio-source structure in astrometric and geodetic very long baseline interferometry. *Astronomical Journal*, 99, 1309–1326.

CHEN, G. AND HERRING, T.A. (1997). Effects of atmospheric azimuthal asymmetry on the analysis of space geodetic data. *Journal of Geophysical Research: Solid Earth*, 102, 20489–20502.

DAI, A. AND WANG, J. (1999). Diurnal and Semidiurnal Tides in Global Surface Pressure Fields. *Journal of the Atmospheric Sciences*, 56, 3874–3891.

DARWIN, G.H. (1898). *The tides and kindred phenomena in the solar system; the substance of lectures delivered in 1897 at the Lowell Institute, Boston, Massachusetts*. Boston, New York, Houghton, Mifflin and company.

DAVIS, J.L., HERRING, T.A., SHAPIRO, I.I., ROGERS, A.E.E. AND ELGERED, G. (1985). Geodesy by radio interferometry: Effects of atmospheric modeling errors on estimates of baseline length. *Radio Science*, 20, 1593–1607.

DEHANT, V. AND MATHEWS, P.M. (2015). *Precession, Nutation and Wobble of the Earth*. Cambridge University Press.

DERMANIS, A. AND MUELLER, I.I. (1978). Earth rotation and network geometry optimization for very long baseline interferometers. *Bulletin géodésique*, 52, 131–158.

DESAI, S.D. (2002). Observing the pole tide with satellite altimetry. *Journal of Geophysical Research: Oceans*, 107, 7–1–7–13, 3186.

DESAI, S.D. AND SIBOIS, A.E. (2016). Evaluating predicted diurnal and semidiurnal tidal variations in polar motion with GPS-based observations. *Journal of Geophysical Research: Solid Earth*, 121, 5237–5256, 2016JB013125.

DOBSLAW, H. AND THOMAS, M. (2005). Atmospheric induced oceanic tides from ECMWF forecasts. *Geophysical Research Letters*, 32, L10615.

DOBSLAW, H., BERGMANN-WOLF, I., DILL, R., POROPAT, L. AND FLECHTNER, F. (2017). GRACE AOD1B Product Release 06: Long-Term Consistency and the Treatment of Atmospheric Tides. In *EGU General Assembly Conference Abstracts*, Vol. 19 of *EGU General Assembly Conference Abstracts*, 10136.

EGBERT, G.D. AND EROFEEVA, S.Y. (2002). Efficient Inverse Modeling of Barotropic Ocean Tides. *Journal of Atmospheric and Oceanic Technology*, 19, 183–204.

EGBERT, G.D., BENNETT, A.F. AND FOREMAN, M.G.G. (1994). TOPEX/POSEIDON tides estimated using a global inverse model. *Journal of Geophysical Research: Oceans*, 99, 24821–24852.

EUBANKS, M., MA, C. AND VANDENBERG, N.R. (1999). Analysis Coordinator Report. In N.R. Vandenberg, ed., *International VLBI Service for Geodesy and Astrometry*.

EUBANKS, T.M. (2013). *Variations in the Orientation of the Earth*, 1–54. American Geophysical Union.

FARRELL, W.E. (1972). Deformation of the Earth by surface loads. *Reviews of Geophysics*, 10, 761–797.

FEY, A.L., GORDON, D., JACOBS, C.S., MA, C., GAUME, R.A., ARIAS, E.F., BIANCO, G., BOBOLTZ, D.A., BÖCKMANN, S., BOLOTIN, S., CHARLOT, P., COLLIOUD, A., ENGELHARDT, G., GIPSON, J.,

GONTIER, A.M., HEINKELMANN, R., KURDUBOV, S., LAMBERT, S., LYTVYN, S., MACMILLAN, D.S., MALKIN, Z., NOTHNAGEL, A., OJHA, R., SKURIKHINA, E., SOKOLOVA, J., SOUCHAY, J., SOVERS, O.J., TESMER, V., TITOV, O., WANG, G. AND ZHAROV, V. (2015). The Second Realization of the International Celestial Reference Frame by Very Long Baseline Interferometry. *The Astronomical Journal*, 150, 58–74.

FEYNMAN, R.P., LEIGHTON, R.B. AND SANDS, M. (1963). *Feynman lectures on physics - Volume 1*. Addison-Wesley.

GAMBIS, D. AND LUZUM, B. (2011). Earth rotation monitoring, UT1 determination and prediction. *Metrologia*, 48, S165.

GAMBIS, D., BAUDOUIN, P., BIZOUARD, C., BOUGEARD, M., CARLUCCI, T., ESSAIFI, N., FRANCOU, G. AND JEAN-ALEXIS, D. (2001). Annual Report 2001: 3.5.1 Earth Orientation Centre . In *IERS Earth Orientation Centre*.

GAMBIS, D., BIZOUARD, C., BECKER, O., CARLUCCI, T., RICHARD, J.Y., BAUDOUIN, P. AND LAMBERT, S. (2015). Annual Report 2015: 3.5.1 Earth Orientation Centre. In *IERS Earth Orientation Centre*.

GIPSON, J.M. (1996). Very long baseline interferometry determination of neglected tidal terms in high-frequency Earth orientation variation. *Journal of Geophysical Research: Solid Earth*, 101, 28051–28064.

GIRDIUK, A., SCHINDELEGGER, M. AND BÖHM, J. (2016a). Tidal atmospheric and ocean loading in VLBI analysis. In *EGU General Assembly Conference Abstracts*, Vol. 18, 4498.

GIRDIUK, A., SCHINDELEGGER, M., MADZAK, M. AND BÖHM, J. (2016b). Detection of the Atmospheric S_1 Tide in VLBI Polar Motion Time Series. In *International Association of Geodesy Symposia*, 1–7, Springer Berlin Heidelberg, Berlin, Heidelberg.

GORDON, D. (2017). Impact of the VLBA on reference frames and earth orientation studies. *Journal of Geodesy*, 91, 735–742.

GROSS, R.S. (1992). Correspondence between theory and observations of polar motion. *Geophysical Journal International*, 109, 162–170.

GROSS, R.S. (2015). Earth Rotation Variations — Long Period. In G. Schubert, ed., *Treatise on Geophysics (Second Edition)*, 215–261, Elsevier, Oxford.

HAAS, R., NOTHNAGEL, A., SCHUH, H. AND TITOV, O. (1999). Explanatory Supplement to the Section "Antenna Deformation. *DGFI Report No. 71, ed. by H. Schuh, 26-29*.

HAGAN, M.E. AND FORBES, J.M. (2002). Migrating and nonmigrating diurnal tides in the middle and upper atmosphere excited by tropospheric latent heat release. *Journal of Geophysical Research: Atmospheres*, 107, ACL 6–1–ACL 6–15, 4754.

HAGAN, M.E., FORBES, J.M. AND RICHMOND, A. (2003). Atmospheric tides. In J. Holton, J. Pyle and J. Curry, eds., *Encyclopedia of Atmospheric Sciences*, 159–165, Academic Press.

HOBSON, E. (1931). *The Theory of Spherical and Ellipsoidal Harmonics*. Cambridge University Press.

HOFMEISTER, A. (2016). *Determination of path delays in the atmosphere for geodetic VLBI by means of ray-tracing*. Ph.D. thesis, Department f. Geodäsie u. Geoinformation / Höhere Geodäsie.

KOLACZEK, B., NASTULA, J. AND SALSTEIN, D. (2003). El Nino-related variations in atmosphere–polar motion interactions. *Journal of Geodynamics*, 36, 397 – 406, Earth Rotation and Episodic Processes.

KRÁSNÁ, H., NICKOLA, M. AND BÖHM, J. (2014). Axis offset estimation of VLBI Telescopes. In K.D. Baver, D. Behrend and K. Armstrong, eds., *IVS 2014 General Meeting Proceedings*, 339–343.

KRÁSNÁ(NÉE SPICAKOVA), H., BÖHM, J., PLANK, L., NILSSON, T. AND SCHUH, H. (2014). Atmospheric Effects on VLBI-Derived Terrestrial and Celestial Reference Frames. In C. Rizos and P. Willis, eds., *Earth on the Edge: Science for a Sustainable Planet: Proceedings of the IAG General Assembly, Melbourne, Australia, June 28 - July 2, 2011*, 203–208, Springer Berlin Heidelberg, Berlin, Heidelberg.

LARA, M., SAN-JUAN, J.F., FOLCIK, Z.J. AND CEFOLA, P. (2011). Deep Resonant GPS-Dynamics Due to the Geopotential. *The Journal of the Astronautical Sciences*, 58, 661–676.

LUZUM, B. AND GAMBIS, D. (2014). EXPLANATORY SUPPLEMENT TO IERS BULLETIN A and BULLETIN B/C04. In *IERS Earth Orientation Centre*.

LYARD, F., LEFÉVRE, F., LETELLIER, T. AND FRANCIS, O. (2004). FES99 (FES2004) was produced by Legos and CLS Space Oceanography Division and distributed by Aviso, with support from Cnes (http://www.aviso.altimetry.fr/)), as part of the Ssalto ground processing segment. *Aviso*.

LYARD, F., LEFÉVRE, F., LETELLIER, T. AND FRANCIS, O. (2006). Modelling the global ocean tides: a modern insight from FES2004. *Ocean Dynamics*, 56, 394–415.

LYARD, F., LEFÉVRE, F., LETELLIER, T. AND FRANCIS, O. (2012). FES2012 was produced by Noveltis, Legos and CLS Space Oceanography Division and distributed by Aviso, with support from Cnes (http://www.aviso.altimetry.fr/). *Aviso*.

LYARD, F., LEFÉVRE, F., LETELLIER, T. AND FRANCIS, O. (2014). FES2014 is distributed by Aviso (http://www.aviso.altimetry.fr/). Copyright: 2014- ongoing Legos/Noveltis/Cnes/CLS . *Aviso*.

MACMILLAN, D.S., HIMWICH, W.E., THOMAS, C.C., VANDENBERG, N.R., BOSWORTH, J.M., CHAO, B., CLARK, T.A. AND MA, C. (1999). CORE: Continuous, High-Accuracy Earth Orientation Measurements. In W. Schlüter and H. Hase, eds., *European VLBI for Geodesy and Astrometry*, 166–171.

MADZAK, M., SCHINDELEGGER, M., BÖHM, J., BOSCH, W. AND HAGEDOORN, J. (2016). High-frequency Earth rotation variations deduced from altimetry-based ocean tides. *Journal of Geodesy*, 90, 1237–1253.

MALKIN, Z. (2009). On comparison of the Earth orientation parameters obtained from different VLBI networks and observing programs. *Journal of Geodesy*, 83, 547–556.

MATHEWS, P.M., BUFFETT, B.A. AND SHAPIRO, I.I. (1995). Love numbers for a rotating spheroidal EarthâĹů New definitions and numerical values. *Geophysical Research Letters*, 22, 579–582.

MATHEWS, P.M., HERRING, T.A. AND BUFFETT, B.A. (2002). Modeling of nutation and precession: New nutation series for nonrigid Earth and insights into the Earth's interior. *Journal of Geophysical Research: Solid Earth*, 107, ETG 3–1–ETG 3–26.

MCCARTHY, D. AND CAPITAINE, N. (2002). Practical Consequences of Resolution B1.6 "IAU2000 Precession-Nutation Model," Resolution B1.7 "Definition of Celestial Intermediate Pole," and Resolution B1.8 "Definition and Use of Celestial and Terrestrial Ephemeris Origin". In *Proceedings of the IERS Workshop on the Implementation of the New IAU Resolutions*, IERS Technical Note; 29, Frankfurt am Main: Verlag des Bundesamts für Kartographie und Geodäsie.

MENDES CERVEIRA, P.J., BOEHM, J., SCHUH, H., KLUEGEL, T., VELIKOSELTSEV, A., SCHREIBER, K.U. AND BRZEZINSKI, A. (2009). Earth Rotation Observed by Very Long Baseline Interferometry and Ring Laser. *Pure and Applied Geophysics*, 166, 1499–1517.

MENEMENLIS, D., CAMPIN, J., HEIMBACH, P., HILL, C., LEE, T., NGUYEN, A., SCHODLOK, M. AND ZHANG, H. (2008). ECCO2: High-Resolution Global-Ocean and Sea-Ice Data Synthesis. *AGU Fall Meeting Abstracts*.

MINTTU, U., KAREN, B., GIPSON, G., NILSSON, T. AND KRÀSNÀ, H. (2016). Comparison of VieVS and Solve UT1 results from VLBI measurements. *Journal of Geodesy and Geoinformation*, 3, 1–8.

MORITZ, H. AND MÜLLER, I. (1987). *Earth Rotation*. The Ungar Publishing Company.

MUNK, W.H. AND CARTWRIGHT, D.E. (1966). Tidal Spectroscopy and Prediction. *Philosophical Transactions of the Royal Society of London A: Mathematical, Physical and Engineering Sciences*, 259, 533–581.

NILSSON, T., BÖHM, J., WIJAYA, D.D., TRESCH, A., NAFISI, V. AND SCHUH, H. (2013). Path Delays in the Neutral Atmosphere. In J. Böhm and H. Schuh, eds., *Atmospheric Effects in Space Geodesy*, 73–136, Springer Berlin Heidelberg, Berlin, Heidelberg.

NOTHNAGEL, A. (2009). Conventions on thermal expansion modelling of radio telescopes for geodetic and astrometric VLBI. *Journal of Geodesy*, 83, 787–792.

PETIT, G. AND LUZUM, B. (2010). IERS Conventions (2010). *IERS Technical Note*, 36.

138

PETROV, L. (2015). "The International Mass Loading Service". *MEMO:* http://arxiv.org/abs/1503.00191.

PETROV, L. AND BOY, J.P. (2004). Study of the atmospheric pressure loading signal in very long baseline interferometry observations. *Journal of Geophysical Research: Solid Earth*, 109, n/a–n/a, B03405.

PETROV, L. AND MA, C. (2003). Study of harmonic site position variations determined by very long baseline interferometry. *Journal of Geophysical Research: Solid Earth*, 108, 2190.

PLAG, H.P., BEUTLER, G., GROSS, R., HERRING, T.A., RIZOS, C., RUMMEL, R., SAHAGIAN, D. AND ZUMBERGE, J. (2009). Introduction. In H.P. Plag and M. Pearlman, eds., *Global Geodetic Observing System: Meeting the Requirements of a Global Society on a Changing Planet in 2020*, 1–13, Springer Berlin Heidelberg, Berlin, Heidelberg.

PONTE, R.M. AND RAY, R.D. (2002). Atmospheric pressure corrections in geodesy and oceanography: A strategy for handling air tides. *Geophysical Research Letters*, 29, 6–1–6–4, 2153.

PONTE, R.M., RAJAMONY, J. AND GREGORY, J.M. (2002). Ocean angular momentum signals in a climate model and implications for Earth rotation. *Climate Dynamics*, 19, 181–190.

PUGH, D. (1987). *Tides, Surges and Mean Sea Level*. John Wiley & Sons Ltd.

RAY, R.D. AND EGBERT, G.D. (2004). The global S1 tide. *Journal of Physical Oceanography*, 34, 1922–1935.

RAY, R.D. AND PONTE, R.M. (2003). Barometric tides from ECMWF operational analyses. *Annales Geophysicae*, 21, 1897–1910.

RAY, R.D., CHAO, B.F., KOWALIK, Z. AND PROSHUTINSKY, A.Y. (1997). Angular momentum of Arctic Ocean tides. *Journal of Geodesy*, 71, 344–350.

RODER, H. (1931). Amplitude, Phase, and Frequency Modulation. *Proceedings of the Institute of Radio Engineers*, 19, 2145–2176.

SASAO, T. AND WAHR, J.M. (1981). An excitation mechanism for the free 'core nutation'. *Geophysical Journal of the Royal Astronomical Society*, 64, 729–746.

SAVCENKO, R. AND BOSCH, W. (2012). EOT11A - Empirical Ocean Tide Model from Multi-Mission Satellite Altimetry. *Deutsches Geodätisches Forschungsinstitut (DGFI), München*.

SCHERNECK, H.G. (1991). A parametrized solid earth tide model and ocean tide loading effects for global geodetic baseline measurements. *Geophysical Journal International*, 106, 677–694.

SCHINDELEGGER, M. (2014). *Atmosphere-induced short period variations of Earth rotation*. Schriftenreihe der Studienrichtung VERMESSUNG UND GEOINFORMATION, Geowissenschaftliche Mitteilungen, Heft Nr. 96.

SCHINDELEGGER, M., BÖHM, S., BÖHM, J. AND SCHUH, H. (2013). Atmospheric Effects on Earth Rotation. In J. Böhm and H. Schuh, eds., *Atmospheric Effects in Space Geodesy*, 181–231, Springer Berlin Heidelberg, Berlin, Heidelberg.

SCHINDELEGGER, M., SALSTEIN, D., EINŠPIGEL, D. AND MAYERHOFER, C. (2017). Diurnal atmosphere-ocean signals in Earth's rotation rate and a possible modulation through ENSO. *Geophysical Research Letters*, 44, 2755–2762.

SCHINDELEGGER, M., EINŠPIGEL, D., SALSTEIN, D. AND BÖHM, J. (2016). The global S_1 tide in Earth's nutation. *Surveys in Geophysics*, 37, 643–680.

SCHMIDT, M. (1963). 3C 273 : A Star-Like Object with Large Red-Shift. *Nature*, 197, 1040.

SCHREIBER, K.U., VELIKOSELTSEV, A., ROTHACHER, M., KLÜGEL, T., STEDMAN, G.E. AND WILTSHIRE, D.L. (2004). Direct measurement of diurnal polar motion by ring laser gyroscopes. *Journal of Geophysical Research: Solid Earth*, 109.

SCHUH, H. AND BÖHM, J. (2013). Very Long Baseline Interferometry for Geodesy and Astrometry. In G. Xu, ed., *Sciences of Geodesy - II: Innovations and Future Developments*, 339–376, Springer Berlin Heidelberg, Berlin, Heidelberg.

SIDORENKOV, N.S. (2009). *The Interaction Between Earth's Rotation and Geophysical Processes*. Wiley.

SIMON, B., LEMAITRE, A. AND SOUCHAY, J. (2013). Oceanic Tides. In J. Souchay, S. Mathis and T. Tokieda, eds., *Tides in Astronomy and Astrophysics*, 83–114, Springer Berlin Heidelberg, Berlin, Heidelberg.

SIR WILLIAM THOMSON (LORD KELVIN) (1882). *The Tides. Evening Lecture To The British Association At The Southampton Meeting on Friday*. Boston, New York, Houghton, Mifflin and company.

SKURIKHINA, E. (2001). On Computation of Antenna Thermal Deformation in VLBI Data Processing. In D. Behrend and A. Rius, eds., *15th Workshop Meeting on European VLBI for Geodesy and Astrometry*, 124.

SOVERS, O.J., FANSELOW, J.L. AND JACOBS, C.S. (1998). Astrometry and geodesy with radio interferometry: experiments, models, results. *Reviews of Modern Physics*, 70, 1393–1454.

TERCJAK, M. AND BRZEZIŃSKI, A. (2017). On the Influence of Known Diurnal and Subdiurnal Signals in Polar Motion and UT1 on Ring Laser Gyroscope Observations. *Pure and Applied Geophysics*, 1–13.

TORGE, W. AND MÜLLER, J. (2012). *Geodesy*. De Gruyter.

VAN DAM, T. (2010). Updated October 2010. NCEP Derived 6-hourly, global surface displacements at 2.5° x 2.5° spacing. *Data set accessed YYYY-MM-DD at* http://geophy.uni.lu/ncep-loading.html.

VANDENBERG, N.R. (1999a). IVS 1999 Annual Report. In N.R. Vandenberg, ed., *International VLBI Service for Geodesy and Astrometry*.

VANDENBERG, N.R. (1999b). IVS is established. In W. Schlüter and H. Hase, eds., *European VLBI for Geodesy and Astrometry*, 6–10.

WEBER, R., UMNIG, E., GRUBER, J., MARAS, J., HINTERBERGER, F., JOLDZIK, N., NASTULA, J. AND BRZEZIŃSKI, A. (2017). GNSS-EOP: High-frequency determination of the Earth Orientation Parameters by GNSS. Final report. In *European Space Agency Contract Report*.

WIJAYA, D.D., BÖHM, J., KARBON, M., KRÀSNÀ, H. AND SCHUH, H. (2013). Atmospheric Pressure Loading. In J. Böhm and H. Schuh, eds., *Atmospheric Effects in Space Geodesy*, 137–157, Springer Berlin Heidelberg, Berlin, Heidelberg.

YODER, C.F., WILLIAMS, J.G. AND PARKE, M.E. (1981). Tidal variations of Earth rotation. *Journal of Geophysical Research: Solid Earth*, 86, 881–891.

Anastasiia Girdiuk

27 December 1990, Belgorod, Russia
fluent English | zero basic German |
Russian mother tongue

Gusshausstraße 25-29/E120 (CB0521),
1040 Vienna, Austria
+43 (1) 58801 - 12866
anastasiia.girdiuk@geo.tuwien.ac.at
geo.tuwien.ac.at/staff/anastasiia-girdiuk/

EDUCATION

Apr 2015 – Nov 2017, PhD defence: 15 November 2017
PhD student,
Vienna University of Technology (TU Wien), Austria

Thesis:	Atmospheric tides in Earth Rotation observed with Very Long Baseline Interferometry (VLBI)
Main advisor:	Prof. Johannes Böhm, TU Wien Head of the Advanced Geodesy
Reviewer:	Dr. Michael Schindelegger, TU Wien, Project Assistant
Reviewer:	Dr. David Salstein, Atmospheric and Environmental Research (USA), Scientist

Sep 2008 - Jul 2013
Astronomer (specialization),
Saint Petersburg State University (SPbU), Russia

Thesis:	VLBI observations of close Jupiter approaches with reference quasars in 2014-2016
Advisor:	Dr. Oleg Titov, Geoscience Australia, Research scientist
Reviewer	Dr. Sergei Kurdubov, IAA, Research scientist

Highlighted intermediate thesis, 2010:

	Gravitational waves: the current statement of the detection issue
Main advisor:	Dr. Yurij Baryshev, SPbU Senior Researcher at the Laboratory of Theoretical Astrophysics

PUBLICATIONS

Astronomy & Astrophysics,
02/2015, Volume 574, id.A128, 7 pp.
"Applying the theory of general relativity to reducing geodetic VLBI data"
Oleg Titov, Anastasiia Girdiuk

International Association of Geodesy Symposia,
2016, DOI 10.1007/1345_2016_234
"Detection of the Atmospheric S_1 Tide in VLBI Polar Motion Time Series"
Anastasiia Girdiuk, Michael Schindelegger, Matthias Madzak, Johannes Böhm
. . .

Publications in proceedings of IVS General Meetings, EGU, "Journèes" as first co-author

WORK EXPERIENCE

CURRENT, FROM DEC 2014
Project Assistant,
Vienna University of Technology (TU Wien)
Atmosphere-Induced Short Period Variations of Earth Rotation (ASPIRE) I1479 project, International Program FWF/DFG. In view of the geophysical approach success in atmospheric tides assessment, my task is to improve the geodetic estimates in Earth's Rotation by means of VLBI observations.

OCT 2013 – OCT 2014
Researcher, *Institute of Applied Astronomy (IAA)*
Institute tenure. My task was to obtain the Pluto's solution in the solar system EPM2015 ephemerides.

COMMUNICATION ACTIVITY

CONFERENCES | Oral Presentations, last year:

April 2017 Vienna, Austria	"Atmospheric tides in variations of VLBI station positions" European Geosciences Union (EGU) General Assembly 2017
May 2017 Gothenburg, Sweden	"An empirical atmospheric tidal loading solution for particular VLBI stations" 23rd Working Meeting of the European VLBI Group for Geodesy and Astrometry
September 2017 Alicante, Spain	"Assessing recent high-frequency Earth rotation models with VLBI" Journées 2017, University of Alicante

IN 2015-2017 :

Poster and oral presentations at IVS General Meetings, EGU, "Journèes" as first co-author

Lectures on topic of the Vienna VLBI and Satellite Software (VieVS) at Workshop at TU Wien

ASPIRE-project business meetings in Potsdam | Vienna

AWARDS

International Association of Geodesy
Travel Awards for participation in conferences:
International VLBI Service for Geodesy and Astrometry (IVS) General Meeting 2014 and 2016

COMPUTER SKILLS

Specific software	VieVS, OCCAM
Other	MATLAB, FORTRAN || LATEX, PGFPlot bash, PYTHON || Linux